Department of Physics and Astronomy

Heidelberg University

Master thesis in Physics

submitted by

Daniel Lange

born in Rottweil

2022

Development of the novel transportable online mass-spectrometer PILOT-Trap with dynamic buffer-gas cooling for stored ions

This Master thesis has been carried out by

Daniel Lange

at the

Max Planck Institut for Nuclear Physics

under the supervision of

Prof. Dr. Klaus Blaum

Development of the novel transportable online mass-spectrometer PILOT-Trap with dynamic buffer-gas cooling for stored ions

The novel transportable PILOT-Trap experiment set up in the framework of this thesis aims to measure masses of short-lived nuclides with low production rates and half-lives $> 100\,\mathrm{ms}$ with relative uncertainties of about 10^{-8}. Applications for these precision mass measurements include atomic, nuclear and neutrino physics.
The setup of the experiment includes a 6 T superconducting coldhead-cooled magnet, which ensures transportability to different radioactive beam facilities. There, this setup enables mass measurements of, for example, heavy or superheavy nuclides that are produced only in tiny quantities of a few ions per hour. To deal with these low production rates a single trap is planned to be used for cooling the ion's motions with a modified dynamic buffer-gas cooling technique as well as for measuring the ion's motional frequencies. To make such a combination of two techniques in one trap feasible, a fast piezo valve is being developed, which enables a rapid and precisely timed helium injection into the Penning trap, followed by a fast helium release to be directly able to measure in the same trap. The latter is going to be realized by the developed rotating-disc approach. The cooling of the ion's motions and the measurement of its motional frequencies in the same trap increases the overall efficiency by avoiding the ion transport stage between different traps.
In addition to the development of the dynamic cooling method, the setup and initial test measurements of the PILOT-Trap mass spectrometer developed in this work are presented. These range from the initial detection of ions at the detector, through the storage and cooling of ions, to the performance of phase-sensitive measurements.

Entwicklung des neuartigen transportablen online Massenspektrometers PILOT-Trap mit dynamischer Puffergas-Kühlung für gespeicherte Ionen

Das neue, transportable PILOT-Trap Experiment hat das Ziel, Massen von kurzlebigen Nukliden mit geringer Produktionsrate und Halbwertzeiten $> 100\,\mathrm{ms}$ mit einer relativen Unsicherheit von etwa 10^{-8} zu messen. Anwendungen finden diese Präzisionsmassendaten beispielsweise in der Atom-, Kern- und Neutrinophysik.
Der Aufbau des Experiments beinhaltet einen 6 T Magneten, welcher durch einen Kaltkopf gekühlt wird und damit den Transport zu verschiedenen Anlagen, an den Radionuklide produziert werden, ermöglicht. Dort sind mit diesem Aufbau Massenmessungen von beispielsweise schweren oder superschweren Nukliden möglich, die nur in winzigsten Mengen von wenigen Ionen pro Stunde produziert werden. Aufgrund dieser geringer Produktionsraten ist es geplant, die Kühlung der Ionenbewegung sowie das Messen der zugehörigen Bewegungsfreuqenzen in einer einzigen Penningfalle zu vereinen. Hierfür wurde ein Piezo-Ventil entwickelt, welches einen schnellen und zeitlich präzisen Helium Einlass in die Penning Falle ermöglicht. Anschließend folgt eine schnelle Helium Freisetzung aus der Falle mithilfe des entwickelten Rotierende-Scheibe Ansatz, um direkt die Messung der Frequenzen in derselben Falle durchführen zu können. Diese dynamische Kühlung der gespeicherten Ionen erhöht die Effizienz des Massenspektrometers, indem auf den eigentlichen Transport zwischen Kühlfalle und Messfalle verzichtet wird.
Zusammen mit der Entwicklung der dynamischen Kühlmethode werden der Aufbau und erste Testmessungen des in dieser Arbeit entwickelten PILOT-Trap Massenspektrometers präsentiert. Diese reichen vom anfänglichen Nachweis der Ionen am Detektor, über das Speichern und Kühlen von Ionen bis hin zur Realisierung von phasensensitiven Messungen.

Contents

0.1 List of Figures

0.2 List of Tables

1 Introduction

According to *Einstein's* famous equation $E = mc^2$ the mass m of an atom is linked to its energy E via the speed of light constant c. The total mass of the atom is therefore made up of the masses of its fundamental building blocks of protons, neutrons and electrons together with their binding energies, interactions, relativistic shifts and structure effects. This makes the atomic mass a unique fundamental property like the fingerprint of a human being.

High-precision mass measurements of nuclides far away from stability [1, 2] find broad application in nuclear physics research by providing insights into the physics of fundamental interactions and the nuclear structure. This contributes to a better understanding of the rapid neutron-capture (r-) and rapid proton-capture (rp-) process for nuclear astrophysics [3]. Improvements on nuclear mass measurements lead to the development of the nuclear shell model [4] in analogy to the electron shell model of an atom. For this, the two-neutron separation energy S_{2N} is used to investigate the shell structure and separation energies, since this quantity is not affected by the seesaw effect in energy caused by the pairing of two neutrons. The measured shell closures lead to the discovery of the magic numbers of neutrons $N \in \{2, 8, 20, 28, 50, 82, 126\}$ and protons $Z \in \{2, 8, 20, 28, 50, 82\}$.

As an illustration of the importance of high-precision mass measurements to nuclear physics let us consider measurements of the masses of transuranium nuclides for the search for the island of stability. High-precision mass measurements of lighter end products of the α-decay chains of superheavy elements would lead to the determination of superheavy nuclei masses, which could enroute to the mysterious island of stability. This is predicted to be far above uranium around the proton number $Z \approx 120$ and the neutron number $N \approx 184$ [5, 6]. Since the determined α-decay often includes excited states, the reconstruction from decay chains introduces uncertainties, making it difficult to allocate the position of the next shell closure. Thus, direct mass measurements of transuranium nuclides are desired to reveal deeper insights into the nature of nuclear interactions [7].

Even though superheavy elements up to $Z = 118$ can be produced in challenging experiments at radioactive ion beam (RIB) facilities [8, 9, 10], the production rate of these are very small - for example, one atome per week for the element with $Z = 112$ [7]. That is the reason why precision mass spectrometers have to be equipped with high sensitivity and high mass-resolving power. Therefore, the device of choice is the Penning trap [11], which is utilized nowadays at RIB facilities worldwide [1] and enables measurements with relative uncertainties on the order of 10^{-9} for radio nuclides [12] and even below 10^{-11} for stable elements [13]. The development of gas-filled stopping chambers [14] and improved ion-beam manipulation made it

possible to store products from fusion-evaporation reactions and projectile fragmentation in Penning traps [15, 16] so that rare isotopes of so far discovered elements are now accessible. This was shown with the measurement of transfermium elements at SHIP-Trap [17].

At the *Max Planck Institut for Nuclear Physics* (MPIK) in Heidelberg, the novel Penning-trap based "**P**hase-**I**maging-**L**ocated-in-**O**ne-**T**ransportable" (PILOT-) Trap mass spectrometer was constructed within the framework of this thesis, which aims to address the nuclear structure research on exotic isotopes. The goal was to design a transportable, online mass spectrometer to measure masses of short-lived nuclides with low production rates and half-life times down to 100 ms with relative uncertainties of about 10^{-8}.

The biggest problem in measuring properties of superheavy nuclides is their low production rates. Therefore, the mass spectrometer has to provide high efficiency to make measurements at different RIB facilities feasible. Since the beamtime at RIB facilities is limited, most of this offered time needs to be invested into the measurements. That is the reason why the number of parameters, which have to be optimized before every measurement has to be reduced to minimize the time of optimization. Thus, the design of an efficient mass spectrometer was of highest priority in this research project. The second priority has to be the reduction of the measurement's duty cycle time, to enable also mass measurements of short-lived isotopes.

Therewith, the goal of this master thesis was to construct a transportable online mass spectrometer using a Penning trap with relative uncertainties on the order of $\leq 10^{-8}$, which should additionally allow to measure short-lived isotopes with half-lives as low as 100 ms.

Experiments like SHIPTRAP (located at GSI) or ISOLTRAP (located at CERN) belong to the world's leading online mass spectrometers, targeting to measure the mass of radio-nuclides. Both experiments include the cooling of ions in one Penning trap, followed by the transport towards a second measurement trap. This transportation and the following centering of the ions in the measurement trap were identified as the most inefficient points, since this needs additional optimization with the ions of interest.

For that reason, the goal is to merge the two traps for buffer-gas cooling and precision measurement. Thus, the trap has to operate in two regimes. In phase one, it works as a cooler trap for a reduction of the ion's motional amplitudes. In phase two, it operates as a measurement trap for the determination of the frequencies of the ion's motions. Therefore, the typically used static buffer-gas cooling in one trap has to have the ability to be adjusted dynamically.

For this reason, a piezo valve was developed, which enables a fast and precisely-timed helium injection into the Penning trap. In closed mode it offers a small leakage rate to enable precision measurements without the distortion of buffer-gas atoms. To reduce the measurement duty cycle time to enable measurements on short-lived radioactive isotopes a rapid helium release must take place. This is to be achieved

with the developed rotating-disc approach.

In this project a 6 T superconducting coldhead-cryo-cooled magnet is used, which enables the transport to different radioactive beam facilities. Suitability investigations of this magnet to perform high-precision mass measurements constitute part of this work. With this, the transportable online mass-spectrometer PILOT-Trap was constructed to enable phase-sensitive measurements in the framework of this master thesis. In addition, the development of a piezo valve and the rotating disc approach to realize dynamic buffer-gas cooling is presented.

Structure of this thesis

In this thesis, the development of the novel transportable PILOT-Trap experiment is presented. Chapter 2 outlines the basic physics of Penning traps required for the measurement of the cyclotron frequency of the stored ions. In chapter 3, the different measurement techniques to realize mass measurements on short-lived nuclides are introduced. Chapter 4 presents the construction of the PILOT-Trap set-up. This chapter gives an overview of the built-in devices together with measurements of the magnetic field homogeneity and vibrations of the magnet. In addition, the implemented position readout with the delay-line detector is explained, followed by the description of the written control system. After the description of the experimental setup, chapter 5 presents the implementation of the measurement methods presented in chapter 3 using rubidium ions of an offline ion-source. The results ranging from the initial detection of ions at the detector, through trapping and cooling, to the final realization of a phase-sensitive measurement are presented. Next, the dynamic buffer-gas cooling technique is introduced in chapter 6. The development of the piezo valve is described, which enables a fast and precisely timed injection of helium into the Penning trap. In addition, simulation results for the rotating-disc approach are presented, which leads to shorter helium release times and therewith enables measurements on shorter-lived nuclides. The upcoming improvements are outlined in the following chapter 7, including the intent to perform cryogenic buffer-gas cooling. Finally, chapter 8 concludes this work with a summary and outlook, together with the description of the current status of PILOT-Trap.

2 Penning Trap

2.1 Hyperbolic Penning Trap

A Penning trap is a device to store a charged particle in a well-definite volume. As Samuel Earnshaw proved, it is not possible to store an ion stationary in a pure and static magnetic or electric field configuration [18]. Therefore Penning traps make use of a strong static homogeneous magnetic field B superimposed with a static quadrupole electric potential E. Because of the Lorentz force

$$\vec{F_L} = q(\vec{E} + \vec{v} \times \vec{B}) \quad , \tag{2.1}$$

a particle with mass m, charge q and velocity v is forced to move on a circular path with the cyclotron frequency

$$\omega_c = \frac{q}{m} B \quad . \tag{2.2}$$

With that, its motion is confined to the plane that is perpendicular to the magnetic field lines (xy-plane). The axial movement in z-direction is restricted by the weak electrostatic quadrupole E-field, which is produced by hyperbolic shaped electrodes, which are symmetric with respect to the z-axis. The corresponding electric potential writes:

$$\Phi(\vec{r}) = \frac{V_0}{2d^2}\left(z^2 - \frac{x^2+y^2}{2}\right) = \frac{V_0}{2d^2}\left(z^2 - \frac{\rho^2}{2}\right) \quad , \tag{2.3}$$

with $\phi = \sqrt{x^2+y^2}$ being the radial coordinate. V_0 is the voltage difference between the ring electrode and the end-cap of the Penning trap (see fig. 2.1) and is thus the potential barrier for the stored ion. The letter d describes the characteristic length of the Penning trap and is given by:

$$d^2 = \frac{1}{2}\left(z_0^2 + \frac{\rho_0^2}{2}\right) \quad . \tag{2.4}$$

.

With $\vec{E} = -\vec{\nabla}\Phi$ and eq. (2.3) the equation of motion becomes

$$\begin{pmatrix} \ddot{x} \\ \ddot{y} \\ \ddot{z} \end{pmatrix} = \frac{qV_0}{2d^2} \begin{pmatrix} x \\ y \\ -2z \end{pmatrix} + \frac{qB}{m} \begin{pmatrix} \dot{y} \\ -\dot{x} \\ 0 \end{pmatrix} \quad . \tag{2.5}$$

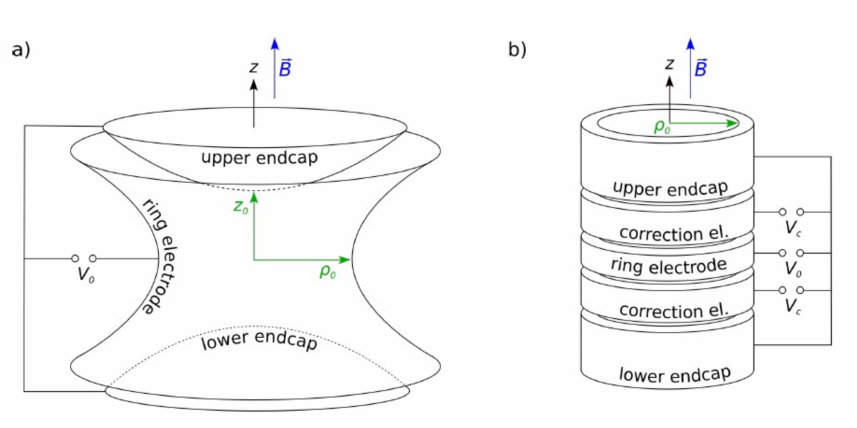

Figure 2.1: *Hyperbolic and cylindrical Penning trap composition of electrodes* a) displays a Penning trap consisting out of hyperbolically shaped electrodes to generate the electrostatic quadrupole field. Today used Penning traps are an assembly of stacked open cylindrical electrodes, which is displayed in b) and produces in first proximity a corresponding potential to a). Figure taken from [19].

By looking at the z component of the equation of motion, one can directly identify this as a harmonic oscillator with the axial motion frequency

$$\omega_z = \sqrt{\frac{qV_0}{md^2}} \quad . \tag{2.6}$$

.

One can see in eq. (2.5) that the ion motion in the xy-plane (radial motion) is a superposition of two eigenmotions, which can be separated by the ansatz $u = x + iy$ and $u = e^{i\omega t}$ towards the modified cyclotron motion with frequency ω_+ and the magnetron motion with frequency ω_-, so that their frequencies become

$$\omega_\pm = \frac{\omega_c}{2} \pm \sqrt{\frac{\omega_c^2}{4} - \frac{\omega_z^2}{2}} \quad . \tag{2.7}$$

From the formulas for the eigenfrequencies (eq. (2.6), eq. (2.7)) the conditions of storing an ion in a Penning trap can be derived as $\frac{qV_0}{d^2} > 0$, as well as $\omega_c^2 > 2\omega_z^2$.

Finally the ion motion in a Penning trap is a superposition of these three eigenmotions, displayed in figure 2.2.

For the magnitude of the eigenfrequencies applies:

$$\omega_c \gtrapprox \omega_+ \gg \omega_z \gg \omega_- \quad . \tag{2.8}$$

Combining the equations of eigenfrequencies, one gets the following formulas to determine the free cyclotron frequency of the ion:

$$\omega_c = \omega_+ + \omega_- \quad , \tag{2.9}$$

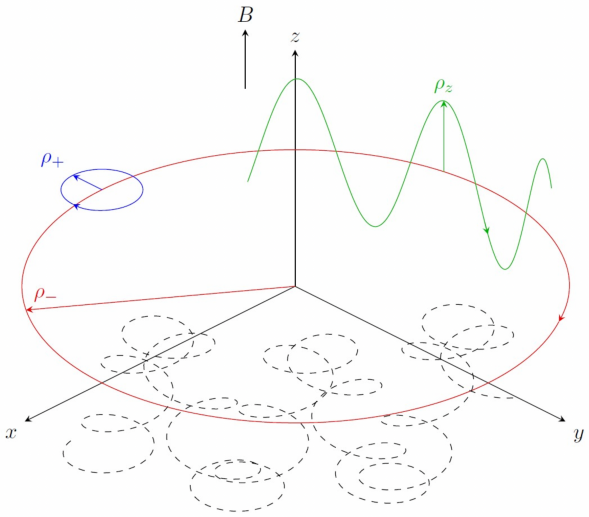

Figure 2.2: *Visualization of the three eigenmotions of a stored ion in a Penning trap* The superposition of the magnetron (red), axial (green) and modified cyclotron motion (blue) is displayed as the dashed line. Figure taken from [19].

$$\omega_c^2 = \omega_+^2 + \omega_-^2 + \omega_z^2 \quad . \tag{2.10}$$

The latter equation is known as the invariance-theorem [20], derived by Brown and Gabrielse, which holds also for imperfect traps in the meaning of small misalignment angle between the z-axis and the magnetic field $\vec{B}$.

Finally, since the cyclotron frequency ω_c of an ion is directly proportional to its charge-over-mass ratio $\frac{q}{m}$, and this cyclotron frequency can be determined by measuring the frequencies of the eigenmotions, the mass of the ion of interest m_{IOI} can be determined, provided the magnetic field strength is known. To get rid of the contribution of the magnetic field and to determine the final atomic mass $m_{IOI,a}$ of the ion of interest (IOI) an alternating measurement scheme of IOI and a reference ion (ref) is used. Therefore the cyclotron frequency ratio $r_{ref,IOI} = \frac{\omega_{c,ref}}{\omega_{c,IOI}} = \frac{m_{IOI}}{m_{ref}}$ is determined, with $m_{IOI/ref}$ being the mass of the respective singly charged ion. The final atomic mass of the particle of interest is corrected by the electron mass m_e and the respective binding energy of the missing electron E_e, thus calculated with:

$$m_{IOI,a} = r_{ref,IOI}(m_{ref} - m_e - E_{e,ref}) + m_e + E_{e,IOI} \quad . \tag{2.11}$$

The determination of relative masses to get rid of the magnetic field strength and the fact that a frequency is currently the most precisely measurable quantity enable relative mass measurements with a precision in the order of 10^{-12} for stable masses at PENTATRAP [13]. For radionuclides relative mass precision in the order of 10^{-9} [12] are routinely achieved, limited by the short measurement time. Such low uncertainties reachable in mass measurements on a wide spectrum of nuclides make the Penning trap so unique and the technique of choice for mass measurements.

2.1.1 Manipulation of Ion Motion

As shown above, the ion eigenmotions in an ideal Penning trap represent three uncoupled harmonic oscillators. Considering the ion's energy in the quantum-mechanical picture (see figure 2.3), this can break down to three quantum-mechanical harmonic oscillators. Each of these energy levels can be manipulated via the irradiation of external radio-frequency (rf)-fields. With this, a dipole excitation on the frequency of the corresponding ion motion can be executed to enlarge the amplitude of this motion. One can also couple two ion motions with a quadrupole rf excitation on the sum or the difference of the frequencies of the respective motions. This will be described in detail in the following subsections. It has to be noted that since the magnetron motion is metastable, it behaves differently than the other two ion motions. Looking at the energy diagram in figure 2.3 one sees a negative energy contribution of the magnetron motion, which results from the electrostatic potential having its maximum in the center of the radial plane (see eq. (2.3)). Thus an enhancement of the magnetron radius is equal to the loss of potential energy.

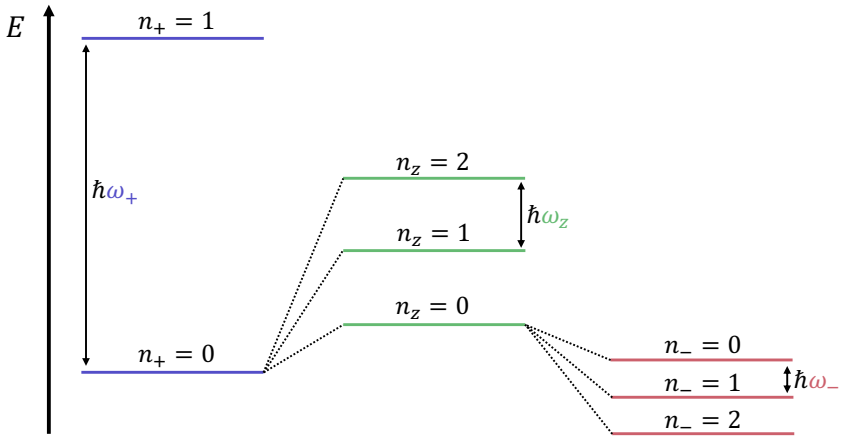

Figure 2.3: *Energy diagram of a stored spinless ion in a Penning trap with the three harmonic oscillator levels*
The contribution of each eigenmode to the total energy of a stored spinless ion in a Penning trap is displayed. One notices the negative energy contribution of the magnetron motion to the total energy of the ion. Level splitting scaling is adjusted for illustration.

Dipole Excitation

The irradiation of a dipole rf-field $\vec{E}$ at position $\vec{x}$ with frequency ω_{rf} and phase ϕ_{rf} is described by:

$$\vec{E} = \frac{U_d}{a} \sin\left(\omega_{rf} t + \phi_{rf}\right) \vec{x} \quad . \tag{2.12}$$

It can be applied between ring electrode segments to manipulate the radial motions or between endcups to change the axial motion of the ion. Thereby the amplitude enhancement is proportional to the excitation time T_{rf} and the excitation amplitude U_d. The dipole excitation is used to enhance the amplitude of a chosen motion, which could be used to remove contaminated ions in the trap, by letting them collide with the trap, or to imprint a certain phase on the motion.

Quadrupole Excitation

This excitation is used to couple individual eigenmotions in the Penning trap. In the case of coupling both radial modes, the quadrupole field $\vec{E}$ with frequency ω_{rf} is irradiated on opposite segments of the four split ring electrode respectively with

$$\vec{E}_{i,j} = \frac{2U_q}{a^2} \sin\left(\omega_{rf} t + \phi_{rf}\right) \left(x_i \vec{e_j} + x_j \vec{e_i}\right) \quad . \tag{2.13}$$

To couple the radial motions, x_i and x_j have to correspond to the x- and y-coordinates. The red sideband coupling of the radial motions with the resonant frequency $\omega_{rf} = \omega_c = \omega_+ + \omega_-$ would lead to a periodical conversion of the radii ρ_+ and ρ_-, displayed in figure 2.4. With this the amplitudes vary with $\propto \cos(\Omega t + \Phi)$ with the *Rabi frequency*

$$\Omega = \frac{qU}{2md^2\sqrt{\omega_+\omega_-}} \quad , \tag{2.14}$$

which describes the strength of the coupling. In this process the phase shift between the radial trapping modes is shifted by factor $\pi/2$. This conversion of magnetron motion into only modified cyclotron motion is shown in figure 2.4 a) and the process vice versa in figure 2.4 b). The conversion time

$$T_{conv} = \pi \frac{m}{q} \frac{a^2}{2U_q} (\omega_+ - \omega_-) \approx \pi \frac{a^2}{2U_q} B \tag{2.15}$$

is in approximation of $\omega_+ \gg \omega_-$ and $\omega_+ \approx \omega_c$ determined by the irradiation amplitude U_q and the magnetic field strength B. This conversion of radial modes with the red sideband coupling is the key element for realizing the buffer-gas cooling in a Penning trap, which will be described in section 3.1.

Instead, if the blue sideband at $\omega_{rf} = \omega_c = \omega_+ - \omega_-$ is chosen for the coupling, both amplitudes of the two coupled modes are exponentially increasing after certain transient oscillations. This behavior can be understood on a quantum-mechanical level, when looking at the cooling (stimulated emission) and heating (absorption) processes, where the heating is superior. This is treated in more detail in [21].

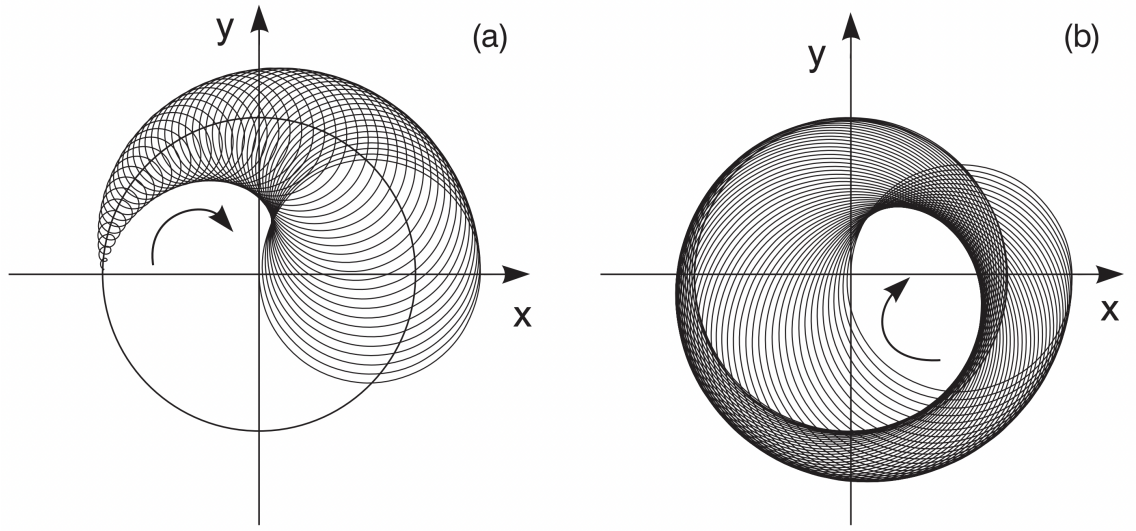

Figure 2.4: *Conversion of radial motions by red sideband coupling*
First and second half of the conversion of radial modes are shown, when performing red sideband coupling by applying a quadrupole rf-field with the resonant frequency $\omega_{rf} = \omega_c = \omega_+ + \omega_-$. The pictured circle in a) indicates the start radius of the magnetron motion, which equals the end of the conversion of b). Figure taken from [22].

2.2 Cylindrical Penning Trap

Instead of using an ideal hyperbolic trap a stack of cylindrical electrodes can be used to generate the quadrupole electrostatic field. An assembly of such a stack can be seen in figure 2.1 b). As in the hyperbolic trap, the ring electrode lies on a potential V_0 with respect to the end caps. In between there are correction electrodes with a potential V_c relative to the endcaps for setting the tuning ratio $TR = \frac{V_c}{V_0}$. Such a stack of electrodes creates a symmetric potential

$$\Phi(z) = V_0 \sum_n C_{2n} z^{2n} = V_0(C_2 z^2 + C_4 z^4 + C_6 z^6 + ...) \tag{2.16}$$

along the z-axis. Thereby $C_2 = (2d)^{-1}$. The geometry of the trap can be designed in such way, that C_2 is stable for different V_c. This condition is called *orthogonal*.

An optimized tuning ratio can be found, so that the higher order correction terms C_4 and C_6 vanish, which would else lead to anharmonicities in the axial motion. With this tuned condition the trap is called to be *harmonic*.

3 Measurement Techniques

This chapter gives an overview of the basics of measurement techniques used to carry out high-precision mass measurements on short-lived nuclides with Penning traps. A typical experimental setup to realize such a measurement is schematically displayed in figure 3.1.

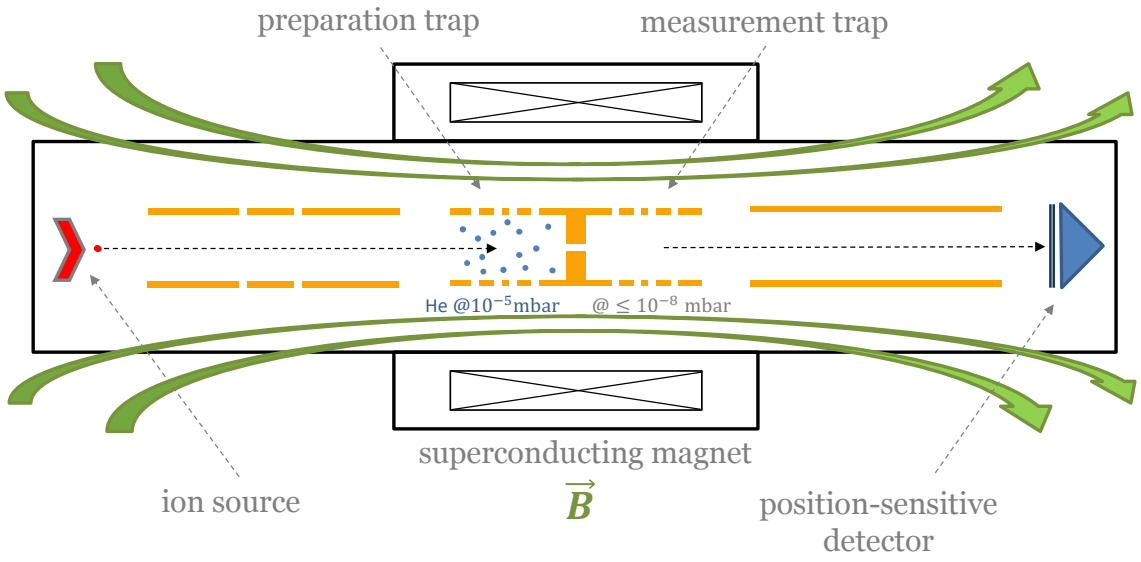

Figure 3.1: *Typical Penning-trap experimental setup for mass measurements on sort-lived nuclides*
This illustration displays the current typical experimental setup to realize mass measurements with Penning traps. Therefore ions from an ion source are transported via ion optics into the preparation trap filled with helium, where the buffer-gas cooling takes place. After cooling, the ions are transported towards the measurement trap through a pumping barrier, whose purpose is to establish low ambient pressure in the following beamline to enable measurements. In the measurement trap the cooled ions get radially excited and ejected towards the detector to perform mass measurements (for details see text).

Every setup needs an ion-source to produce the ions of interest. This could be a built-in offline ion-source or ions can be delivered from an online facility (symbolized on the left in red in figure 3.1). These ions are transported to the Penning trap setup by means of ion optical elements. In currently used online setups at radioactive ion beam facilities the ions are first trapped in a preparation Penning trap, where their

motional amplitudes are reduced with the mass-selective buffer-gas cooling technique [23], which will be introduced in chapter 3.1. This process is called "*cooling of ion motions*" or for short "*ion cooling*". In principle this technique is based on energy exchange by collisions of the ions and the buffer-gas (commonly helium) atoms with which the preparation trap is filled to a pressure of 10^{-5} to 10^{-4} mbar.

To perform mass measurements with the cooled ions based on radial excitation's (see chapter 2.1.1) a smaller ambient pressure is needed. Therefore in currently used setups the measurement schemes are performed in a measurement trap, another Penning trap next to the preparation trap separated by a pumping barrier to achieve the measurement pressure.

For mass measurements with Penning traps two established techniques can be used. One is the time-of-flight ion-cyclotron-resonance technique (ToF-ICR) described in chapter 3.2, the other is the phase-imaging ion-cyclotron-resonance (PI-ICR) explained in section 3.3. Both are based on radial excitations of the ions before they are ejected in the direction of the position sensitive detector, leading to a time-of-flight measurement in the first or a phase measurement in the second method. Later will be the method of choice, since it outperforms the ToF-ICR method in such aspects as achievable precision and mass resolving power (see figure 3.7). Furthermore, the determination of the cyclotron frequency with the ToF-ICR method requires at least a few ten ions to form a proper resonance spectrum, whereas just a few ions are sufficient with the phase measurement using the PI-ICR method.

3.1 Buffer-Gas Cooling

This cooling method for stored ions is based on multiple collisions with a light gas (commonly helium) used as a buffer, so that the ion temperature converge to that of the injected buffer-gas. Therefore the trap is filled with helium gas at a typical pressure of about 10^{-5} to 10^{-4} mbar [24]. Collisions reduce the amplitudes of the cyclotron and axial motion, whereas the magnetron amplitude grows, because of its metastable behavior (see fig. 2.3).

Because of the hierarchy of frequencies (see eq. (2.8)), the cyclotron motion gets cooled the fastest, since a higher frequency implies a higher cross-section with the buffer-gas. That is why the increase of the magnetron amplitude happens very slow compared to the damping of the modified cyclotron motion. This is illustrated in figure 3.2 a).

In order to reduce the magnetron amplitude as well, a quadrupolar rf-field with the frequency $\omega_{rf} = \omega_c = \omega_+ + \omega_-$ is used to convert the magnetron motion into the cyclotron motion, as described in chapter 2.1.1. Because of this induced Rabi-oscillation of both radial modes and the damping effect of the buffer-gas on the cyclotron motion the magnetron radius is now also shrinking, resulting in a constriction of the ion distribution in the center, which is called the *cooling spot* and displayed in figure 3.2 b).

The only condition to ensure this cooling technique is that the conversion time

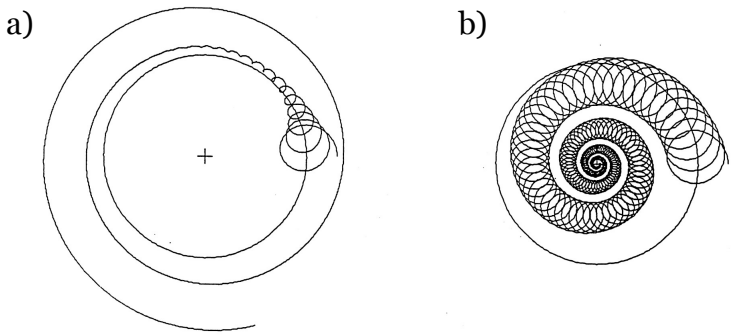

Figure 3.2: *Damping effect on radial motions of buffer-gas cooling without and with red sideband coupling*
The cross represents the center of the trap.
a) displays the fast damping of the modified cyclotron motion together with a slow magnetron blow up, induced by the damping through collisions with the buffer-gas.
The buffer-gas cooling with the effect of the additional quadrupole field with frequency $\omega_{rf} = \omega_+ + \omega_-$ is illustrated in b). Here both motions are cooled and both radii are decreased to the center forming the so-called *cooling spot*. Figure taken from [23].

between the radial motions (see eq. (2.15)) has to be faster than the magnetron blow-up. Thereby the cooling time can be lowered to a few milliseconds [24] by optimizing the helium pressure.

Because of this quadrupolar excitation with ω_{rf}, the buffer-gas cooling gets mass dependent (see eq. (2.2)). Unwanted ions with a different charge-to-mass ratio will undergo a magnetron amplitude blow up during the cooling.This blow up can be used to remove the unwanted ions, when transporting the ions through a pumping barrier with smaller radius than the gained magnetron amplitude, so that the unwanted ions hit the wall whereas the ions of interest are passing the barrier.

The above is the basic of buffer-gas cooling, which will now be looked up in more detail to finally derive the cooling time constants in the macroscopic picture. The microscopic description including the statistical nature of the collisions can be found in [25].

The interaction of heavy ions and buffer-gas at low energies corresponds to that of an ion and the dipole moment it induces in the buffer-gas atoms. Averaged over time, these interactions causes small changes in the ions energy for each collision, which is similar to a viscous drag [23]. Thus the effect of buffer-gas on the motion of the ions in the Penning trap can be obtained analytically, if the damping force

$$\vec{F}_d = -\gamma m \frac{d\vec{r}}{dt} \tag{3.1}$$

is added to the equation of motion (see eq.(2.5)). A realistic expression for the damping constant γ can be found in the classical theory of *ion mobility*, where a constant drift velocity v_d of an ion in a gaseous environment under the impact of an electrical field is derived. This can be considered analogue as a linear viscous drag proportional to the ion velocity.

In this model the equation of motion is:

$$m\frac{d\vec{v}}{dt} + \gamma\vec{v} - q\vec{E} = 0 \quad , \tag{3.2}$$

which can be solved with the variation of parameters. This drift velocity v_d is proportional to the electric field strength E_{el} and to the characteristic ion mobility K:

$$v_d = K \cdot E_{el} \quad . \tag{3.3}$$

In the case of the constant drift velocity, the damping force equals the electric force, transforming eq. (3.2) to

$$\gamma = \frac{q}{m}\frac{1}{K} \quad , \tag{3.4}$$

which leads to the derivation of the damping constant γ being inverse proportional to the ion mobility K.

Since the mobility K is dependent on pressure p and temperature T, one finds in literature [26] the value of the reduced mobility K_0, which has the following relation to K:

$$K_0 = K \cdot \frac{273.16\,\mathrm{K}}{T}\frac{p}{1013\,\mathrm{mbar}} \quad . \tag{3.5}$$

After the damping term is now derived, the impact on the ion movement gets investigated. The radial motion of a trapped ion consists out of a linear superposition of the modified cyclotron motion ω_+ with radius r_+ and the magnetron motion with frequency ω_- and radius r_- and represent the cartesian coordinates with:

$$x = r_+ \sin(\omega_+ t) + r_- \sin(\omega_- t) \quad , \quad y = r_+ \cos(\omega_+ t) + r_- \cos(\omega_- t) \quad . \tag{3.6}$$

By solving the equation of motion including the damping force F_d from eq. (3.1) and eq. (3.4) one derives the radial motions with initial amplitudes $r^0_{+,-}$ to be:

$$r_\pm(t) = r^0_\pm \exp(\mp\alpha_\pm t) \tag{3.7}$$

with

$$\alpha_\pm = \gamma\frac{\omega_\pm}{\omega_+ - \omega_-} \quad . \tag{3.8}$$

Therewith the cooling time constant α depends on the buffer-gas pressure and temperature, as well as the trapping parameters included in the terms of the frequencies.

Finally the circular spot radius in the radial (xy-) plane can be estimated by the FWHM of spatial distribuition $2\Delta r$ [24] with

$$\Delta r \approx \frac{2.35}{\omega_+}\sqrt{\frac{k_B T}{2m}} \approx \frac{2.35}{\omega_c}\sqrt{\frac{k_B T}{2m}} \quad , \tag{3.9}$$

whereby T represents the temperature of the buffer-gas. For example this would result in a spot size $2\Delta r \approx 84\,\mu$m of singly charged ions of mass 85 u (^{85}Rb) for the PILOT-Trap experiment with a 6 T magnetic field at room temperature.

3.2 Time-of-Flight Ion-Cyclotron-Resonance Technique (ToF-ICR)

Because of a fast measurement duty cycle ($60\,\text{ms} \leq T_{rf} \ll 1\,\text{s}$) [27] and a high relative mass precision of $\delta m/m \sim 10^{-9}$ [27], the time-of-flight ion-cyclotron-resonance technique [28] is a worldwide established method of mass spectrometry of short-lived nuclides. In this technique, the dependence of the time of flight of an ion through the gradient of the magnetic field on the ion's orbital magnetic moment μ is used. The magnetic moment of a stored ion in a Penning trap is given by:

$$|\mu| = \left|\frac{q}{2}(r_+^2\omega_+ + r_-^2\omega_-)\right| = \left|\frac{E_r}{B_0}\right| \quad , \tag{3.10}$$

with r representing the radius of the respective motion, E_r the radial kinetic energy of the ion and B_0 being the magnetic field strength in the center of the Penning trap.

The interaction of the magnetic field gradient and the magnetic moment of the ion expresses in an accelerating force $\vec{F} = -\vec{\mu}\nabla\vec{B}$, here:

$$|F_z| = \left|\frac{E_r}{B_0}\frac{\delta B}{\delta z}\right| \quad , \tag{3.11}$$

which is accelerating the ion in the direction of the detector. This means depending on the ion's amplitude of radial motions, the ion is accelerated differently strong from the trap at z_0 towards the detector at z_{det} by the magnetic field gradient, leading to different time of flights, which can be calculated with

$$T(E_r) = \int_0^{z_{det}} dz \sqrt{\frac{m}{2(E_0 - qU(z) + |\mu(E_r)B(z)|)}} \quad . \tag{3.12}$$

After the ions are cooled in the Penning trap (see sec. 3.1) the orbital magnetic moment and therefore the time of flight can be manipulated by a quadrupolar rf-field excitation at the frequency around $\omega_{rf} \approx \omega_+ + \omega_-$. Thereby the amplitude of the magnetron motion is converted in the modified cyclotron motion (see chapter 2.1.1). Because of eq. (3.10) and $\omega_+ \gg \omega_-$ the magnetic moment is maximized,

when $\omega_{rf} = \omega_+ + \omega_-$ and a full conversion of motions happened, and subsequently the time-of-flight towards the detector is minimized. The time of flight spectrum is shown in figure 3.3(a) containing one pronounced minimum, which represents the cyclotron frequency of the ion. The surrounding smaller minima are caused by the Fourier-transformation of the square-excitation pulse in the time domain [29].

The Ramsey technique applied on this measurement technique made it possible to even lower the full-width-half-maximum (FWHM) [30]. In this process the one excitation pulse is divided in two short excitation pulses with equal amplitude and duration, where the integral area of the one conversion π-pulse is equal to the integral area of the two $\pi/2$-pulses. This results in an ToF-resonance with almost equally distributed deep minima, which show reduced FWHM, pictured in figure 3.3 (b).

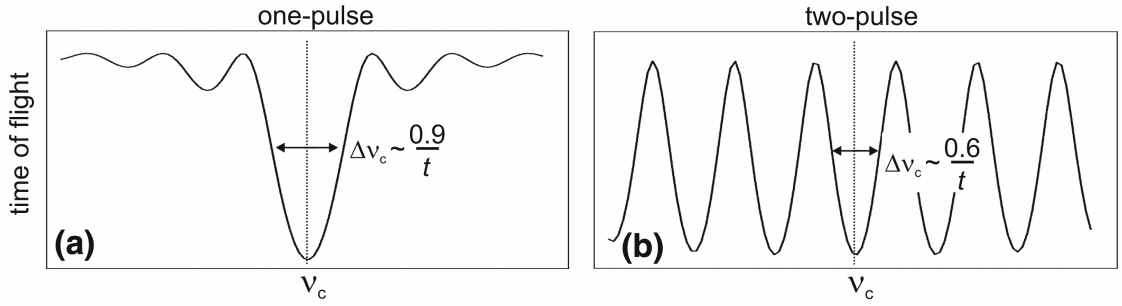

Figure 3.3: *Time of flight resonance using different excitation pulses*
a)ToF-resonance with one continuous quadrupole excitation *pi*-pulse.
b)ToF-resonance with two $\pi/2$-pulses with equal amplitude and duration using the Ramsey technique. Figure taken from [24].

The mass-resolving power of the ToF-ICR [24][29]

$$R_{ToF} = \frac{m}{\Delta m} = \frac{\omega_c}{\Delta\omega_c} \propto \omega_c T_{rf} \tag{3.13}$$

is directly proportional to the measurement time, meaning the total duration of the excitation pattern T_{rf}. Thereby the uncertainty of the cyclotron frequency is proportional to the spot-size Δr defined in chapter 3.1 and inversely proportional to the duration time t and magnetron radius r_-, building with the number of recorded ions N the following relation [24]:

$$\Delta\omega_c \propto \frac{\Delta r}{r_- t\sqrt{N}} \quad . \tag{3.14}$$

Along with a relatively moderate resolving power, the main disadvantage of this measurement technique is the need of at least a few ten ions to obtain a ToF-ICR resonance as compared to just a few ions needed for the determination of the cyclotron frequency with the phase-sensitive PI-ICR technique introduced in the next chapter.

3.3 Phase-Imaging Ion-Cyclotron-Resonance (PI-ICR) Measurement

The phase-imaging ion-cyclotron-resonance (PI-ICR) technique relies on measuring the total phase evolution ϕ_{tot} of the radial motion of a trapped ion in a Penning trap in a measurement time t of excitation free propagation. This total phase is described by

$$\phi_{tot} = 2\pi \cdot n + \phi_i \tag{3.15}$$

with $n \in \mathbb{N}_0$ being an integer number of full turns and $\phi_i \in [0, 2\pi)$ the additional phase. Thus the radial frequency ω_i is determined by:

$$\omega_i = \frac{\phi_{tot}}{t} = \frac{2\pi \cdot n_i + \phi_i}{t} \quad , \tag{3.16}$$

where i represents the index of one of the radial motions. By projecting the ion motion onto a position-sensitive multi-channel-plate (PS-MCP) detector, the resulting image is magnified by the magnetic field gradients between the trap and the detector without influencing the radial motions and its relative positions (see figure 3.4), which is summarized in the multiplication factor

$$G_B = \frac{r_{det}}{r} = \sqrt{\frac{B_z(r,0)}{B_z(r,z_{det})}} \quad , \tag{3.17}$$

where the index *det* indicates the position of the detector.

In the following the measurement principle is presented, which is illustrated in figure 3.4. The previous cooling of the radial motions defines the initial spatial distribution $2\Delta r$, which is referred here as "center" (see section 3.1). This spot can be prepared on a radius r_i with the help of a dipolar excitation with the rf-frequency being one of the radial eigenfrequencies. This is called the reference phase. After a certain propagation time, the ions accumulate the total phase ϕ_{tot}, so that the spot is called the final phase, before the ions are ejected from the trap in the direction of the position-sensitive detector.

The PI-ICR technique enables two measurement schemes, which will be pointed out shortly. For more information see [24].

The first one is the independent measurement of the reduced cyclotron and magnetron frequency and the excitation scheme of this method is shown in figure 3.5. The measurement of the magnetron frequency ω_- equals exactly the measurement principle explained above. To measure ω_+, two steps have to be taken in addition. First the magnetron radius has to be reduced by an dipole excitation before the cyclotron motion is excited to a certain radius r_+. After the free evolution time the modified cyclotron motion has to be fully converted by a π-pulse at the cyclotron frequency ω_c towards the magnetron motion (see chapter 2.1.1). Without this conversion, the spot would be smeared out, caused by the high modified

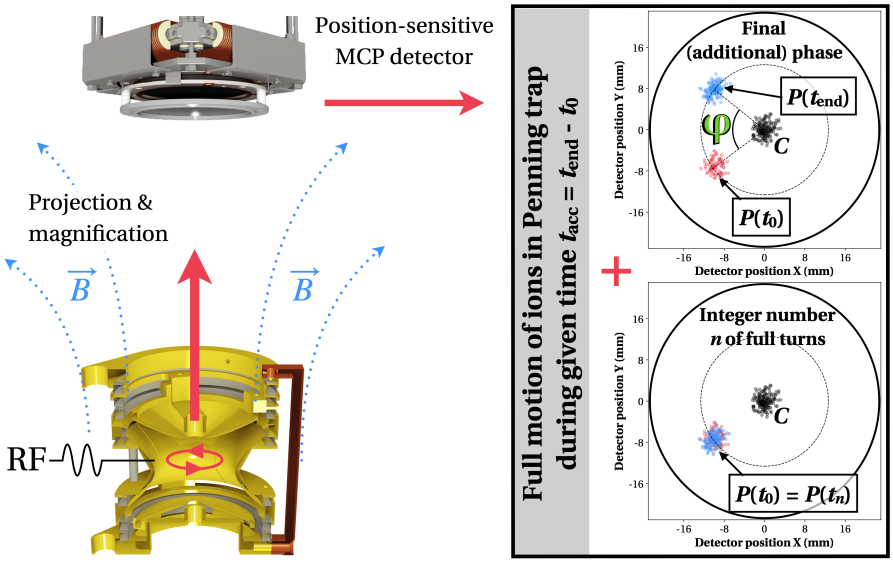

Figure 3.4: *Schematic drawing of PI-ICR setup and phase images*
left: Schematic drawing of PI-ICR setup, which illustrates the magnification of the ion motion caused by the magnetic field gradient.
right: Phase images, with the center pot in the middle, $P(t_0)$ representing the reference phase and $P(t_{end})$ representing the final phase. Figure taken from [27].

cyclotron frequency and the energy distribution in the axial motion, leading to a distribution in the time-of-flight towards the detector. This happens if the FWHM of the time-of-flight spectrum is at least comparable to the period of the modified cyclotron frequency. Note that the angle between the reference and final phase are preserved by the conversion [24].

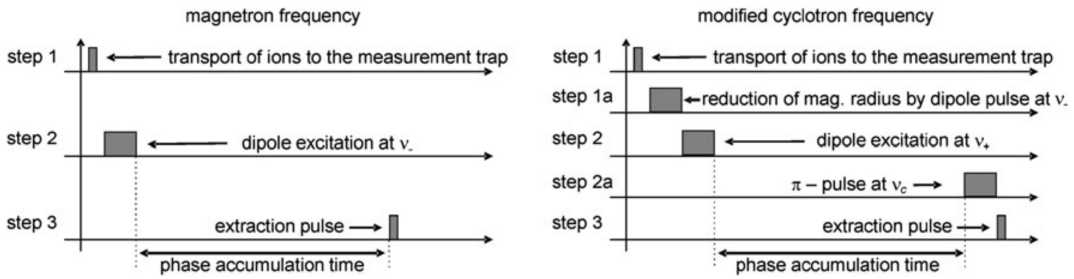

Figure 3.5: *Excitation-pulse scheme (1) for the separate measurement of* ω_+ *and* ω_-
Figure taken from [24].

The second scheme is a direct measurement of the cyclotron frequency ω_c. Therefore this scheme also consists out of two excitation-pulse patterns, shown in figure 3.6. The second pattern equals the modified cyclotron determination pattern of

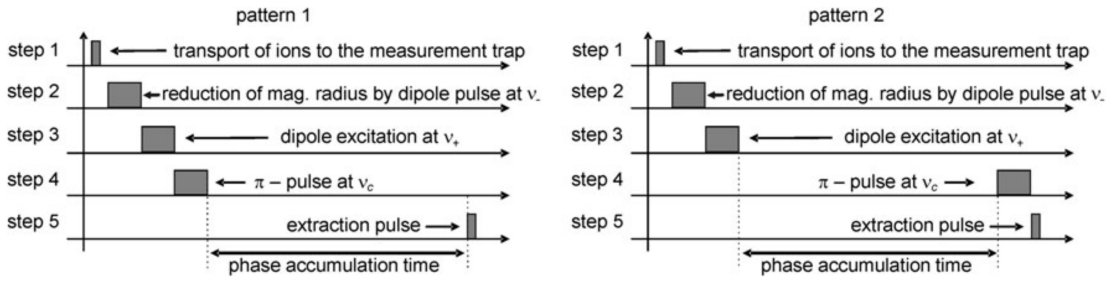

Figure 3.6: *Excitation-pulse scheme (2) for the direct measurement of* ω_c
Figure taken from [24].

scheme one, where the π-pulse with ω_c is applied after the phase evolution time t_1 just before the ejection of the ions out of the Penning trap. The first pattern equals the second one, by first reducing the magnetron radius and than exciting the modified cyclotron frequency. But this time the π-pulse with ω_c is applied right after the excitation of ω_+ and the ions are ejected after the free phase accumulation time t_2. If $t_1 = t_2 = t_{acc}$, the cyclotron frequency ω_c could be determined out of the angle between the phase images of these two patterns by

$$\omega_c = \frac{\phi_c + 2\pi(n_1 + n_2)}{t_{acc}} \quad . \tag{3.18}$$

The latter measurement scheme has the advantage, that it does not need the reference phases, thus reducing the number of ions to half of the ones needed in the first scheme. That is why the second scheme is very suitable for mass spectrometry on short-lived nuclides. Compared to the ToF-ICR technique, this scheme also provides a gain of 40 in resolving power and a gain of 5 in precision [24].

The major advantage in the PI-ICR technique is the high resolving power $R = \omega_c/\Delta\omega_c$, which is needed in this area of research, like for example to resolve low-lying ($< 500\,\mathrm{keV}$) isomeric states [31]. Thereby the uncertainty of the cyclotron frequency is derived in [24] towards:

$$\Delta\omega_c = \frac{2}{\pi t\sqrt{N}} \frac{\Delta r_{det}}{r_{det}} \propto \frac{\Delta r}{r} \quad , \tag{3.19}$$

assuming $\Delta r_{det,-} = \Delta r_{det,+} = \Delta r_{det}$.

The ISOLTRAP experiment located at CERN has implemented the ToF-, the PI-ICR- and the MRToF technique. In [27] the resolving powers of these techniques are compared, whose result is displayed in figure 3.7. There it is shown, that the PI-ICR technique offers the highest mass resolving power for every trapping time. This emphasizes the advantage of using the PI-ICR technique for a high-precision mass spectrometer of short-lived nuclides, like PILOT-Trap will do.

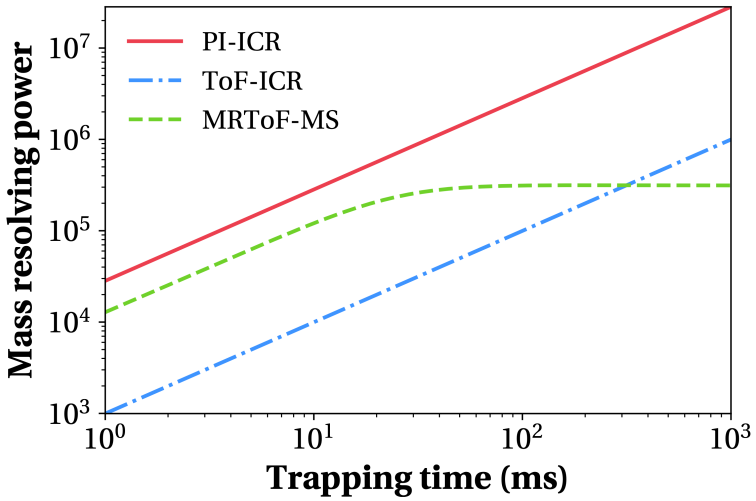

Figure 3.7: *Comparison of resolving power of MRToF, ToF-ICR and PI-ICR at ISOLTRAP*
This graph shows the comparison of mass-resolving powers of ISOLTRAP's MRToF mass spectrometer and the ToF-ICR and PI-ICR technique realized with the precision Penning trap as a function of the trapping time. Figure taken from [27].

3.4 PILOT-Traps Planned Measurement Technique

Having introduced the currently common used Penning trap measurement setup with all used techniques before, the planned measurement technique of PILOT-Trap can now be introduced.

The idea is to combine the preparation and measurement trap into one Penning trap, for which a schematically drawn experimental setup is shown in figure 3.8. Therefore a dynamic buffer-gas cooling technique has to be implemented with the help of developing a fast piezo valve to be able to inject helium in the Penning trap for cooling the ions by opening the valve (displayed in figure 3.8) and obtain the ambient pressure to perform mass measurements in the same trap by closing the valve. The realization of this dynamic cooling technique is described in chapter 6, in which the particularly challenging problem of the fast helium release is addressed.

The advantage of such a setup is the conservation of the cooled ion conditions, which in the commonly used setup can be altered by the transport to the measurement trap, when the electrode symmetry axis is not perfectly aligned to the magnetic field axis. This could lead to an enhanced magnetron radius, which than has to be counteracted by magnetron excitation, for which optimization is needed. In contrast, in this setup the cooling conditions are conserved, since just the buffer-gas is removed from the trap. This increases the overall efficiency, which is important for measuring masses of short-lived nuclides with low production rates.

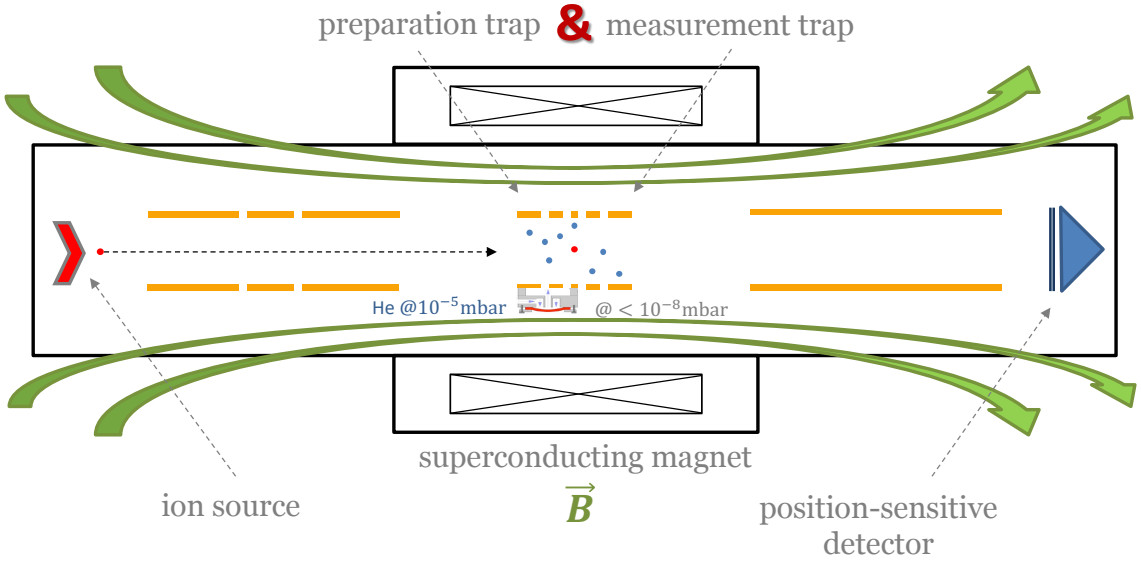

Figure 3.8: *Planned Experimental Setup of PILOT-Trap*
In this setup the idea is to combine the preparation and measurement trap. Therefore a developed fast piezo valve has to be adjusted to the Penning trap, to realize buffer-gas cooling when the valve is opened together with measurements at low ambient pressures, when the valve is closed and the helium got pumped out of the trap. In the schematic drawing the time of cooling is illustrated, where the valve is open.

In addition, for the commonly used setup a magnetic field with two areas of homogeneity is needed. Superconducting magnets with these are not produced anymore, so that one has to combine two magnets in a setup, making the experiment larger and less transportable.

To realize this dynamic buffer-gas cooling a piezo valve for fast and precisely timed helium injection is designed, which is described in chapter 6.1. In addition the helium release is investigated and a new approach to reduce the release time is presented in section 6.2.

The design of the PILOT-Trap experiment to test and realize the above presented measurement techniques, especially the normal buffer-gas cooling as well as the PI-ICR technique, with a transportable coldhead cooled superconducting magnet is shown in the following chapter.

4 PILOT-Trap: Construction and Experimental Setup

4.1 Beamline Design

The PILOT-Trap beamline is shown in figure 4.1 with an additional cut to enable the view on the inner structure. The central component is a coldhead cryogenically cooled 6 T magnet (green, see also chapter 4.2.2) from the company *CRYOGENIGC LTD*, which was converted into a warm bore magnet by adding a bore surrounded by a copper radiation shield. The latter is connected to the 40 K radiation shield of the magnet. The bore contains a trap assembly (see also section 4.5), including a Penning trap (see section 4.2.3) together with drift electrodes. At the end of the right side a position sensitive delay-line detector (displayed in blue together with its holding structure, see also chapter 4.2.4) is placed, whereby its position was chosen to ensure a magnetic environment of ≤ 5 mT as recommended in the manual [32]. Instead of a closed drift tube, a perforated drift electrode is used in front of the detector to improve the pumping cross-section in this volume, since the distance between the last drift tube and detector is only 2 cm. To support the pumping in the volume of the ejection path of the ion, an additional vacuum tube (U-shape) was constructed. On the left side, a rubidium ion source (displayed in red, see also section 4.2.1) is placed. The extension of the beamline on the left is constructed to ensure a magnetic environment of ≤ 5 mT for the turbo-molecular pump *W600P* from *Leybold* (as recommended in the manual [33]) to ensure a reliable run of those with performing a pumping speed of 550 l/s and 570 l/s [33] for helium and nitrogen, respectively.

The whole beamline is mounted on a frame made of extruded aluminum profiles, called support frame in the following, which is equipped with horizontal linear rails. On this support frame three segments (see figure 4.1) of the beamline can be moved. The first segment contains the ion source and the drift tubes. The magnet is mounted on the second segment. The last segment contains the Penning trap, exit drift tubes and detector. The beamline mountings on each segment are height adjustable with the bracket of the magnet holding plate or vacuum crosses and could be tilted as well.

The vacuum tubes of the outer segments are connected towards the magnet with bellows, which have an axial travel range of 50 mm to ensure centering the Penning trap in the homogeneous area of the magnetic field. In addition, the bellows may possibly damp the vibrations of the coldhead cryo-cooled magnet. With the bellows, the height adjustable attachments and the rolling tables on the item frame, all

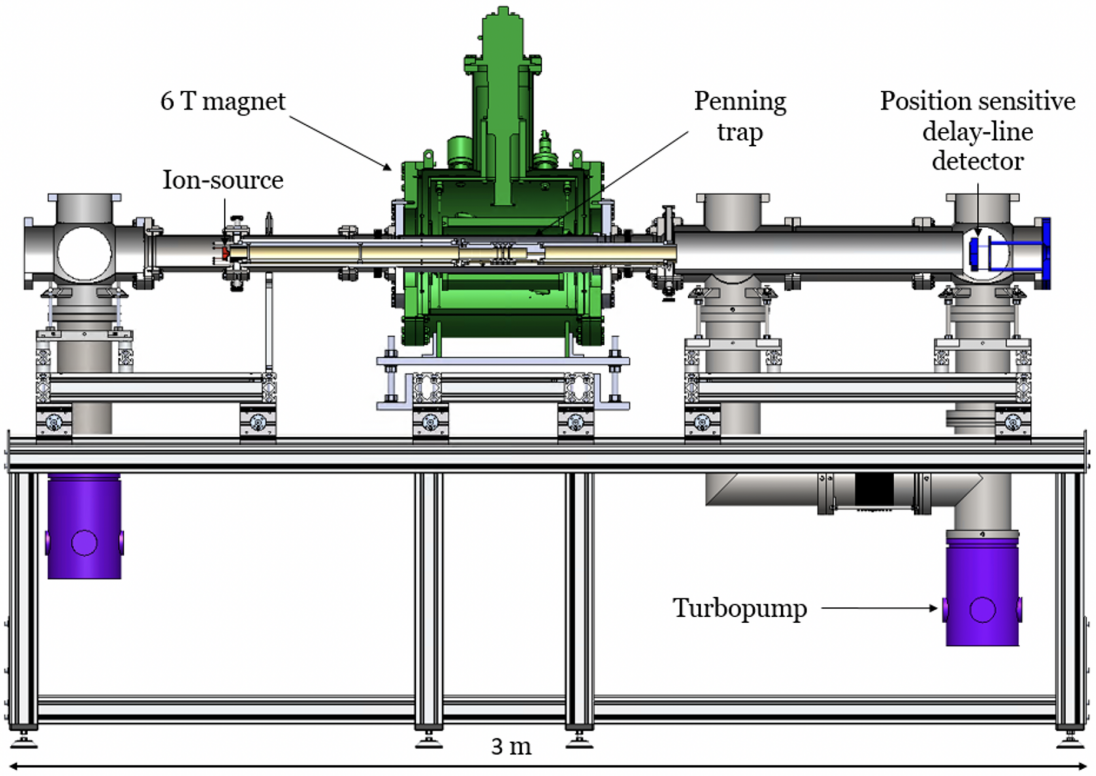

Figure 4.1: *Beamline construction of PILOT-Trap*
Shown is the beamline of the PILOT-Trap mass spectrometer with its technical components. Thereby the 6 T coldhead cryo-cooled magnet (green colored, see also figure 4.2) is placed in the middle.
Centered in the own designed warm bore of the magnet, the trap assembly (see also figure 4.5) is located. The rubidium ion source is placed on the left (red colored)
Right after the trap assembly follows a perforated (to enhance the pumping cross-section in the ion's ejection path region) drift tube, whose electric field accelerates ions towards the position sensitive detector (blue colored). The construction consists of a big horizontal support frame, on which three height adjustable movable tables are placed, carrying the three independent segments of the beamline (namely the ion production and transport setup, the magnet and the trap assembly), connected by bellows towards the magnet. This construction ensures the maximal degrees of freedom for the alignment.

degrees of freedom are preserved to align the beamline.

Attaching an additional small frame to the support frame makes it possible to move one of the outer segments further away from the magnet to remove the inner structure. This small frame is movable to both ends of the beamline (not shown in figure 4.1) and was chosen to reduce the size of the beamline. Using movable

segments makes the setup flexible and transportable, since every segment could be fixed to a small frame and the support frame can than be dismantled, to ensure fitting in a small transporter and easy movement in buildings. Without any loss of alignment it could then be built up at another facility by just ensuring that the support frame is aligned horizontally to the beamline of the external ion source.

4.2 Built-in components

This chapter shows all devices with their technical properties and design parameters used to realize the PI-ICR measurement technique, which might influence the possibilities and precision of the measurement result.

Like the ion's path in the duty cycle, the chapter starts with the description of the ion source, followed by the magnet, which is classified as the most important and crucial component. Afterwards the installed Penning trap with its geometry is presented. As the last beamline part the delay-line detector is introduced with its spatial and time resolution and the explanation of its working principle. In addition the position readout process is described. Afterwards, the additionally used electronic devices are presented shortly, but more details can be found in the appendix section A. Finally the control system is presented, which provides communication with all devices. In addition security installations are shown to protect the experiment with its devices from potential damage that might be caused by a power shortcut.

4.2.1 Ion source

In this setup, a rubidium ion source from *HeatWave Labs, Inc., (101142 emitter)* [34] is used. It is based on surface ionization, where for cation production a high temperature ionisator with high work function ϕ_s (here rhenium) is used to ionize an alkali (here rubidium) with ionization potential ϕ_i. If an evaporated atom is in contact with the heated rhenium surface for sufficiently long time, it comes in a thermal equilibrium with the rhenium atoms and the ionization probability is described by the Langmuir-Saha [35] equation:

$$P_i = \frac{n_i}{n_i + n_0} = \left(1 + \frac{g_0}{g_i} \exp\left[\frac{e(\phi_i - \phi_s)}{k_B T}\right]\right)^{-1}. \tag{4.1}$$

Here n_i and n_0 indicate the number of ions and atoms, respectively, and g_i and g_0 describe the degeneracy of the state, respectively, where for alkalis $g_i/g_0 = 1/2$. The elementary electric charge is represented by e and the Boltzmann constant with k_B. Since the ionization efficiency drops with an increase of temperature T, the temperature has to be set just high enough to evaporate the atoms of interest.

4.2.2 Magnet

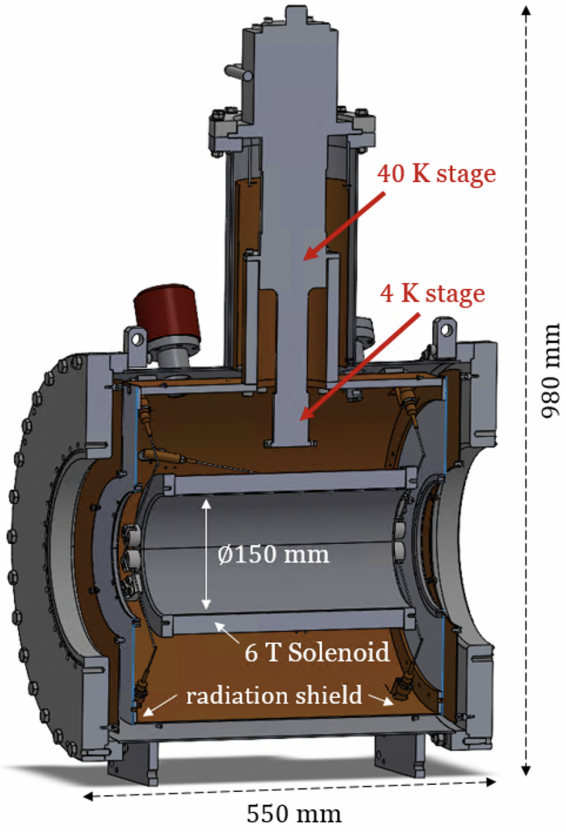

Figure 4.2: *Construction of the magnet* The cryogenically cooled superconducting 6 T magnet is cooled by a two stage coldhead to enable coil temperatures of about 4 K. The coil is shielded from radiative heat by a radiation shield, reaching from the flanges left and right toward the cold head turret, where it is connected to the first stage to get cooled down to $\approx 30 - 40$ K. The displayed connection possibilities on the radiation shield or even the coil holder may be used to realize a cryogenic Penning trap (see chapter 7.4). No need of liquid helium and the compactness make this magnet perfectly suitable for transport.

The cryogenically cooled superconducting 6 T magnet from *CRYOGENIGC LTD* is equipped with a coldhead, which consists of a two-stage cryocooler to hold the magnet coil at a temperature of around 4 K. Being cooled by a coldhead and not by liquid helium makes this magnet suitable for transport. The construction of the magnet together with its geometric parameters are displayed in figure 4.2.

To protect the magnet from radiation heat, it is equipped with a radiation shield, reaching from the flanges left and right toward the cold head turret, where it is connected to the first stage to get cooled down to $\approx 30 - 40$ K. This stage has a cooling power of roughly 40 W to support the 4 K stage, which provides a cooling power of 1 W and is directly connected to the coil. The radiation shield was extended through the inner of the coil, so that the coil is protected from radiation heat of the installed warm bore, which is adapted to the CF250 flanges of the magnet. The helium used in the helium lines of the *Sumitomo 415* cold head [36] is cooled by the compressor *Sumitomo CSW-71D* [37], that on the other hand is cooled by cooling water.

In addition, the magnet contains carbon ceramic temperature sensors connected to important components, providing low magneto-resistance. These wires of the thermometers are fed through a 25-pin UHV connector towards the *Keithley 2700*

temperatures:	manufacture specs	@ PILOT-Trap [1]
first stage	31.4 K	43.3 K
radiation shield	32.4 K	45.3 K
second stage	2.9 K	3.55 K
magnet winding	3 K	4.08 K
persistent switch	4 K	5.28 K

magnet:	
cool down time	$\leq 1\,\mathrm{day}$
field constant	$51\,\mathrm{mT/A}$
homogeneity [2] (determined by manufacture data)	$2 \cdot 10^{-5}$
homogeneity [3] (determined by Kellerbauer group) [39]	10^{-4}
homogeneity [4] (determined by magnetic field measurement)	$3 \cdot 10^{-5}$
time stability in persistent mode [39]	$2 \cdot 10^{-5}\,\mathrm{h}^{-1}$

Table 4.1: *Specification of the superconducting magnet*

Multimeter [38], where the resistance is measured and are traced back to the temperature value. Typical temperature values of the specific components are given in table 4.2.2.

Magnetic field

One of the most important parameters of the magnet for PILOT-Trap is a high magnetic field homogeneity in the center of the magnet. Unfortunately, the manufacturer gives the specs with a current load of just one ampere on the coil, shown in figure 4.3 b). Without detailed information on the measurement procedure (for example the diameter of probe), it is hard to determine the homogeneity, but it could be estimated to $2 \cdot 10^{-5}$ at a distance of 2 mm from the center on the symmetry axis.

The magnet was previously used in the group lead by A. Kellerbauer, where the homogeneity was determined to be 10^{-4} [39] . Nevertheless, in the experiments by the Kellerbauer group this magnet was only used to trap ions, not to perform precision Penning-trap measurements. That's why one part of this work is to find out, if the generated magnetic field is homogeneous enough to perform PI-ICR measurements, or if it could just be used to build a cooling trap with the buffer-gas technique. For that reason, a magnetic field measurement with a nuclear-magnetic-resonance (NMR) probe was carried out. For this a flange with a gateway out of plastic was designed and built, which was connected to the magnet on one side and a

[1] measured with installed warm bore and radiation shield

[2] calculated from manufacture data, where they measured the magnetic field strength in the center at 1 A in steps of 2 mm, but do not give information about the measurement sphere

[3] in 20 mm sphere volume

[4] own measurement over the marked center area (see figure 4.3 d))

manual linear manipulator on the other side. The end of the linear manipulator was equipped with a holding aluminum tube for the NMR-probe. With this construction it is possible to move the NMR-probe in the warm bore along the symmetry axis of the magnet, so that the magnetic field strength could be measured at different positions. The results of these measurements are displayed in figure 4.3. The measurement yielded a better homogeneity in the center than the manufacturer states. But this area of homogeneity is located 4 mm off the geometry center of the magnet. In addition it could be seen, that the magnetic field varies for every new charging of the coil. From the comparative measurement displayed in figure 4.3 a), a magnetic field strength difference of 0.4 mT can be derived in the center of the magnet between two charging times. This was expected but verifies that the magnetic field strength has to be determined after every charging, as well as the radial eigenfrequencies of ions in the Penning trap.

Furthermore the polynomial coefficients B_m (extracted from a polynomial fit to the manufacture data) are fitted with a scaling amplitude I (analogue to supplied current in coil) to the measured data, once with a possible offset c (see graph a)) and once without (see graph c)). Since there is no physical reason for an offset c and the manufacturer data should just scale in amplitude dependent on the current, a variance between the manufacturer and measured data is observed, which could be justified by the installed warm bore and radiation shield.

For closer investigation the center is displayed in figure 4.3 d), to which data a quadratic and a fifth-order polynomial fit was performed to determine the magnetic field coefficients in the trap region. In this plot, the red dotted line progression indicates the position sequence carried out at the measurement. Especially at the turn around points, different measured magnetic field strengths may demonstrate different displacements of the manipulator for the same set position. Furthermore, small imperfections like a slightly non-parallel mounting of the linear manipulator to the magnet flange or enhanced sag of NMR probe by further extending of the linear manipulator would lead to an offset from the symmetry axis. Nevertheless the extracted magnetic field coefficients listed in table 4.2.2 can be treated as a good assumption or even as an upper limit and can therefore be used to verify the suitability of the magnet for this project. As can be seen, all fitted magnetic field coefficients B_2 are in the order of a few $\mu\mathrm{T}/\mathrm{mm}^2$. In addition the magnetic homogeneity over this center area results to $3 \cdot 10^{-5}$.

For comparison, the magnetic field coefficients of the precision mass spectrometer ISOLTRAP located at CERN are used, which can achieve relative mass precision on the order of 10^{-9} [12] with a magnetic field strength of $B_0(\mathrm{ISOLTRAP}) = 5.93\,\mathrm{T}$. This experiment suits for a good comparison, since it also employs the PI-ICR technique and therewith makes use of comparable excitation radii. The spatial magnetic field strength distribution extracted from [40] calculates to $B_2(\mathrm{ISOLTRAP}) = -1.6 \cdot 10^{-7}\,\mathrm{T}/\mathrm{mm}^2$ without the use of shimming coils and $B_{2,shim}(\mathrm{ISOLTRAP}) = -1.4 \cdot 10^{-8}\,\mathrm{T}/\mathrm{mm}^2$ after shimming the magnet.

Since the relative mass precision $R_{\omega_c}$is directly proportional to the magnetic field imperfection R_B [41] as

$$R_{\omega_c} \coloneqq \frac{\Delta\omega_c}{\omega_c} \propto R_B \coloneqq \frac{B_2}{B_0}\,, \tag{4.2}$$

the achievable relative mass precision of PILOT-Trap can be estimated by assuming the same excitation radii. A comparison of B_2(ISOLTRAP) to the measured data fit coefficient $B_{2,q} \approx 7\,\mu\mathrm{T/mm}^2$ with

$$R_{\omega_c}(\text{PILOT-Trap}) = R_{\omega_c}(\text{PILOT-Trap}) \cdot \frac{R_B(\text{PILOT-Trap})}{R_B(\text{ISOLTRAP})} \tag{4.3}$$

would lead to a relative precision of $1.8 \cdot 10^{-8}$ of PILOT-Trap, whereas the comparison with the manufacture data fit coefficient $B_{2,m} \approx 0.3\,\mu\mathrm{T/mm}^2$ would lead to $1.8 \cdot 10^{-9}$. With this, the goal of PILOT-Trap stated in the introduction would be realized, since a precision between both estimates can be expected. But this assumption takes into account an implementation of shimming coils being just as good as at ISOLTRAP. Without latter the currently achievable precision of PILOT-Trap is probably between $2 \cdot 10^{-7}$ and $2 \cdot 10^{-8}$, performing the same comparison with $B_{2,shim}$(ISOLTRAP), respectively. This precision is lower than the aimed one, but it could be improved besides with shimming coils by performing cryogenic buffer-gas cooling, which is described in chapter 7.4.

Vibration

Since the magnet is cooled by a coldhead, vibrations of the cooling process are transferred to the magnet housing, which could be felt by touching by hand. A measurement of the vibrations by attaching a piezo element to the surface of the magnet was carried out to determine the frequency of the vibrations. For this, the produced voltage in the piezo element was read out by an oscilloscope and is shown in figure 4.4.

Since the Piezo elements are attached directly to the surface of the magnet, it could only detect strong vibrations. The voltage magnitude does not reflect the full amplitude of vibration, since the Piezo module moves together with the magnet surface. However the frequency of the opening and closing of the coldhead could be determined to 2 Hz. With triggering on the vibration the goal is to pull down the measurement duty cycle of PILOT-Trap below 500 ms to ensure that the Penning trap is not moving against the magnetic field, even if it is not proven that this vibration is transferred to the magnetic field or the Penning trap. It is assumed that fast vibrations of small amplitude cancel out during the ion motion in the trap and the coil is not moving because the vibrations get damped by its bigger mass and its flexible attachment to the magnet surrounding. But it may be possible that the vibration may be transferred along the beamline to the Penning trap holding flange, which then may effect the position of the Penning trap relative to the magnetic

Manufacture polynomial fit @ 1 A	
$B_{0,m}$	$0.051\,\mathrm{T}$
$B_{1,m}$	$-2.0 \cdot 10^{-12}\,\mathrm{T/mm}$
$B_{2,m}$	$-2.8 \cdot 10^{-7}\,\mathrm{T/mm^2}$
$B_{3,m}$	$8.3 \cdot 10^{-13}\,\mathrm{T/mm^3}$
$B_{4,m}$	$-3.8 \cdot 10^{-11}\,\mathrm{T/mm^4}$
$B_{5,m}$	$-8.5 \cdot 10^{-15}\,\mathrm{T/mm^5}$

$B_{fit,off,m}$ after Rampdown	
I	85.7 ± 1.0
z_{off}	$0.70 \pm 0.03\,\mathrm{mm}$
c	$1.68 \pm 0.05\,\mathrm{T}$

$B_{fit,off,m}$ before Rampdown	
I	116.8 ± 2.4
z_{off}	$0.83 \pm 0.09\,\mathrm{mm}$
c	$88.7 \pm 1.2\,\mathrm{mT}$

$B_{fit,m}$ before Rampdown	
I	118.6007 ± 0.0007
z_{off}	$0.50 \pm 0.09\,\mathrm{mm}$

Central polynomial fit	
$B_{0,p}$	$6.064913 \pm 7 \cdot 10^{-6}\,\mathrm{T}$
$B_{1,p}$	$(-2.7 \pm 0.8) \cdot 10^{-5}\,\mathrm{T/mm}$
$B_{2,p}$	$(3 \pm 6) \cdot 10^{-6}\,\mathrm{T/mm^2}$
$B_{3,p}$	$(7.8 \pm 2.3) \cdot 10^{-6}\,\mathrm{T/mm^3}$
$B_{4,p}$	$(-1.8 \pm 0.9) \cdot 10^{-6}\,\mathrm{T/mm^4}$
$B_{5,p}$	$(-8 \pm 24) \cdot 10^{-8}\,\mathrm{T/mm^5}$

Central quadratic fit	
$B_{0,q}$	$6.064920 \pm 8 \cdot 10^{-6}\,\mathrm{T}$
$B_{1,q}$	$(8 \pm 4) \cdot 10^{-6}\,\mathrm{T/mm}$
$B_{2,q}$	$(-7.1 \pm 1.7) \cdot 10^{-6}\,\mathrm{T/mm^2}$

Table 4.2: *Fitted magnetic field coefficients on measured data (see figure 4.3)*

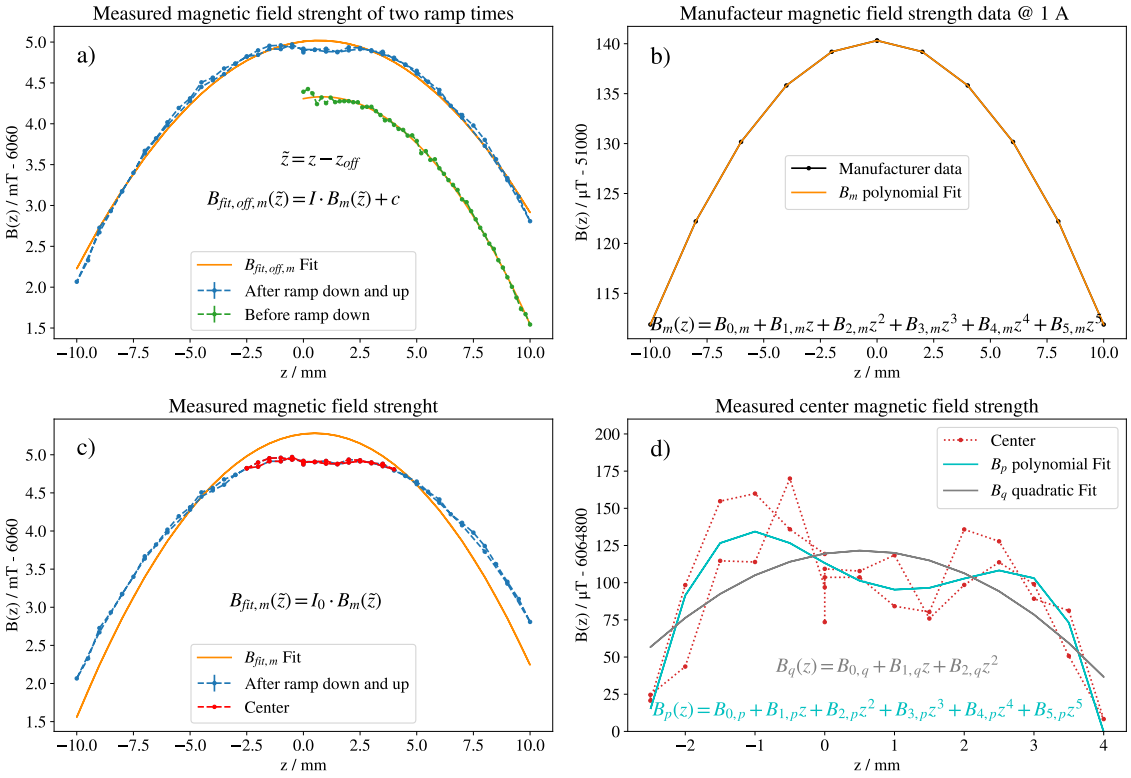

Figure 4.3: *Magnetic field strength measurement with a NMR-probe*
(a) displays magnetic field measurements with a NMR-probe for two different ramp times of the magnet. As can be seen, the magnetic field strengths varies for every ramping, due to current variation in the coil. In addition the polynomial coefficients B_m extracted from the manufacturer data (b) are fitted to these graphs with the current I as scaling factor and an offset parameter c.
In figure (c) the manufacturer polynomial B_m was fitted without constant offset, since there is no physical explanation for a constant offset and the magnetic field should just scale with the current running through the coils. In addition the center spot of the measurement is marked red, which is closer investigated in (d).
In latter, the measured central magnetic field is shown, on which a quadratic B_q and polynomial B_p fit was performed to estimate the polynomial magnetic coefficients (see table 4.2.2). The movement scheme of the NMR probe can be followed by the red dotted line.

field. However, the effect of vibration on the phase-sensitive measurement has to be investigated in more detail, which is carried out in section 5.4.1.

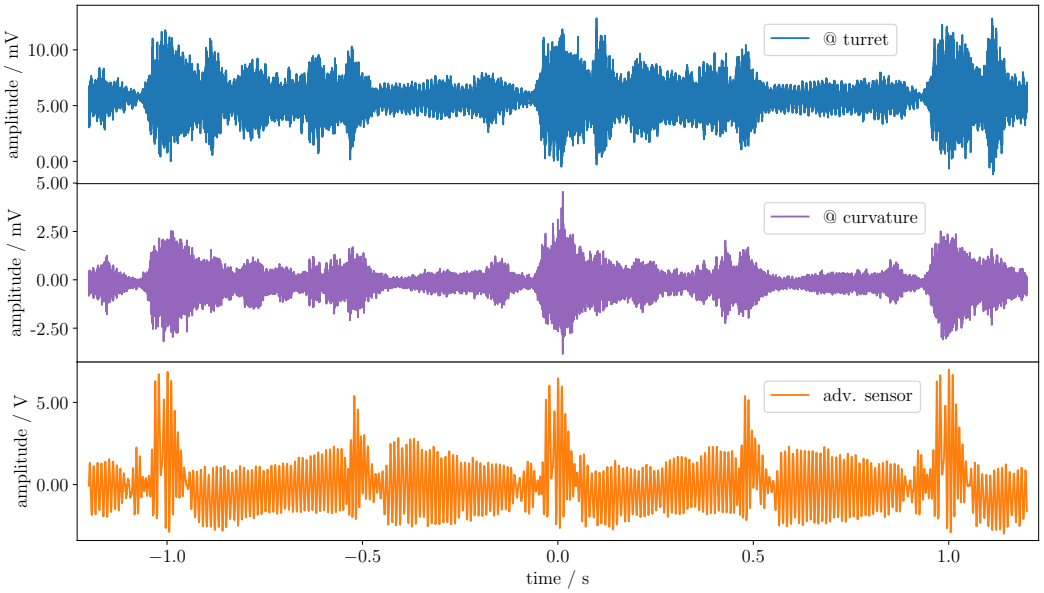

Figure 4.4: *Piezo detected vibration of the magnet*
The first two graphs show the detected voltage signals of a piezo element attached directly to the surface of the magnet housing at the labeled positions. The opening of the coldhead (at $t = 0$) can clearly be detected every second by the high increase of amplitude, wheres it is hard to detect the exact timing of the closing. In addition the vibrations between opening and closing seem to be stronger than between opening and closing. To investigate this closer a piezoelectric bender was mounted on the feedthrough of the magnet (red colored in figure 4.2). At the end of the bender weights are mounted, to enhance the deflection of the piezo by vibration. The amplified signal is displayed in the lower graph, where the frequency of opening and closing is determined to be 2 Hz. Latter piezo signal is used to generate the trigger signal for the measurement duty cycle with a Schmitt-Trigger circuit, described in section 5.4.1.

To emphasize once more, the magnet is classified to be the most critical component in the construction of PILOT-Trap. Even if it is perfectly suited for transport, it has to be investigated in this work, if it is suitable to function as a precision measurement magnet and the expected disadvantages of lower homogeneity and vibration, which both imply systematic effects on the measurement, could be concurred.

Parameter	value
distance between all electrodes	1 mm
length ring electrode (RE)	4.7 mm
length correction electrodes (CE 1&2)	12.6 mm
length end cap electrodes (EC 1&2)	50 mm
length diaphragm	50 mm
radius diaphragm	2 mm
radius electrodes	16 mm
tuning ratio TR	0.88
C_2	$1.46 \cdot 10^{-3}\,\mathrm{mm}^{-2}$

Table 4.3: *Penning-trap parameters*

4.2.3 Penning Trap and Ion Optical Elements

The inner working of the beamline, containing the Penning trap and surrounding drift electrodes is displayed in figure 4.5. Towards the detector the Penning trap is equipped with a pumping barrier of radius 2 mm to reduce the base pressure in the right beamline volume to prevent collisions of rest gas with the ion on its ejection path. In contrast, the first endcap has the opening radius as the inner trap radius of 16 mm to ensure a rather simple ion injection. Helium is injected into the trap via a small hole in the first endcap connected with a Swagelock-tube towards the feedthrough flange. The ring electrode is fourfold segmented to enable quadrupole rf couplings. With the listed geometry parameters in table 4.2.3 forming an orthogonal trap, the tuning ratio TR is determined to be 0.88 to form a harmonic trap. With this, the higher order correction terms of the potential (see eq. (2.16)) vanish, only leaving $C_2 = 1.46 \cdot 10^{-3}\,\mathrm{mm}^{-2}$.

The inner radius of the surrounding drift tubes DT0-DT3 is 21 mm. In addition, DT0 is fourfold segmented to focus the ion beam towards the Penning trap, which is also used to create ion bunches by pulsing the electrodes for a certain time. The Penning trap as well as the drift tubes are gold coated to avoid oxidation and surface inhomogeneities. In contrast, DT4 is made out of aluminum and is perforated to enhance the pumping cross-section in the right beamline setup. It has an inner radius of 60 mm and is provided with a fine grid at the end towards the detector to establish a linear potential increase over the small distance of 2 cm to the detector.

In figure 4.5 at each end of electrode the multiplication factor G_B is depicted, describing the magnification of spot radius relative to the trapped spot size, which is caused by the magnetic field gradient (see eq. (3.17)). One may counteract this magnification by lowering the potentials of the respective electrodes, so that the ions move faster and thus the magnetic field has weaker deflecting action on the ion's flight path.

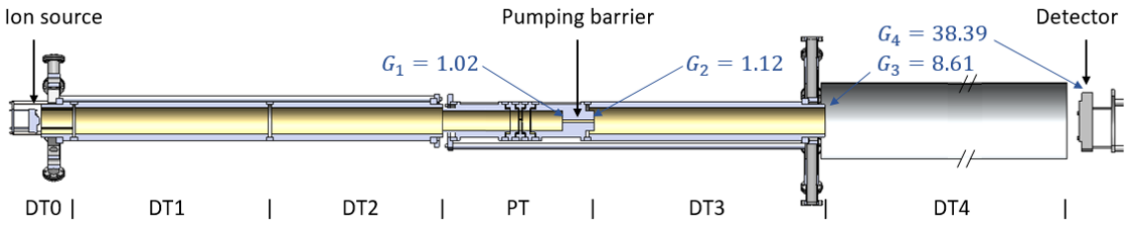

Figure 4.5: *The inner structure of PILOT-Trap*
The heart of the inner working builds the Penning trap (PT), which is equipped with a small channel (pumping barrier) towards the detector in order to reduce the base pressure in the ion's ejection path region. For an enhanced pumping cross-section in the same region, the drift tube DT4 (here shorter displayed) is perforated. The drift tube DT0 is quarter splitted to function as a focus or deflection element directly at the ion source to create ion bunches. In addition, the multiplication factors G (see eq. (3.17)) are displayed at each end of electrode to estimate the spot size magnification caused by the magnetic field gradient.

4.2.4 Delay-Line Detector and Position Readout

The *RoentDek DLD40* (Delay-Line Detector) [32], consisting of a mico-channel plate (MCP) and a delay-line anode, can be used for single particle or photon detection, giving high-precision information on the position and time of the impact.

An MCP consists of many very thin (here with pore size of 25 μm and center-center distance of 32 μm) lead glass channels, all parallel aligned in a typical 8 ° angle to the front surface. Between the front and end plate a voltage difference of typically 1 kV is applied. If an ion hits the wall of a thin channel, secondary electrons are emitted and accelerated to the end surface, whereby more collisions with the wall produce more electrons. Generally, two MCPs are assembled in series with contrary tilt of the channels to ensure that all particles hit the wall of one channel and a strong current signal is produced. After the MCPs follows the position sensitive delay-line anode, consisting out of two serpentine like ordered wires along the x- and y- direction with very small spacing. If the secondary electrons of an MCP-channel hit the anode, a current is induced, which flows in both directions of the wire. The time difference of this current signal at the end of the wires gives information about the particles hit position for the x and y coordinate, respectively. This working principle of the delay-line detector is displayed in figure 4.6.

The built-in *RoentDek DLD40* has an active area of 45 mm and could be used at a pressure below $2 \cdot 10^{-6}$ mbar. Together with a temporal resolution of < 0.2 ns and a position resolution < 0.1 mm it offers an absolute detection efficiency up to 81 % [42]. With the multi-hit dead time of $10 - 20$ ns it offers a rate capability above 1 MHz.

In this setup the delay-line signals are first inverted and amplified by a fast amplifier *FTA 820* from *ORTEC* [43] and then fed to a constant-fraction discriminator

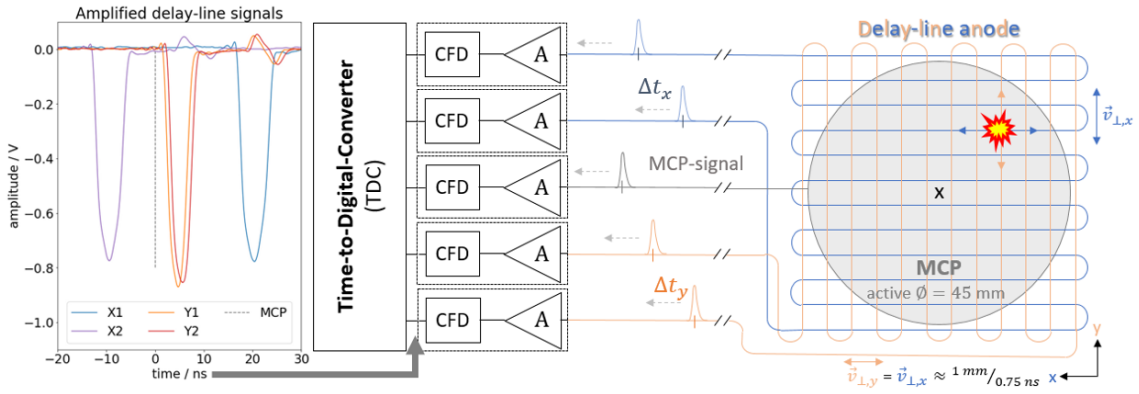

Figure 4.6: *Working principle of the delay-line detector*
The schematic composition of a delay-line detector is shown, consisting of an MCP and a delay-line anode. To calculate back the exact position from the observed time difference between both delay-line signals, the orthogonal spread velocity $v_\perp$ [32] can be used. The amplified brought delay-line signals with changing amplitude are reduced to exact time marks with a constant-fraction discriminator (CFD). Finally these time mark signals are digitized with a time-to-digital converter (TDC).

(CFD) *935 Quad CFD* from *ORTEC* [44]. Latter generates exact time marks of the delay-line signals regardless of their amplitudes. Thereby for each channel a trigger level can be adjusted, which is used to regulate the noise counts per time interval to around five per second.

The generated delay-line time marks are digitized with the *HPTDC8-PCI* [45] time-to-digital converter (TDC) from *cronologic*. This TDC card offers eight Nuclear Instrumentation Module (NIM) (current based) logic inputs with 25 ns bin size. Besides a dead-time between multiple hits on one channel of < 5 ns it has no dead-time due to readout. If the trigger logic is enabled on one channel it offers a 419 μs time window, with half of the span ahead and after the incoming trigger signal. This mode is used in the experiment, where for the trigger the ejection pulse of the Penning trap is used. Relative to this one, the MCP signal is detected, which then displays the time of flight. It has to be stated that for the whole delay-line signal acquisition equally long connections for all channels are used, to exclude systematic delays.

The readout of the TDC card was programmed in python within this thesis work, whereby the output of time marks is adjusted to the input format of the PI-ICR data-analysis script of ISOLTRAP [46], at which the final position analysis is oriented. To allocate the different time marks ($\{X_1, X_2, Y_1, Y_2, MCP\}$) to a detected ion position, the following boundary conditions are set for $\tilde{T}, T \in \{X, Y\}$, $i \in \{1, 2\}$ and $\tilde{T}_i = T_i - MCP$ to:

- $MCP \in [ToF_{min}, ToF_{max}]$

- $\tilde{T}_i \in [-12\,\text{ns}, 25\,\text{ns}]$
- $\sum_i \tilde{X}_i \in [9\,\text{ns}, 15\,\text{ns}]$ and $\sum_i \tilde{Y}_i \in [10\,\text{ns}, 17\,\text{ns}]$
- $(\Delta\tilde{T} = \tilde{T}_1 - \tilde{T}_2) \in [-35\,\text{ns}, 35\,\text{ns}]$

The latest boundary symbolizes the maximal possible time difference of one coordinate, which follows from the active diameter of 45 mm and the perpendicular signal speed (pitch of one wire loop) $v_\perp = 1.33\,\text{mm/ns}$ (only accurate within 5%). The first condition is based on the time-of-flight distribution, dependent on accelerating electrode potentials and the ion mass. Lasting two conditions are determined experimentally (see in appendix figure A.1) and show, that separate coordinate time signals can even be detected before the MCP signal, but the mean of the two time signals of one coordinate is after the MCP signal. This mean time value indicates a perfect centered hit with respect to the coordinate on the detector.

The self-written time mark readout together with the adapted position analysis were verified with Monte-Carlo simulated data. The verification pointed out self-created hit points, when the ToF-distribuition is reduced and the ions per shots are increased. Thus coordinate time signals of separate ions can add up to self-created hits, when lying in each others boundaries. That is the reason why data of a complete shot is neglected in the analysis, when any time signal in the shot is used twice. This reduced the detection efficiency but is counteracted by tuning the ion bunch to obtain one detected ion per shot, which is also good to avoid ion-ion interaction in the Penning trap. The results of these simulations are shown in figure A.2 in the appendix.

4.2.5 Other used Devices

In the following other used devices are listed, for which more details or measurements can be found in the appendix section A.

- A high-precision, low-noise DC voltage source *HV500-16* from *stahl-electronics* [47] to set electrode and Penning-trap potentials
- A programmable transistor-transistor-logic (TTL) pulse generator *PulseBlaster PB12-100-4k* from *SpinCore Technologies, Inc.* [48] with a pulse resolution of 10 ns to set the trigger signals for all time dependent parameters of a duty cycle
- A fast high-voltage push-pull switch developed at PENTATRAP [49], switching high voltages up to 500 V for pulses with ≥ 20 ns width on a timescale on the order of 10 ns
- Waveform generators of the *33X00*-series from *Keysight* [50] to generate the coupling and excitation frequencies
- A high-precision high-voltage power supply *NHQ 204M* from *iseq* to supply the delay-line detector with high voltage

4.3 Safety Installations and the Control System

During the realization of this project, PILOT-Trap developed to a completely remotely controllable experiment with some safety features, which will be explained and shown in this section.

Since a warm bore was installed in the magnet, it was possible to separate the vacuum of the magnet from the beamline-vacuum. The magnet system is pumped via a small turbo pump *SL80* from *Leybold* [51], which is connected via a voltage controllable valve towards a scroll pump. With the help of a circuit connected to the scrollpump, this valve closes automatically, when the scroll pump shuts down or fails for some reason. This ensures the survival of the turbo pump and that the vacuum is kept inside the magnet. In between the magnet and the turbo pump a full range pressure gauge and an over-pressure valve are assembled. Latter is implemented for safety in case a lot of gas freezes out in the magnet and an over-pressure is built by warming up the magnet.

The magnet itself has its own safety circuit to ramp down the magnetic field fast and therewith prevent a quench. In case the power supply is shut down, the current of the coils is routed to dumping resistors, where the energy gets dissipated by heat, which is as well the case, if the compressor for cooling the cold-head is shut down. Latter is the case, when the cooling water of the compressor is too warm, so that it shuts down. Since in the beginning of the project a lot of "restoration work" in the laboratory was done, affecting the cooling water system, the water tubes got equipped with temperature sensors, whose data were logged. In case of a temperature rise, a warning mail is sent. This warning system was also used for all logged pressures of the beamline and the temperatures of magnet components.

Both turbo pumps of the beamline are connected over an automatic closed valve to another scroll pump, so that these two systems are really separated from each other and in case of a failure, the pressure holds to protect the MCP of the delay-line detector.

All vacuum pumps together with the power supply of the magnet are connected to an uninterruptible power supply (UPS), which is connected to the generator network. In case of a power failure at the institute, the generator should deliver power after about one minute. During this time interval the UPS should deliver enough energy to run the powersupply of the magnet and the pumps to ensure no quench of the magnet and holding the vacuum to protect the magnet and the delay-line detector.

All the logged data of pressures and temperatures are shown in the self-written PILOT-GUI. With this control system it is possible to set the timings of the trigger pulses of the TTL card to change the pattern of a duty cycle. In addition one can control the potentials of all electrodes, the current of the ion source (tuning the ions per shot), the high voltage of the delay-line detector and the frequencies for all excitations or couplings. Furthermore it allows setting different helium-flows, by controlling the fine dosing valve *EVR116* [52] controlled with the *RVC300* controller [53] from *PFEIFFER VACUUM*, whereby just flows up to 10^{-5} mbar l/s are allowed also for security reasons.

5 Proof-of-Principle Measurements with Rubidium

In this chapter, the first proof-of-principle tests for phase-sensitive measurements with the fully assembled setup, described in section 4.1, are presented. This section describes the first fundamental tests and achievements carried out to enable phase-sensitive measurements of the ions eigenfrequencies.

5.1 First Detected Time-of-Flight Signal

The first step of commissioning was to shoot a constant current ion beam through the setup to the delay-line detector without the presence of a magnetic field. With only radial-symmetric voltages on all drift tubes at -500 V signals could be detected on the MCP. Consequently, the thorough alignment with a telescope paid off, since the ions were able to fly through the small pumping barrier. By changing the voltage on one of the fourfold segmented drift tube directly after the ion source (DT0), the ion beam is deflected resulting in zero detector counts.

A similar test was performed with magnetic field. For this, the current in the magnet was ramped up in order to generate a magnetic field of 6 T in the center of the Penning trap. It was observed that the ion beam did not change so that ions were still detected, when all electrodes were supplied with $-500\,\mathrm{V}$.

In the next step, the setup was operated in pulsed mode compared to the continuous measurements described above. In pulsed mode, a voltage on the fourfold segmented electrode at the ion source was switched from GND (passing ions) to $-200\,\mathrm{V}$ (deflecting ions) to chop the beam. The used cycle had a pulse width of $3\,\mu\mathrm{s}$ that was repeated periodically every 10 ms . The measured timings of the MCP signal relative to the chopping trigger are plotted in figure 5.1, which is the first measured time-of-flight spectrum with PILOT-Trap. For comparison, the time of flight was calculated for the first two charge states of the stable rubidium isotopes Rb^{85} and Rb^{87} using the acceleration potential, flight distance, literature mass and charge state, which are added in figure 5.1. The alignment of the calculated and measured signals proves clearly, that the detected ions are singly and doubly charged rubidium ions. The ToF-peak of the singly charged rubidium isotopes appears a bit broad, so that it may include other contaminants, like for example molybdenum, out of which the ion source is built. Another possibility for the detection of four peaks in the time-of-flight area around the singly charged rubidium isotopes can be the switching of the deflection electrode. This electrode is switched from $-200\,\mathrm{V}$ to GND for a duration of $3\,\mu\mathrm{s}$. Therefore, further accumulation of rubidium isotopes

could be detected by the acceleration during the switching back. Moreover, the width of the ToF distribution coincides with the bunch width in time.

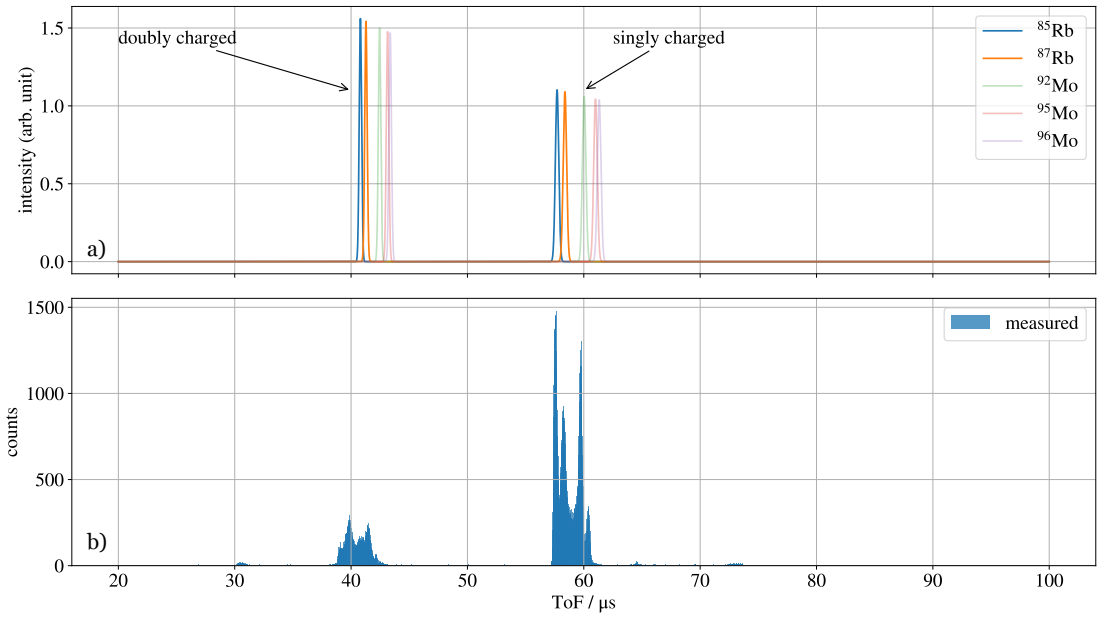

Figure 5.1: *First measured time-of-flight spectrum*
a) Calculated time of flights for different isotopes.
b) Measured time-of-flight spectrum.
This measurement verifies the detection of singly and doubly charged rubidium ions. Detecting four peaks at a ToF around 60 µs may be due to the detection of molybdenum ions, out of which the surface ionization source is built, or the accumulation of rubidium isotopes due to the acceleration during the chop-switching. The latter explanation is favored since the time between the last two peaks towards the first ones equals the chopping pulse width of 3 µs.

5.2 Trapping of Ions in the Penning Trap

Following the successful transmission of a continuous and chopped ion beam through the Penning trap and onto the position-sensitive detector, the setup was configured for trapping the rubidium ions in the Penning trap. Compared to the settings used in section 5.1, the trap electrodes were set to ground potential which decreases the ion energy in the trap region and increases the ToF.

Subsequently, the voltage on the first endcap *EC1* was set to a positive potential, so that no ions were detected anymore, ensuring no ion has higher potential energy compared to the trapping potential. This trapping potential on *EC1* was switched for the duration $t_{d,inlet}$ down to ground, where the starting time $t_{0,inlet}$ and duration was set in that way, that all ions of the bunch pass the first endcap without being accelerated, which could be ensured by the ToF remaining the same. The same procedure was executed for the potential on the second end cap EC2, where $t_{d,outlet}$ was set much larger to prevent ions to be accelerated.

Finally setting the ion source plate at 20 V and the trapping potential to 25 V together with $t_{d,inlet} = t_{d,outlet} = 30\ \mu$s starting at $t_{0,inlet} = 20\,\mu$s and $t_{d,outlet} = 150\,\mu$s realized the trapping of ions for different trapping times $t_{trap} = t_{0,outlet} - t_{0,inlet}$. The result for different trapping times is shown in figure 5.2.

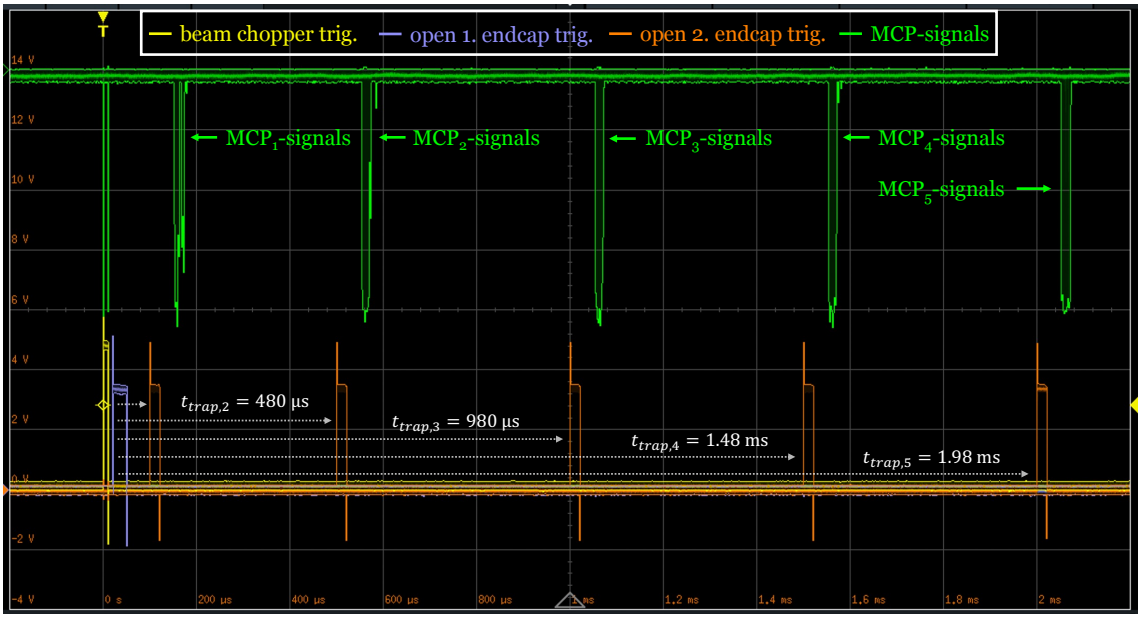

Figure 5.2: *First realization of trapped ions*
The trapping measurement recorded with an oscilloscope in the envelope mode is displayed. By varying the trapping time, new pulses of lowering the voltage on EC2 are additionally displayed with the following detected MCP signals. Here the trapping time is increased to almost two milliseconds, but it was tested up to one second with still detecting MCP signals.

5.3 Cooling and Separation of Rubidium Isotopes

After the trapping of ions was successfully implemented, the next step to realize is the buffer-gas cooling. In order to implement buffer-gas cooling, helium is injected into the Penning trap without applying any coupling or excitation frequencies of eigenmotions at first. With this, the ions are expected to interact by the collisions with the helium atoms. Thus, a shrinking of the amplitudes of the axial and modified cyclotron motion is expected, whereas the magnetron radius will increase (as described in chapter 3.1). Since the cooling time constant for the magnetron motion is much higher compared to one of the other modes, the ion beam should still pass the pumping barrier given a short enough trapping time. Since the axial motion gets cooled, a shrinking width of the time-of-flight peaks is expected, since their kinetic energy gets cooled to the temperature of the helium gas. Therefore, longer trapping times and higher helium pressure should lead to smaller width of the ToF-signals. In figure 5.3 the time-of-flight spectra for different trapping times are displayed for two different helium inlet fluxes of $5.2 \cdot 10^{-6}$ mbar l/s and $5.4 \cdot 10^{-6}$ mbar l/s in a) and b), respectively. The cooling effect by the presence of helium in the trap can clearly be seen: At the higher helium pressure, the width of the ToF signals after a trapping time of 50 ms is already reduced to its possible minimum of ≈ 1 ms, whereas for the lower pressure a more broad distribution is recorded.

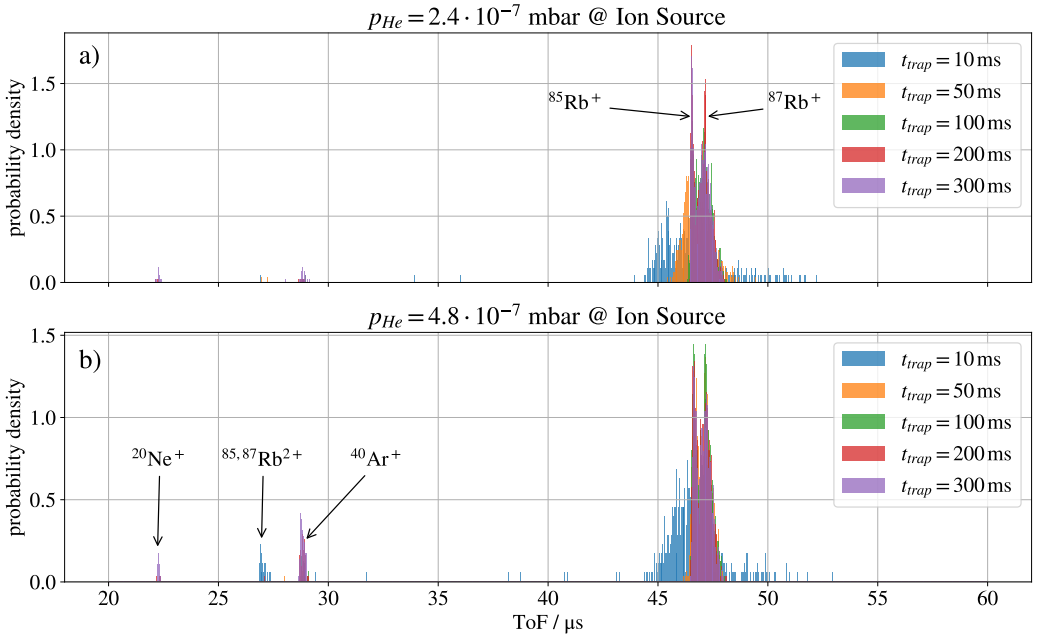

Figure 5.3: *Decreasing ToF-distribution width by increased cooling time with helium*
a) Detected ToF spectra at a helium inlet flux of $5.3 \cdot 10^{-6}$ mbar l/s.
b) Detected ToF spectra at a helium inlet flux of $5.4 \cdot 10^{-6}$ mbar l/s.

As can be seen in this plot, new time-of-flight peaks were appearing in these measurements, whose time compared to the rubidium peaks suggests to be argon and neon. It is assumed that a charge exchange takes place between the doubly charged rubidium ions and the noble gas in the trap. This is supported by the reduction of detected doubly charged rubidium ions for longer trapping times. In addition, the implemented fine-dosing valve was used beforehand with argon (and most likely also neon) explaining this observation. But these noble gases have to be ionized in the trap. Furthermore, the second ionization energy of rubidium is $\approx 27.29\,\text{eV}$, whereas the ionization energy of the noble gases are $\approx 15.76\,\text{eV}$,$21.56\,\text{eV}$ and $24.59\,\text{eV}$ for argon, neon and helium, respectively, making all ionization processes possible.

For the following measurements, the flux of the fine dosing valve was set to $5.4 \cdot 10^{-6}\,\text{mbar l/s}$. Even if the minimum width of the ToF distribution is already observed at a trapping time of 50 ms, a cooling time of $\approx 100\,\text{ms}$ is selected to ensure an optimal cooling.

As a next step, the buffer-gas cooling with the coupling of magnetron and modified cyclotron motion should be realized. For this, the magnetron motion of the ions is excited, so that no ions are detected in the time-of-flight spectrum anymore. This was realized by applying a frequency of 887.1 Hz for a duration of 10 cycles at one fourfold segment of the ring electrode to perform a dipole excitation (see chapter 2.1.1). After this, the quadrupolar excitation (see section 2.1.1) is applied on two opposite fourfold segments of the ring electrode. The frequency was scanned until the ions were cooled towards the center so that they pass the pumping barrier and induce an MCP signal again. With this, the coupling frequency was found, leading to the first determination of the free cyclotron frequency with the PILOT-Trap setup. Thereby the cyclotron frequencies of both rubidium isotopes were "manually" found to be $\omega_c(^{85}\text{Rb}) = 1.096590$ GHz and $\omega_c(^{87}\text{Rb}) = 1.071390$ GHz. Using equation (2.9), the modified cyclotron frequencies could also be calculated. With this, the separation of rubidium isotopes during the mass-selective buffer-gas cooling technique was realized as displayed in figure 5.4. The latter shows in a) the ToF measured with a trapping time of 100 ms at a helium inlet flow of $5.4 \cdot 10^{-6}\,\text{mbar l/s}$ without any excitations applied. Different ToF spectra with applying different excitation schemes are displayed in figure 5.4 b). The blue colored ToF spectrum is recorded by applying the determined magnetron frequency, which led to no detection of ToF-signals for both rubidium isotopes. But still the ToF peaks of the noble gases are recorded.

Starting together with the magnetron excitation, the coupling frequency $\omega_c(^{85}\text{Rb})$ or $\omega_c(^{87}\text{Rb})$ is applied, whose resulting ToFs are additionally displayed in figure 5.4 b), colored in orange and green, respectively. The reason for choosing this scheme is to perform noise-cleaning by exciting all isotopes to higher radii with the magentron excitation, while the wanted isotope is cooled towards the trap center again by coupling the magnetron mode with the cyclotron mode. To ensure cooling of the isotope of interest towards the center, the coupling amplitude is set much higher than the excitation amplitude.

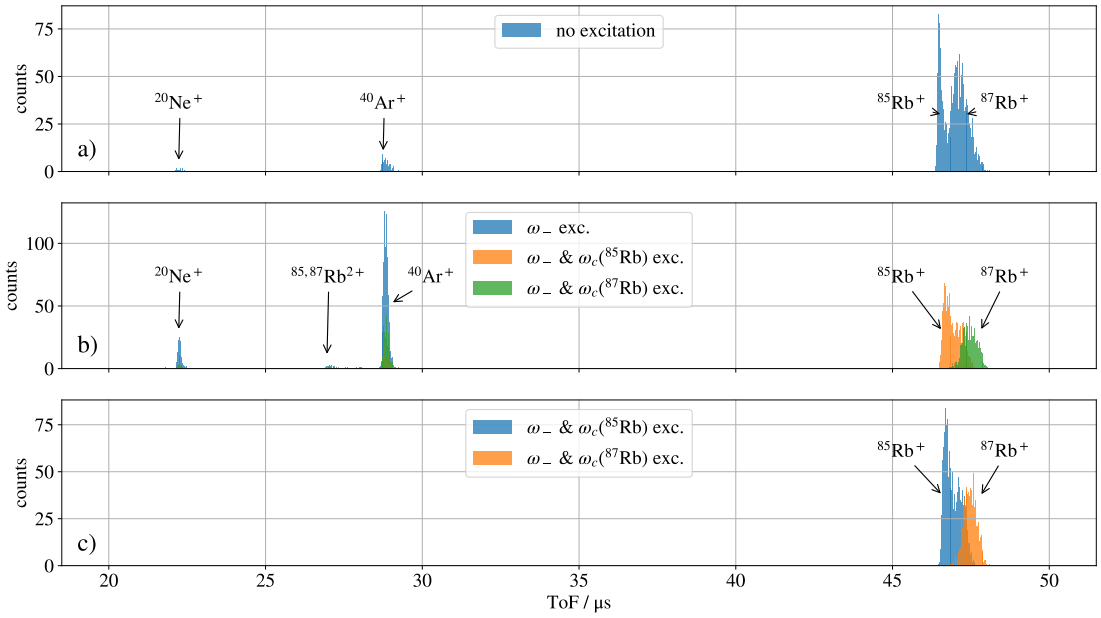

Figure 5.4: *Demonstration of mass-selective buffer-gas cooling*
a) pictures the ToF spectrum of the trapped ions without excitations. b) displays the time-of-flight spectrum for different excitations. Applying only the magnetron excitation leads to the disappearance of the singly charged rubidium signals, since they are excited to a larger radius compared to the one of the pumping barrier. The additional application of the cyclotron frequency for the respective isotope recenters the ion of interest. Thus, these ions can pass the pumping barrier and impinge on the MCP.
c) presents the successful mass-selective buffer-gas cooling, when the time-of-flight window used by the TDC card is set around the time range of the singly charged rubidium isotopes.

To shortly conclude this section, it was shown, that just the inlet of helium gas into the Penning trap cools the rubidium ions, reducing the axial energy distribution towards the temperature of the gas. The mass-selective buffer-gas cooling technique was successfully implemented by exciting the magnetron motion of all ions while coupling the magnetron and modified cyclotron motion by applying a quadrupole excitation at the free cyclotron frequency of the ion of interest.

5.4 Spot Optimization

In the previous sections, mainly the time of arrival of the ions on the MCP detector was recorded and this information used to draw conclusions on the operations that were done with the Penning trap. In the following, also the position information of the ions spatial projection on the delay-line detector behind the MCP is analyzed. For this, the readout of the TDC card was programmed in python within the framework of this thesis. The position readout was first adjusted with the dark count rate of the detector and afterwards optimized with the signals of rubidium ions. With this, the sensing of all coordinate signals per MCP signal was optimized together with measuring the times relative to the MCP signal to ensure the right boundary settings in the following data analysis. This readout calibration is described in the appendix A.0.1.

Ensuring the right coordinate data acquisition, the cooling spot and excitation spots could now be investigated. The first detector spots from analyzed position data are displayed in figure 5.5 using the previously described settings (section 5.2) and determined frequencies (section 5.3) for rf-excitations. Here, the blue spot presents the cooling spot with no further excitation. In addition, the magnetron excitations have been performed by applying an RF-signal with the previous determined magnetron frequency for five burst cycles after the cooling coupling pulse. This was carried out for different starting phases selected for the rf-excitation at the frequency generator. As can be seen in figure 5.5 a), distinguishable magnetron excitation spots were detected which show the set phase difference relative to each other. Other phase settings to detect a magnetron ring were not possible since the center spot is at the edge of the detector. Further increasing the starting phase shows no recorded ions on the MCP, confirming the spots are moving around the center spot for higher starting phases. In addition a modified cyclotron excitation was performed with the calculated frequency ω_+ according to equation (2.9). This resulted in a detected cyclotron ring displayed in figure 5.5 b), but its radius is small due to the damping caused by the buffer-gas.

These first detected ion spots are large, dominated by scattered ions and offset from the detector center. To correct for the offset and to allow better optimization the detector was moved in relation to radial the trap center. In addition, the spot structure for different magnetron excitation amplitudes in the noise cleaning as well as for higher helium pressures was investigated without achieving any noticeable improvement. Applying voltages analog to the calculated tuning ratio $TR = 0.88$ on the correction and end caps of the Penning trap resulted in the spot structure shown in figure 5.6 a). In this figure, the cooling spot and magnetron excited spots are displayed. For the latter, different starting phases at the frequency generator were chosen. As can be seen, still no round spots were observed. Nevertheless, the projections of the cooling spot and the magnetron excitation spots can be distinguished from each other. In addition, the set phase difference $\Delta\phi = \pi$ between the magnetron excitations is also recognizable in the projection of the excitation spots.

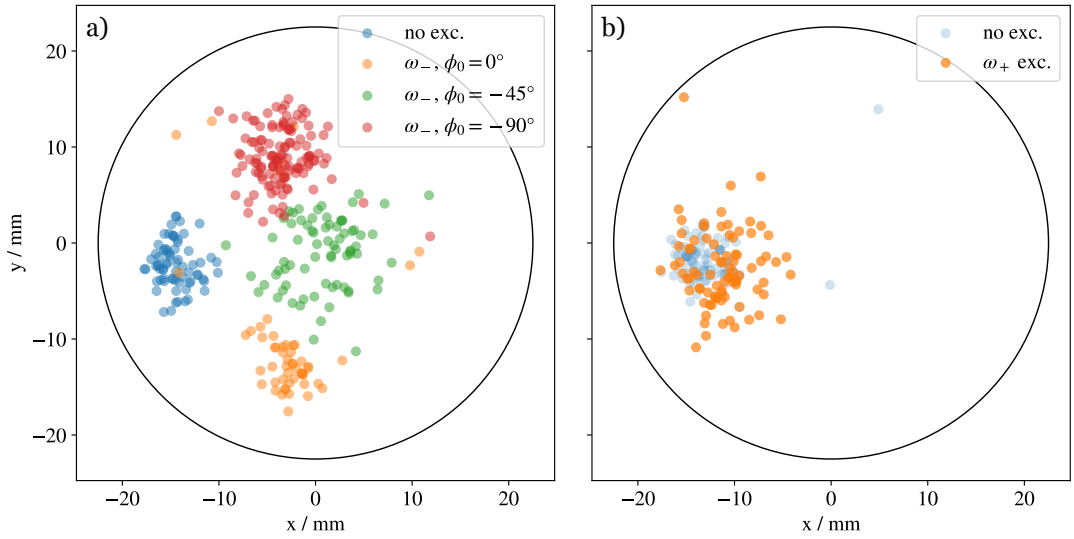

Figure 5.5: *First position-sensitive measurements on the delay-line detector*
a) Cooling spot (blue) and projections of excited magnetron motion for different phase offsets ϕ_0 set at the frequency generator.
b) Cooling spot (blue) and projections of excited modified cyclotron motion.

But some outliners are still observed during the optimization. To ensure that the correct frequencies are applied after the trapping potential was adjusted when changing the TR, frequency and amplitude scans were performed for the magnetron excitation and the cyclotron coupling, which are presented in the appendix C.

During the investigation of the influence of different drift potentials on the ejection path of the ions after the Penning trap, it became apparent that voltage differences between the drift electrodes DT3 and DT4 lead to a position shift of the cooling spot. This is shown in figure 5.6 b), where changing the voltage U_{ej} on the perforated drift electrode DT4 leads to a movement of the cooling spot. If the electrodes would be perfectly aligned on their respective symmetry axis, this should only lead to a (de-) focusing. However, if both voltages on DT3 and DT4 are increased so that the ion's potential energy is increased, the spot size increases, as the ions are slower and are thus stronger magnified by the magnetic field gradient. This showed that a further reduction of the potentials promises a reduction of the spot size, for which the focus must be adjusted again. Nevertheless, scattered ions are still observed during the described ejection voltage optimization. Therefore, the influence of vibration of the coldhead on the spot should be investigated first as a possible cause, since with a bigger projection of the spot these effects may be resolved more clearly. This is presented in more detail in the following chapters.

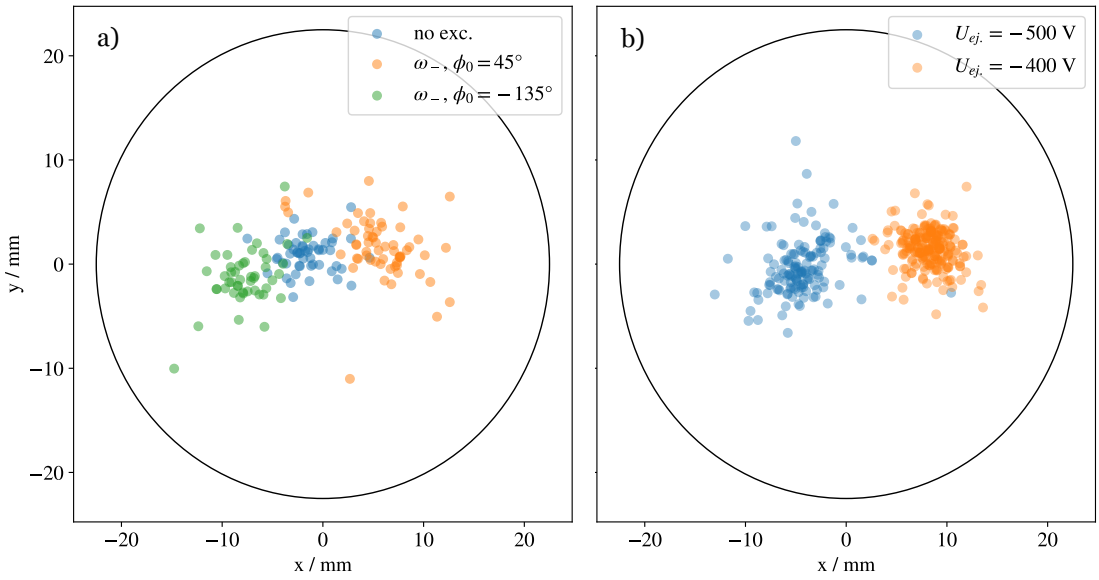

Figure 5.6: *Centered spot optimization*
a) Centered cooling spot (blue) and projections of the excited magnetron motion for different phase offsets ϕ_0 set at the frequency generator.
b) Detected sift of cooling spots for different voltage U_{ej} at DT4.

5.4.1 Investigation of Vibration Effects from the Coldhead

To investigate the influence of the coldhead's vibration on the spot structure, the measurement duty cycle was triggered by the vibration signal. For this purpose, the recorded signal of a weighted piezo bender was translated into a trigger signal with the help of a Schmitt-trigger circuit. In principle the alternating vibration signal is first cut to only positive voltage by a diode, followed by a low-pass filter. Here it is important that the signal is first cut by the diode, since otherwise the low-pass filter would average the signal to zero. With an adjustable threshold, it can be set from which level of the vibration signal a 5V trigger signal is output. This resulted in a trigger period of (499.87 ± 0.08) ms. With a measurement cycle length of ≈ 300 ms it was possible to shift the measurement in a time span of low vibrational amplitude. So far the measurements have been carried out directly one after the other with a fixed cycle length of ≈ 300 ms without any respect to the vibration. It is expected that the vibration will lead to a broadening of the spot when the measurement starts at different times compared to the vibration.

The cooling spot was first used to investigate the spot broadening. Here, the measurements were triggered once on the vibration, so that this is carried out in the low-vibration temporal range. These measurements are labeled with "Fixed Trig." in table 5.4.1. For comparison, measurements were carried out without the use of the vibration trigger, which are referred as "No Trig.". The time for all measurement cycles was set to an odd duration 363 ms, so that really always

Trigger	N_{ion}	c_x / mm	c_y / mm	r_x / mm	r_y / mm
No Trig.	3509	2.13 ± 0.02	-0.07 ± 0.03	1.32 ± 0.03	1.68 ± 0.03
Random Trig.	3427	2.17 ± 0.02	-0.08 ± 0.02	1.36 ± 0.02	1.69 ± 0.02
Fixed Trig.	3433	2.14 ± 0.01	-0.04 ± 0.02	1.33 ± 0.02	1.70 ± 0.02
No Trig.	10490	2.56 ± 0.01	-0.83 ± 0.01	1.19 ± 0.02	1.65 ± 0.02
Fixed Trig.	10660	2.59 ± 0.01	-0.82 ± 0.02	1.20 ± 0.02	1.60 ± 0.02
No Trig.	8770	2.60 ± 0.02	-0.89 ± 0.02	1.21 ± 0.02	1.66 ± 0.02
Fixed Trig.	8748	2.63 ± 0.02	-0.89 ± 0.02	1.18 ± 0.02	1.64 ± 0.03

Table 5.1: *Vibrations influence measurement on the basis of the cooling spot*
The determined values of the spot position (c_x, c_y) and radius $(r_x, r_y$ calculated from the FWHM) by fitting one dimensional Gaussian distributions to the cooling spots recorded with different trigger schemes are displayed.

Trigger	N_{ion}	c_x / mm	c_y / mm	r_x / mm	r_y / mm
No Trig.	24070	-7.79 ± 0.02	4.86 ± 0.02	1.40 ± 0.02	1.64 ± 0.02
Random Trig.	24004	-7.85 ± 0.02	4.72 ± 0.02	1.42 ± 0.02	1.62 ± 0.02
Fixed Trig.	24017	-7.82 ± 0.02	4.76 ± 0.02	1.40 ± 0.02	1.64 ± 0.02
No Trig.	24070	-7.74 ± 0.02	4.52 ± 0.02	1.45 ± 0.02	1.59 ± 0.02
Fixed Trig.	24017	-7.81 ± 0.02	4.44 ± 0.02	1.42 ± 0.02	1.57 ± 0.02

Table 5.2: *Vibrations influence measurement on the basis of an magnetron excitation spot*
The determined values of the spot position (c_x, c_y) and radius $(r_x, r_y$ calculated from the FWHM) by fitting one dimensional Gaussian distributions to excitation spots recorded with different trigger schemes are displayed.

different time intervals to the vibration for the measurement without trigger are realized. To ensure the latter, comparative measurements were performed with a randomly Gaussian-distributed delay to the vibration, which are labeled as "Random Trig.". All these measurements were performed alternately in order to cancel out the influence of the environment or drifts.

A comparison of the spot sizes is shown in figure 5.7. One dimensional Gaussian-distribution fits were carried out for the x and y dimension, respectively, to determine the spot position (c_x, c_y) and radius $(r_x, r_y$, calculated from the FWHM). The results of the measurements on basis of the cooling spot are listed in table 5.4.1. Furthermore, this investigation has been carried out with an excited magnetron spot as well, which results are listed in table 5.4.1. Based on these measurements, no significant increase in spot size can be detected.

Additional comparison measurements have been carried out with smaller spot sizes when lowering the potentials of the drift tubes at the ejection path of the ion. Still, no spot broadening was observed.

Nevertheless, the trigger on the vibration signal was and is still used in order to be able to perform the measurements in the detected low-vibration range. Besides the unused time towards the next vibration trigger, its use can only positively affect the measurement.

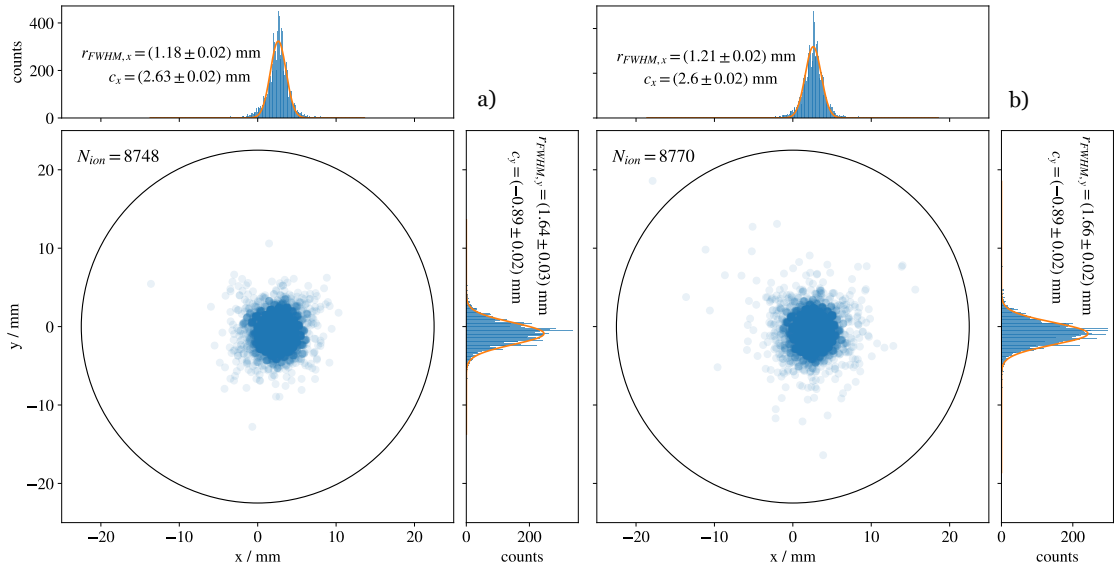

Figure 5.7: *Investigation of spot broadening due to vibration*
a) Detected spot using the trigger on vibration signal.
b) Detected spot without using the trigger on vibration signal.

5.4.2 Magnetron Excitation Spots

As we have been seen in section 5.4, lowering the potentials on the drift electrodes after the Penning trap realized a spot size reduction. For lower potentials, the ions are faster and therewith less influenced by the magnification of the magnetic field gradient. Optimizing the lens-effect for these reduced potentials led to the in figure 5.8 b) presented projections. Here a symmetric cooling spot with FWHM-radii of $r_x = (0.72 \pm 0.02)\,\mathrm{mm}$ and $r_y = (0.70 \pm 0.02)\,\mathrm{mm}$ is observed. The surrounding data points are magnetron excitation spots with a respective phase difference of 20°to the nearest neighbor spot forming a circular ring around the cooling spot. Here the different phases of the magnetron spots are not produced by different starting phases of the rf-excitation, but by different phase evolution times after the magnetron excitation. In addition, magnetron excitation spots with higher excitation amplitude are recorded for both potential settings and displayed in figure 5.8 c) and d), respectively. Comparing these, the lens-effect are more pronounced for the deeper potential settings, converting the circular ring consisting of magnetron excitation spot (b)) to an ellipse (d)).

The amplification of the focus has been carried out in order to enable a temperature measurement of the cooling spot to confirm that the cooling of the ions is optimized to maximal performance. Using a simple cross-multiplication calculation, the projected cooling spot size and the projected diameter of the pumping barrier should be used to infer the spot size in the Penning trap after the cooling process. In addition, the magnification G from the trap center towards the pumping barrier is negligible, as shown in figure 4.5. In this measurement, the magnetron excitation amplitude was increased further and further until no signals are observed anymore at the detector, because they are colliding with the pumping barrier. In figure 5.8 c), a slight truncation of the spots due to collisions with the pump barrier can already be seen at the top and right of the circle. Seeing the extinction of the spots by the pump barrier without being limited by the detector diameter was the actual reason for increasing focus. However, since an amplified lens-effect as well as a phase-shift (compare b) and d)) are noticeable at large excitation amplitudes, the radius of the barrier seems to be too large and a modification of the setup is needed to perform this type of temperature measurement.

Based on these observations, the potentials were reset to the settings analogous to a) and the detector was aligned in relation to radial the trap center. In figure 5.9 the projections of magnetron excitation spots with phase evolution times in steps of 142 µs up to one period of the magnetron motion of 1.14 ms are presented. The spots with one period of the magnetron motion as phase evolution time overlays perfectly the one without any phase evolution time.

With this, phase sensitive frequency measurements on the magnetron motion are now possible with the current setup of PILOT-Trap.

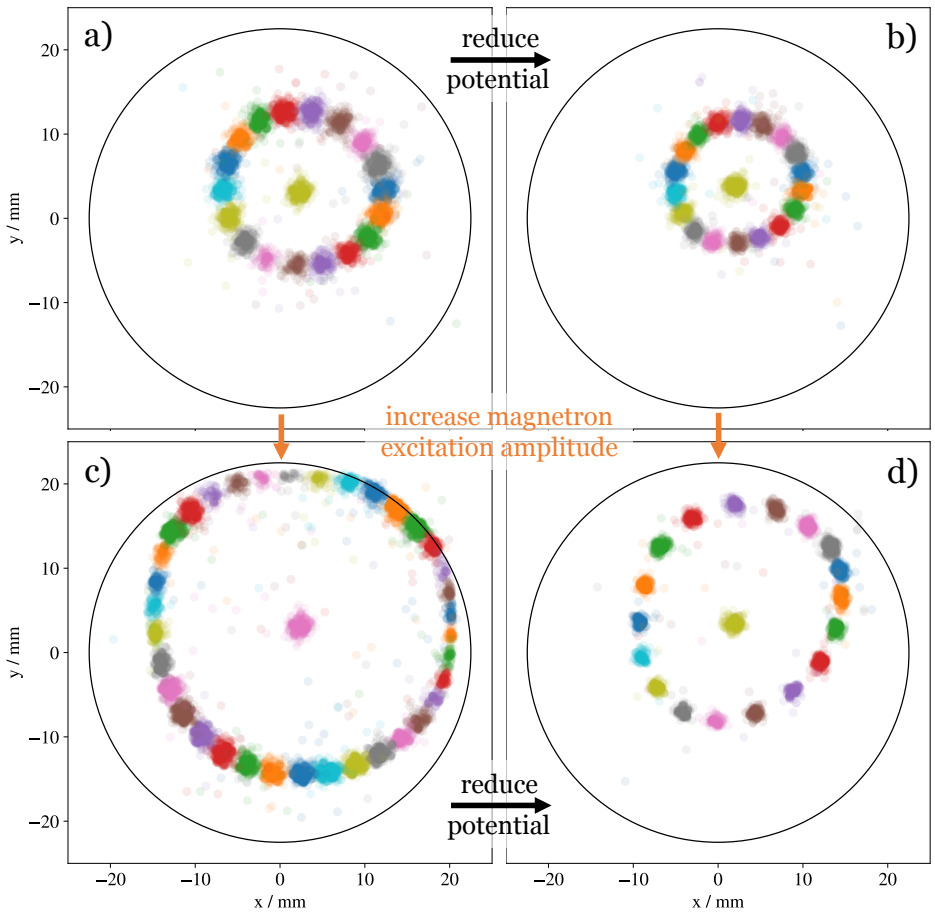

Figure 5.8: *Magnetron excitation spots at different excitation amplitude and drift electrode potentials*
a) $U_{DT3} = -404\,\mathrm{V}$, $U_{DT4} = -1\,\mathrm{kV}$ and excitation amplitude of $0.5\,\mathrm{V}$ with respective phase difference of $\pi/9$.
b) $U_{DT3} = -520\,\mathrm{V}$, $U_{DT4} = -1.6\,\mathrm{kV}$ and excitation amplitude of $1.03\,\mathrm{V}$ with respective phase difference of $\pi/9$.
c) $U_{DT3} = -404\,\mathrm{V}$, $U_{DT4} = -1\,\mathrm{kV}$ and excitation amplitude of $0.5\,\mathrm{V}$ with respective phase difference of $\pi/18$ to map the pumping barrier.
d) $U_{DT3} = -520\,\mathrm{V}$, $U_{DT4} = -1.6\,\mathrm{kV}$ and excitation amplitude of $1.03\,\mathrm{V}$ with respective phase difference of $\pi/9$.

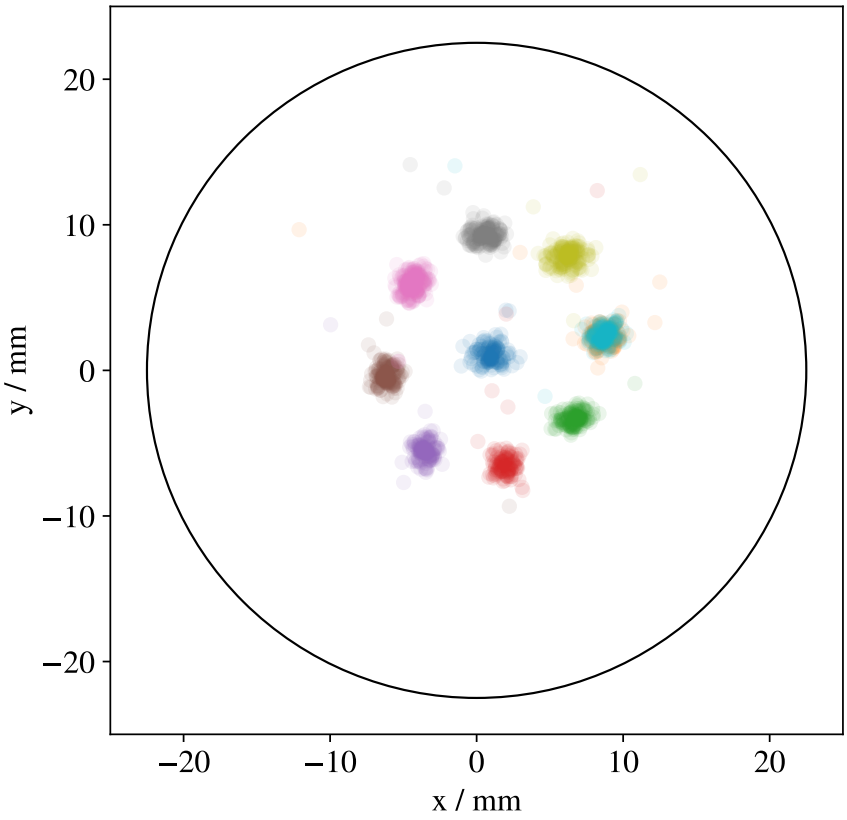

Figure 5.9: *Magnetron excitation spots at same excitation amplitude but different phase evolution times*
The cooling spot surrounded by circular ring consisting of magnetron excitation spots with respective phase difference of $\pi/4$ for centered ion projection is shown. In addition, the magnetron excitation spot with a phase evolution time of one period of magnetron motion (turquoise) overlaps the one without any phase evolution time (orange). This shows that phase-sensitive measurements of the magnetron frequency are possible with PILOT-Trap.

6 Dynamic Cooling

This chapter is devoted to the description of the development of the dynamic buffer-gas cooling technique carried out within the framework of this master thesis.

The ultimate goal of the presented project is a development of a Penning-trap mass spectrometer whose design and thus performance would be optimally adjusted to mass measurements of short-lived nuclides with very low production rates. One of the remarkable features of this design would be an employment of the same trap for cooling of the ion's motions as well as for a measurement of their frequencies. The trap is planned in the following way: First, helium gas for the cooling of the ion's motions has to be injected into the trap so that it reaches a pressure of $\approx 5{\cdot}10^{-5}$ mbar to ensure enough collisions of the buffer-gas atoms with the ions. Note that the cooling time constant is directly proportional to the helium pressure (combining eq. (3.4), (3.5) and (3.8)). Second, after successful cooling, the helium pressure has to decrease to $\lesssim 10^{-8}$ mbar in order to make a high-precision mass measurement of the trapped ions possible. Shortening this helium release time presents a major challenge and is one central topic in this chapter.

The key part to realize this cooling scheme is a piezo valve developed within the framework of this thesis. It enables a fast and precisely timed helium injection and exhibits a very low leakage in closed mode. The exact conditions it has to fulfill and the performance of the final design is shown in chapter 6.1.

Furthermore, the duty cycle of the mass spectrometer should be as fast as possible to enable measurements on short-lived nuclides. While the injection and the pressure build-up are mainly defined by the piezo valve, the helium release is defined by the pumping speed of the vacuum system.

The first idea was to install a transparent trap (see figure B.1), consisting of many thin electrode discs, to enhance the pumping cross-section in the trap region. With higher pumping speeds a stronger helium flow is required to enable the cooling pressure, which can be realized with the developed piezo valve. But due to this open Penning-trap geometry and higher helium flow the base pressure of the beamline would also rise to a quite high pressure ($\approx 5 \cdot 10^{-6}$ mbar, see figure 6.10 a)). This makes the helium pumping time slow again. In the appendix section B this problem was investigated in more detail and simulated with MOLFLOW [54], yielding a pumping time of ≈ 800 ms to reduce the pressure from 10^{-5} mbar to 10^{-9} mbar in the PILOT-Trap setup. To verify this simulation result a test station with helium injection was set up and the measured pumping time constants were compared to the simulated ones of this test setup, leading to an agreement within 25% and with that to a satisfactory verification of the simulation. Worth to note, the experimentally determined times were always longer than the simulated ones.

Due to the long pumping time, the open Penning trap approach will not be suitable to mass measurements on nuclides with half-lives shorter than a fraction of a second. Nevertheless, it can still be used for realizing the dynamic buffer-gas cooling technique for relatively long-lived nuclides.

This result triggered the question how to realize dynamic buffer-gas cooling and still enable measurements on short-lived nuclides. To enable measurements on short-lived nuclides with dynamic buffer-gas cooling, a completely closed trap is assumed, contrary to the original idea. Imagine a cylindrical Penning trap, which could be closed during the buffer-gas cooling and opened for the helium release at the end caps. With this, the idea is to use this instant increase of volume, by opening the trap, to achieve an almost instant decrease of the helium pressure in the Penning trap. Using the ideal gas law $pV = Nk_BT$, with p being the pressure, V the volume, N the number of particles (helium atoms), k_B the Boltzmann constant and T the temperature of the system (here room temperature), the pressure reduction of a perfectly closed Penning trap could be approximated. By assuming a trap volume of $V_{Trap} = 0.2\,\mathrm{l}$ (SHIPTRAP preparation trap has a volume of $174\,\mathrm{cm}^3$) and the PILOT-Trap beamline volume $V_{Beaml.} \approx 80\,\mathrm{l}$, the volume would be increased by a factor of 400, leading to a relative pressure reduction of $2.5 \cdot 10^{-3}$.

With this idea, the second goal to obtain short measurement times seems to be realizable. An additional positive effect would also be that less helium is needed to reach the cooling pressure, leading to a faster rise in helium pressure or lower mass flow through the piezo valve and especially not a constant helium flow like in the transparent trap.

The experimental realization of this closing trap idea, together with simulation results are described in chapter 6.2, after the now following presentation of the developed piezo valve.

6.1 Piezo Valve Performance

To realize the dynamic buffer-gas cooling the helium inlet has to be dynamically controllable, which is realized by a piezo disc taking advantage of the piezo electric effect. This effect describes the emergence of a voltage by changing electrical polarity, when mechanical stress is put on such a piezo element. Vice versa, applying an electrical field to those materials results in a deformation.

With such a piezo element a valve should be realized to enable a helium pressure of $\approx 10^{-5}\,\mathrm{mbar}$ by a present pumping speed of $S = 71\,\mathrm{l/s}$ (calculated by vacuum conduction formulas) in the Penning trap. Closing the valve should enable measurement pressures of $\approx 10^{-8}\,\mathrm{mbar}$. This results by using

$$p_{end} = Q \cdot S \tag{6.1}$$

in a leakage rate $Q \leq 7 \cdot 10^{-7}\,\mathrm{mbar\ l/s}$ for the piezo valve in closed mode. To reduce the helium release time, the valve should be placed directly next to the Penning trap, to minimize the so called "dead volume".

The development of the first piezo valve version showed that the distance between the sealing on the piezo towards the orifice is really important to be tunable from outside. This was realized by separating the piezo mounting structure and orifice on different flanges and sealing them with a FKM ring by adjusting fine screws outside the piezo valve, as realized in the second version (see figure 6.1).

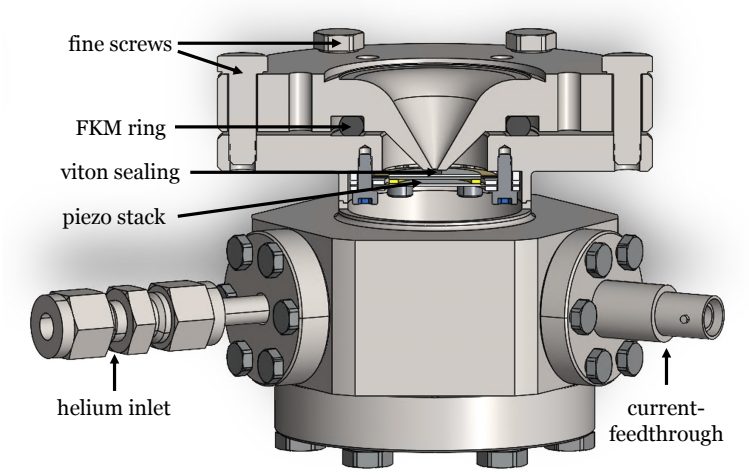

Figure 6.1: *Piezo valve version 2.0*
Shown are different components of the valve in a 5:8 scaling.

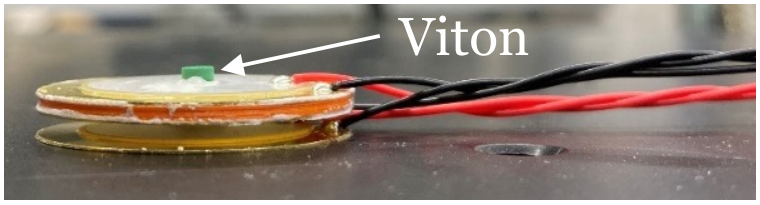

Figure 6.2: *Piezo stack with the attached viton sealing*
One piezo disc has a total thickness of 0.53 mm and an outer diameter of 27 mm. The sealing glued on top of the stack has a diameter of 3 mm. The piezo stack has a total height of ≈ 7.5 mm including the height of the sealing.

Enhancing the displacement of the piezo, by assembling three piezo discs into a piezo stack (see figure 6.2), made it possible to work with lower helium reservoir pressures in the valve, reducing the leakage rate in the closing mode. In addition lower helium reservoir pressures are more secure in case of failure.

For the characterization of the piezo valve a test setup was built, which mimics the pumping speed of $S = 75\,\mathrm{l/s}$ at the vacuum-side of the piezo valve using a turbomolecular pump. Therewith the measured pressure follows approximately the same pressure evolution as in the Penning trap (referenced as pressure Penning in

the following), since the tube diameter after the piezo valve has a diameter of 40 mm. In addition, a pressure gauge is also connected to the helium reservoir, measuring p_{He}. Both pressures were measured by recording the analog output signals of the gauge with an oscilloscope. These measured analog voltages can be calculated back to the pressure. Here it is important to classify the type of gas expected, since the calculated pressures of helium has to be multiplied with $K_{He} = 5.9$. To open and close the valve, the fast high-voltage push-pull switch developed at PENTATRAP [49] is used, switching the voltage from HV_- (closed) to HV_+ (open). Applying negative voltages to the piezo deforms it in the other direction, which can be used to enhance the force on the sealing to tighten it more. But just voltages down to $HV_- = 150\,\mathrm{V}$ can be applied, since for even lower voltages a switching polarity of the piezo was observed. The applied voltage on the piezo has been recorded with an high-voltage probe.

With this setup, the pressure evolution for an opening time down to 100 ms was measured, leading to the aimed performance shown in figure 6.3 for $p_{He} \approx 6.4\,\mathrm{mbar}$ and $HV_+ = 400\,\mathrm{V}$ with an orifice diameter $d = 1.5\,\mathrm{mm}$. The leakage rate of the piezo valve in closing mode was investigated by attaching a leak detector to the setup. This is measured as a function of the helium reservoir pressure and HV_-, presented in figure 6.4. In these plots the leakage rates of the piezo valve with an orifice of 1.0 mm are added. Latter setup has achieved a comparable pressure evolution at $p_{He} \approx 12\,\mathrm{mbar}$. But for the smaller orifice the distance between orifice and piezo had to be enhanced, to achieve comparable helium fluxes in open mode, which results in an overall higher leakage rate in figure 6.4 a). Nevertheless, the proportionality to p_{He} is the same, as expected. In contrast the slope for $Q(HV_-)$ differs for the two different orifice diameters. Since the leakage is proportional to the area of opening, which in this case is the product of orifice perimeter and distance between orifice and sealing, the slope should be proportional to the radius of orifice. Therewith the ratio of slopes should equal the ratio of orifice radius, which is approximately observed here.

In figure 6.5 the pressure evolutions for different HV_- and different p_{He} are presented in a) and b), respectively. As can be seen, the stahl-electronics voltage supply can not deliver enough current to reach the set $HV_+ = 450\,\mathrm{V}$. Lower HV_- weaken the maximal voltage reached even further. It is assumed that the first pressure rise is due to the PID regulator in the pressure gauge and has to be investigated by using another pressure gauge. As proofed in sub-figure b) the pressure after the piezo valve is proportional to p_{He}.

The base pressure in the shown measurements seems to be high, but has to be divided by K_{He}. This assumption that the observed base pressure is not due to leakage in the closed mode is supported by the measurement of pressure evolution for different helium reservoir pressures. There higher helium pressure would result in a greater leakage rate Q and with eq. (6.1) lead to different end pressures assuming a constant pumping speed S, which is not observed here. Dividing the measured base pressure of figure 6.5 b) of $4{\cdot}10^{-7}$ mbar by K_{He} leads to a base pressure of $7{\cdot}10^{-8}$ mbar assuming the gas type of air. This high base pressure is attributed to outgassing

of the used FKM sealings and the outgassing of the used viton sealing. Latter assumption is supported by the comparison of base pressures for both measurements pictured in figure 6.5. The measurement presented in b) is recorded one day after the one in a) and shows a lower base pressure, which is due to the reduction of outgassing over time of pumping. Thus the base pressure can be further improved when the piezo valve (or the test setup) is baked out.

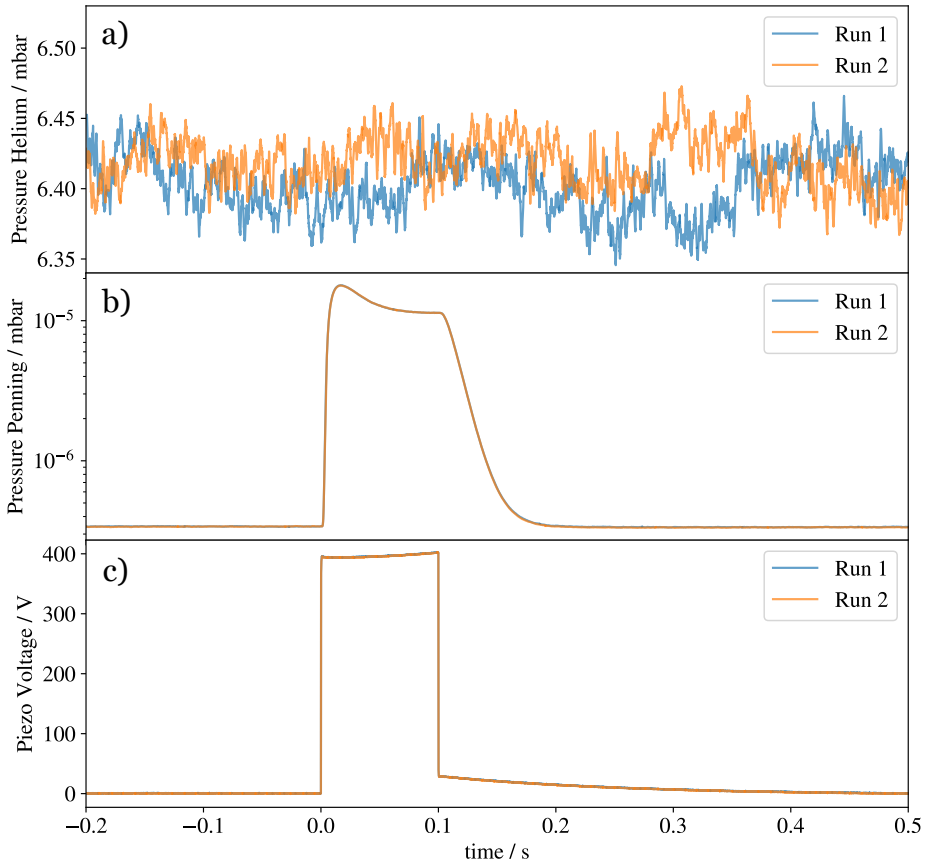

Figure 6.3: *Reproducible fast cooling pressure rise with the developed piezo valve* a) displays the recorded pressure in the helium reservoir, which stays constant during the measurement. The measured cooling pressure rise behind the piezo orifice is displayed in b), which is proportional to the opening of the piezo vale. The latter depends on the applied voltage on the piezo stack, which is presented in c). As can be seen in b), a precisely timed helium injection realizes a cooling pressure rise up to 10^{-5} mbar. When the piezo valve closes at 100 ms, the pressure decrease in the simulated Penning trap depends on the pumping speed of the system.

In an attempt to decrease the helium reservoir pressure even further, voltages up to 1 kV were used in order to enhance the piezo displacement. This was realized with the high-voltage power supply of the detector. With applying greater HV_+ it was

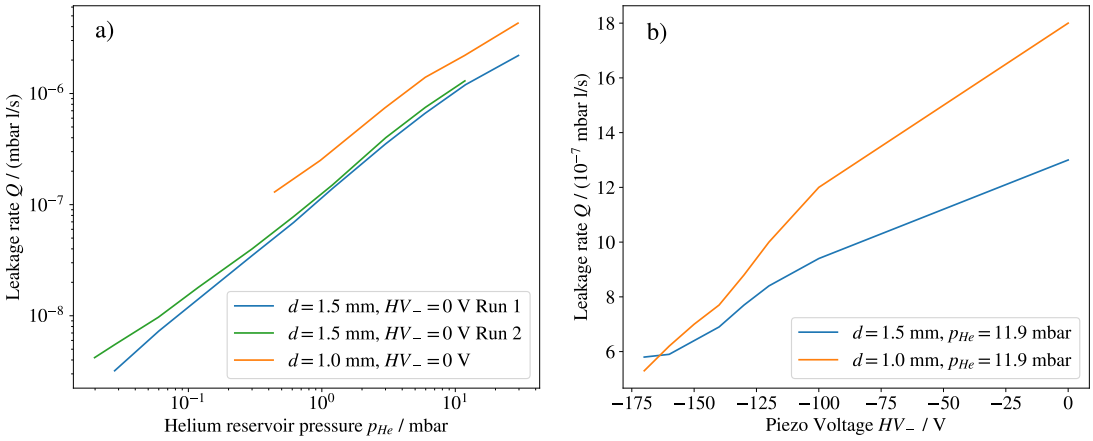

Figure 6.4: *Leakage rate characterization of the developed piezo valve*
The dependency of the leakage rate on the helium reservoir pressure of the piezo valve in closed mode is displayed in a). The graphs in b) presents the measured leakage rate for different applied voltages HV_- in the closed mode of the piezo valve. Lower HV_- increase the contact pressure force of the sealing on the orifice, resulting in a lower leakage rate.

possible to reduce p_{He} to 0.3 mbar and thus the leakage rate by a order of magnitude. One notices in figure 6.6 the different voltage rise compared to when the other power supply was used. This behavior has to be investigated in more detail together with the influence of the additional capacity of the high-voltage probe used to measure the voltage evolution. Whether such high voltages near the Penning trap can be used without affecting the trapping potential has to be investigated. Nevertheless, it shows another parameter to tune in order to realize the desired pressure evolution while reducing the leakage rate by lowering the helium reservoir pressure. But one has to pay attention when using higher voltages, since flashovers may occur for certain pressures, which was also observed here. Besides increasing the voltage, a higher number of stacked piezos can be used to enhance the deformation. But since the piezo valve should be as compact as possible this option was discarded.

In addition teflon was tested as a sealing material with this configuration. The reservoir pressure had to be chosen larger compared to that used in the configuration with a viton sealing, as sealing with teflon turns out to be more difficult to achieve. This is due to the more rigid property and the difficult alignment of the sealing parallel to the orifice but could be solved by enhancing the force of the sealing towards the orifice by tighten the fine screws. This is the reason why only higher voltages (> 500 V) and one order of magnitude higher reservoir pressures achieve a comparable pressure evolution in the simulated Penning trap, as displayed in figure 6.6. Furthermore the leakage rates were measured for the comparison of sealing materials, which is presented in figure 6.7. As can be seen, the leakage

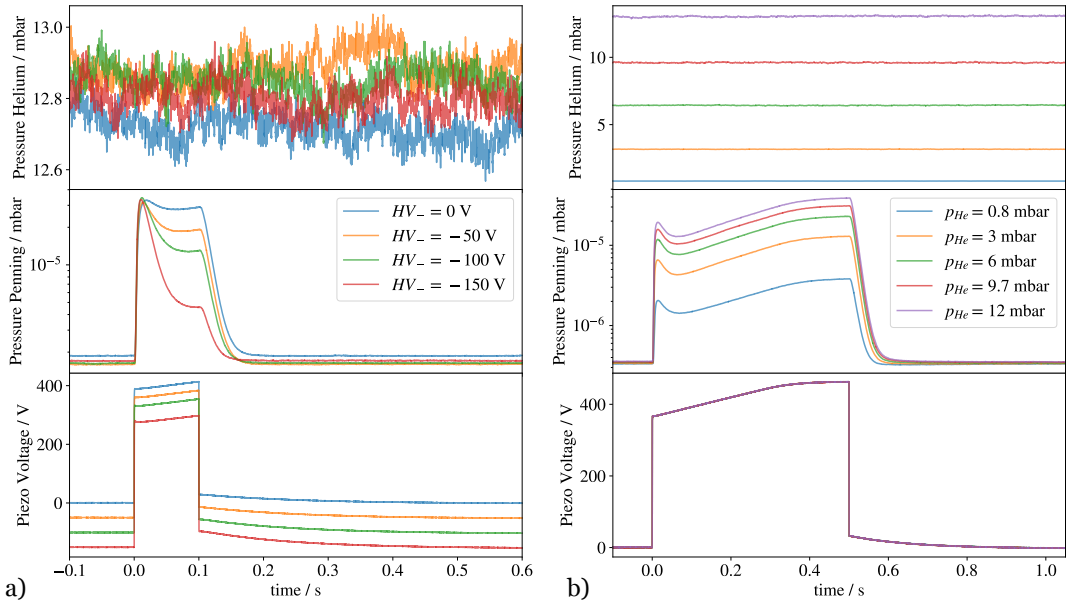

Figure 6.5: *Comparison of cooling pressure rises for different HV_- voltages in closed mode and different reservoir pressures*
Analog to figure 6.3, the respective subplots presents, from top to bottom, the recorded pressure in the helium reservoir, the measured pressure rises behind the piezo valve and the voltage applied to the piezo stack during the measurement.
a) shows the different pressure rises for different set HV_-, whereas HV_+ was always set to 450 V.
b) displays the different pressure rises for different helium reservoir pressures p_{He} with set voltages of $HV_- = 0$ V and $HV_+ = 450$ V.

rate using teflon is lower for all helium reservoir pressures, compared to the viton sealing. This can be attributed to the tighter mounting of the teflon sealing. But comparing the leakage rate at the used reservoir pressures respectively (to achieve the typical cooling pressure), leads to a leakage rate of $\approx 10^{-8}$ mbar l/s for both sealing materials. With this result, viton will be used further as sealing material, since it enables using lower reservoir pressures.

With this successful characterization of the piezo valve, the final version was designed to be mounted next to a Penning trap and to fit inside a CF100 tube by minimizing its total volume to a total height of 22 mm with a maximal radius of 34.5 mm. For simplicity and other applications, the adapter to connect this valve was chosen to be a CF16 flange. The two flanges with fine screws were displaced by KF flanges, so that with a KF clamping ring the distance between sealing and

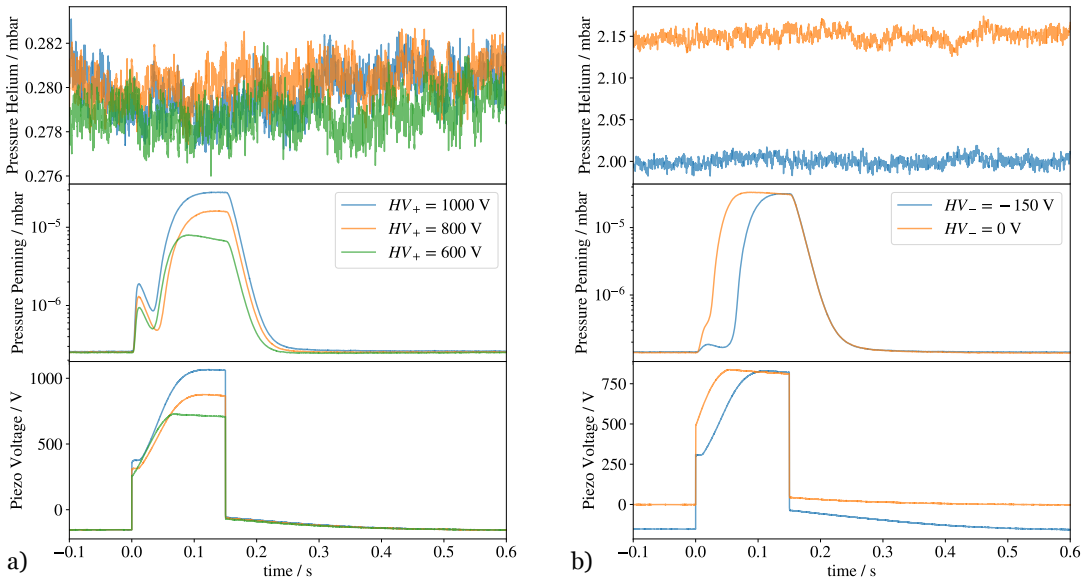

Figure 6.6: *High-voltage piezo valve pressure rise for different sealings*
Analog to figure 6.3, the respective subplots presents, from top to bottom, the recorded pressure in the helium reservoir, the measured pressure rises behind the piezo valve and the voltage applied to the piezo stack during the measurement.
a) Piezo valve with viton sealing at $HV_- = -150\,\mathrm{V}$, $HV_+ > 500\,\mathrm{V}$ and $p_{He} = 0.28\,\mathrm{mbar}$.
b) Piezo valve with teflon sealing at $HV_- = 0\,\mathrm{V}$ and $HV_- = -150\,\mathrm{V}$, $HV_+ = 750\,\mathrm{V}$ and $p_{He} \approx 2\,\mathrm{mbar}$.

orifice can be adjusted by only one screw from the outside. In addition, this ensures a uniform displacement of the piezo plane towards the orifice, in contrast to the displacement via the screws. This flexible displacement setup takes up most of the volume of the assembly. To save space, the voltage feedthrough was omitted and the isolated power line is feed through the helium line. This design is presented in figure 6.8.

Since this final piezo valve design is still manufactured, it could not be tested yet, but it is expected to lead to the same results as the version presented before, as long as the displacement via the KF clamping ring works.

With the achieved compact and simple design it can easily be recreated and used for different applications, especially in Penning traps. The final performance to realize the dynamic buffer-gas cooling technique will be tested together with the rotating disc approach, which will be presented in the following chapter.

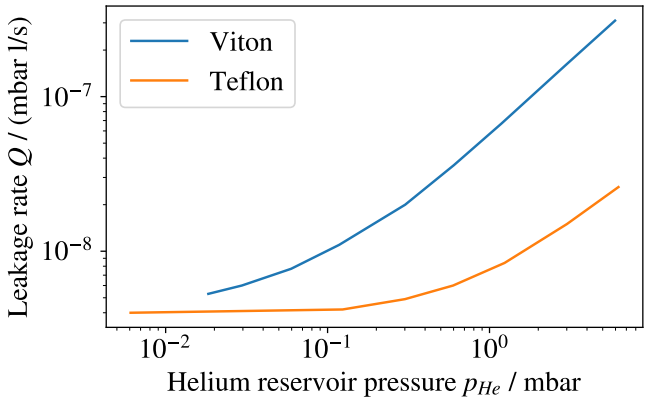

Figure 6.7: *Piezo valve leakage rate comparison for viton and teflon sealing*
Both measurements were performed at $HV_{-} = -150\,\mathrm{V}$ in closed mode and same screw settings as used to achieve the recorded cooling pressure rises in figure 6.6.

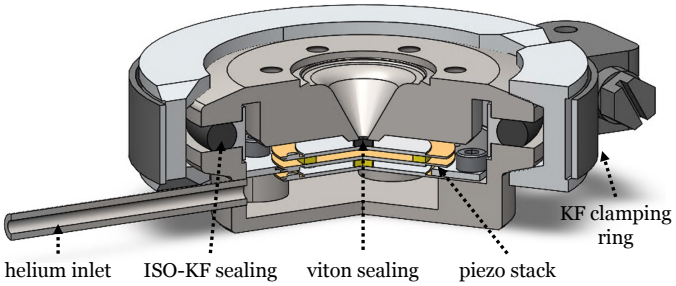

Figure 6.8: *Minimized piezo valve design*
This minimized piezo valve has a total height of 22 mm and a maximal radius of 34.5 mm. This makes it suitable for attachment to a Penning trap. To save space the isolated poser line is feed through the helium inlet.With the KF clamping ring the distance between sealing and orifice can be adjusted by only one screw.

6.2 Closed Penning Trap with Rotating-Disc Approach

As already described in the introduction of this chapter, a closed trap design should be used to reduce the time needed to pump the helium out of the trap region, to enable a fast following measurement. The idea is to use a fast increase of the volume by opening the trap in order to provide an immediate pressure drop of helium in the Penning trap.For this, the trap has to be closed at its ends when the helium is injected into the trap until the buffer-gas cooling has finished. Afterwards the trap has to be opened to release the helium to start a PI-ICR measurement cycle.

A challenging task is the fast opening and closing without introducing systematic effects to the measurement. Any electromagnetic actuators are out of question, since they are unacceptably slow in strong magnetic field.

The approach of using a continuously rotating disc consisting of isolating material was favored. The disc is mounted on an axle, which is radially offset from the symmetry axis of the trap. An excentric hole inside the rotating disc leads to a periodic release of helium.On the other hand, the disc is closed at the opposite side of the orifice, to enable the helium pressure rise in the Penning trap, when opening the piezo valve, without affecting the base pressure around. The rotating speed is set by a servomotor, placed outside at the end of the beamline, about 1 m away from the magnet. An isolating material was chosen to avoid eddy currents by the strong magnetic field, which would slow down the process of rotation. It is assumed that ions hitting the disc in closed mode will imprint charge on its surface, which is carried away by the released helium in open mode.

The most important parameter is the distance of the discs towards the ends of the Penning trap, which will define the tightness of the trap in closed mode. However, the distance can not be made arbitrarily small, to ensure no transfer of vibrations on the Penning trap. This rotating disc approach was simulated in MOLFLOW for different distances reaching from 1 mm to 100 μm. The simulation setup consists of a trap with radius 16 mm and length 218 mm placed in a simplified beamline of PILOT-Trap without any ion optics inside. The results are shown in figure 6.9. There the red graph demonstrates a relative pressure drop of $3 \cdot 10^{-3}$ within 25 ms with an ideal closed trap, as predicted by the ideal gas law. In addition, one sees that a distance of 100 μm leads to a pressure drop close to that of an ideal closed trap. The reason for dropping to a higher pressure compared to the ideal closed trap is the rise of the base pressure around the trap, which is directly proportional to the distance of the discs towards the trap. The rise in base pressure caused by leakage through the slits is presented in figure 6.10 a). These were obtained by simulating the pressures near the closing Penning trap. This leakage rate is directly proportional to the pressure inside the trap, whereas the base pressure is directly proportional to the leakage rate (see eq. (6.1)). Thus, an immediate pressure drop p_{drop} of 10^{-2} mbar is always observed for different helium flows (and therewith different cooling pressures) by a distance of 100 μm, which is shown in figure 6.10

b). This distance was taken for simulation, since 100 μm seemed to be feasible after consultation with the manufacturer.

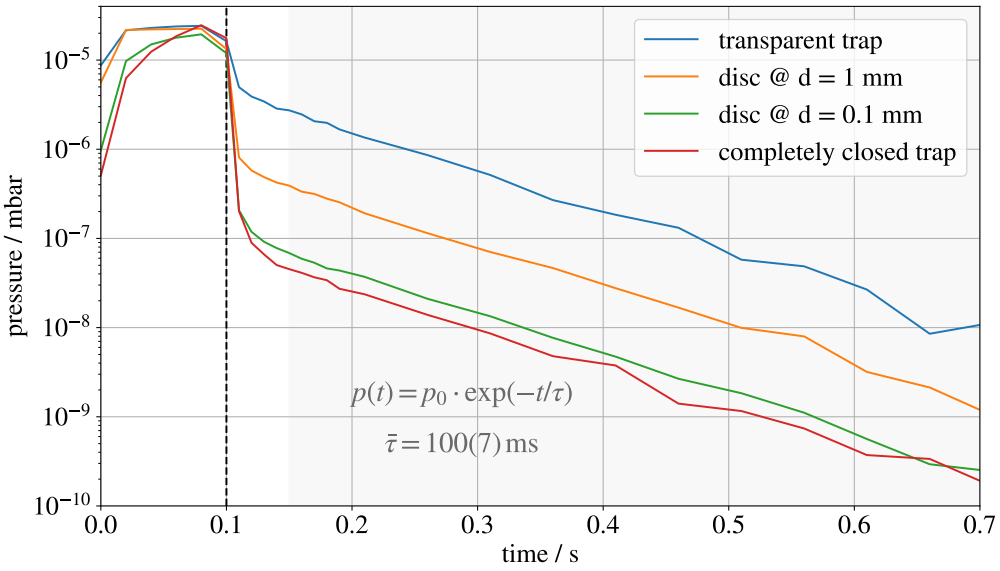

Figure 6.9: *Comparison of MOLFLOW simulated pressure evolutions in PILOT-Trap with open and closing Penning-trap using the rotating-disc approach at different distances*
The dashed line indicates the time the piezo valve closes. At the same time the rotating discs open. An exponential decay was fitted to the pressure curves in the gray shaded area resulting in an average pumping constant of 100(7) ms.

In this approach, the helium pressure p_{He} is used as a parameter to optimize the total cooling time. While a higher pressure directly reduces the cooling-time constant t_{cool} during buffer-gas cooling, it also increases the time t_{pump} needed for pumping out the buffer-gas after the rotating disc opens. Therewith, the total cooling time $t_{tot} = t_{cool} + t_{pump}$ is a function of helium pressure assuming an immediate pressure drop from p_{helium} to p_{drop}.

Using this technique, the time used to pump the trap region from 10^{-5} mbar to 10^{-8} mbar was found to be 200 ms as determined by simulations, while the completely open trap would need 600 ms.

This reduction of factor three is the result for the current PILOT-Trap beamline design as well as for a SHIPTRAP-like Penning trap [55]. Of course, this rotating-disc approach offers possibilities to further shorten this release time. Increasing the pumping speed S with better turbo pumps or using pumps with higher compression ratios for helium would further reduce t_{pump}. Furthermore, it would decrease the base pressure by same leakage of the closed trap (see eq. (6.1)), which would then

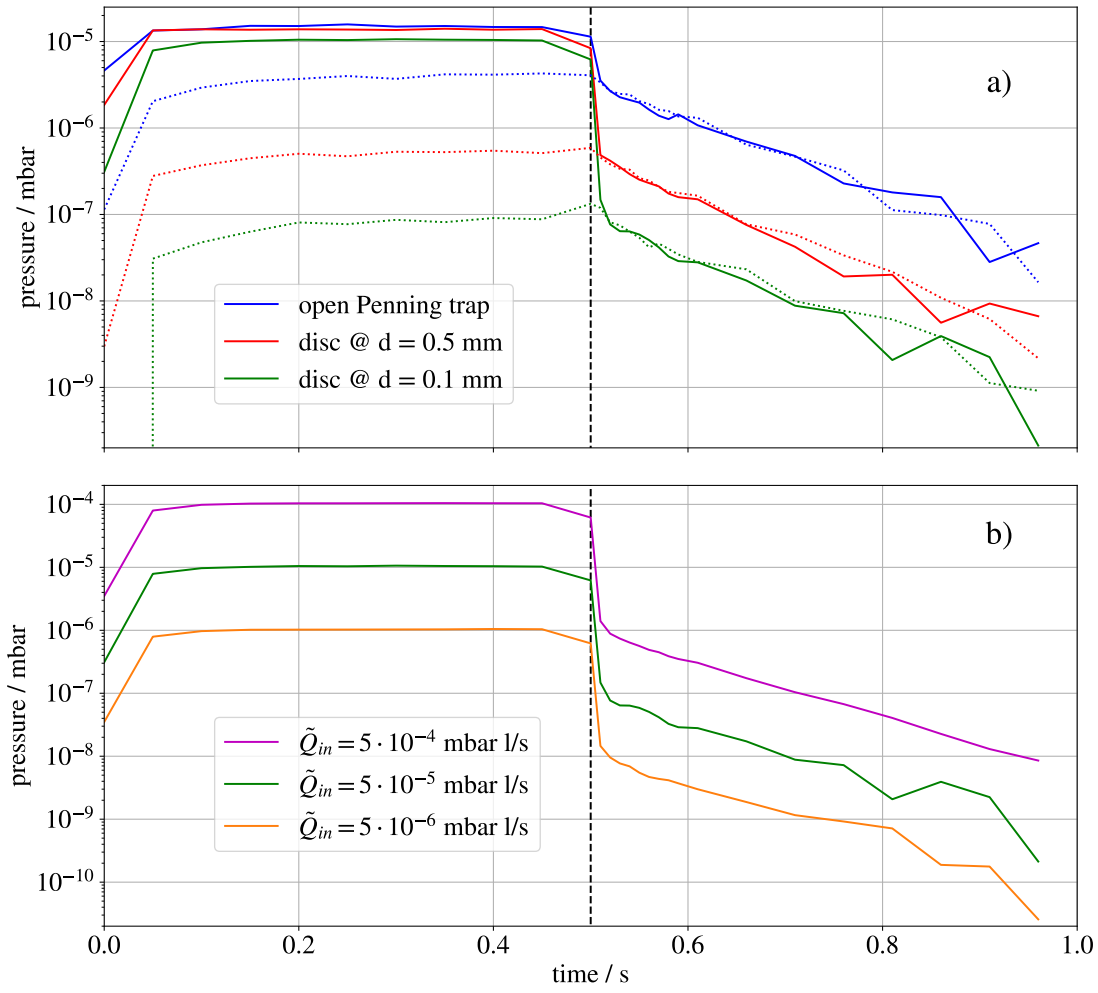

Figure 6.10: *Evolution of pressure inside a Penning trap using the rotating-disc approach simulated with MOLFLOW*
The dashed line in both plots indicates the time the piezo valve closes and the rotating discs open. Besides the pressures in the trap which are displayed as solid lines, the base pressure next to the trap is shown as dotted line.
The comparison of pressure evolution for different disc distances d and the transparent trap is shown in a). Thereby the inlet flux of helium was set to achieve a pressure of 10^{-5} mbar in the trap. Lower leakage through the disc distance reduces the base pressure and enables higher pressure drops when opening the trap.
In figure b) different helium inlet fluxes are simulated for a disc distance $d = 0.1$ mm.

enable higher pressure drops by opening the trap. The pumping speed can also be increased by enhancing the pumping cross-section at the trap using bigger tubes in the beamline towards the trap. In addition the larger tubes would also lead to a greater volume, so that a higher pressure drop can be realized in the ideal case, only limited by the base pressure. Contrary to increasing the volume of the beamline, the reduction of the trap volume would also increase the possible pressure drop. But one has to pay attention choosing the trap radius big enough to enable good ion trapping from the source.

A comparable technique was once attempted in a diploma thesis at SHIPTRAP [55] by the development of a pumping barrier, where an improving by a closing piezo between cooling and measurement trap was investigated. At measurements, where the piezo movement was not working, the barrier solenoid was implemented in closing mode by pulling it in the small channel of radius 2 mm to investigate the residual permeability. The distance of this solenoid towards both sides of the tunnel is not clear defined in the thesis, but could be estimate by the tolerances, which were stated to be 100 μm. This improved the pressure ratio between cooling and measurement volume by factor of 3 [55] compared to without the solenoid. In addition it has to be stated, that the thin (radius of 2 mm) pumping barrier channel with a length of 2 mm without the solenoid let to a pressure ratio of $8 \cdot 10^4$ by the same helium inlet of 0.6 mbar l/s. Referencing this results should not state that only using the solenoid would lead to a pressure ratio of $\approx 2.5 \cdot 10^5$, since the pumping barrier by the small channel is influencing the pressure reduction as well, but should state that this solenoid has improved this pressure ratio further, supporting the rotating disc approach.

With the above simulation results and supporting investigation at SHIPTRAP, it was decided to investigate the rotating disc approach closer for which the following described test setup was constructed.

6.3 Experimental Test of Rotating Disc Approach

The designed test setup to verify the rotating-disc approach is pictured in figure 6.11.

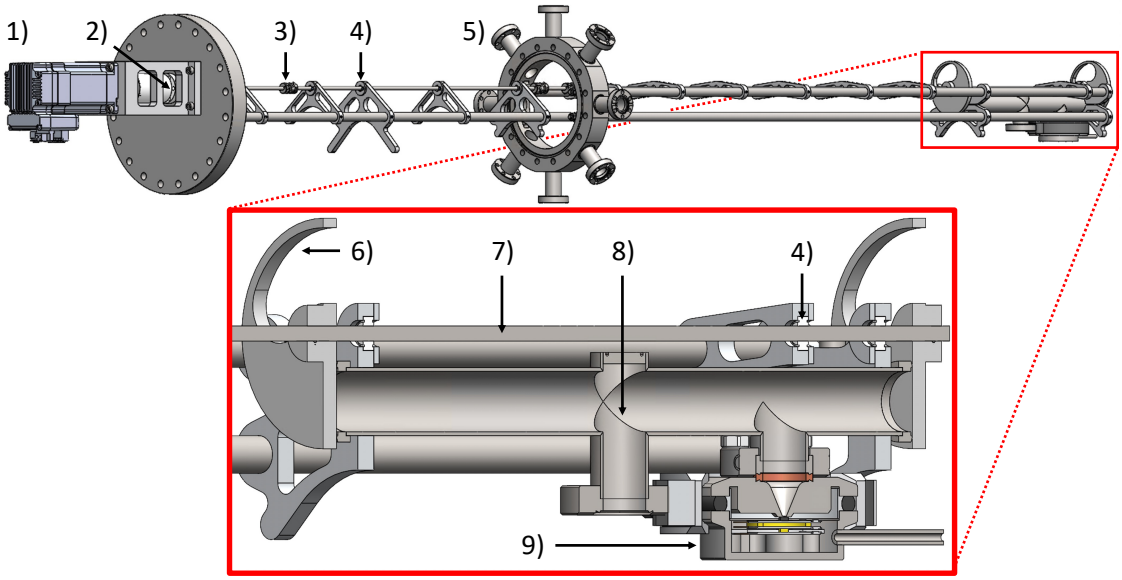

Figure 6.11: *CAD model of the test bench for the rotating-disc approach*
1) servomotor, 2) rotary feedthrough 3) coupling to dampen vibrations, 4) ceramic ball bearings, 5) feedthrough flange, 6) open area of rotating disc, 7) stainless steel rotary axis, 8) bulge to place the self-designed mini pressure gauge, 9) developed piezo valve

For easier construction a CF16 tube with inner diameter of 16 mm is used to simulate the Penning trap. Even though the covered volume is smaller by a factor of two compared to the used Penning trap, the design for the discs and their holding aperture were easier to realize. In the middle of the tube a small bulge is placed with a CF16 adapter to install a self-designed mini pressure gauge to record the pressure rise induced by the piezo valve and the following pressure drop by opening the trap. At a certain distance of 60 mm towards the center another bulge with CF16 adapter is placed to connect the piezo valve (see section 6.1). The ends of the tube feature knife-edges, so that the tube could also be connected directly to a pumping system. This setup is designed to test whether the piezo valve and pressure recording works and all sealings are tight. In this configuration an additional commercial pressure gauge should be installed to calibrate the developed pressure gauge. The Penning trap tube is held by four rods connected to the feedthrough flange, analog to the current design of PILOT-Trap.

The non magnetic stainless steel axle of rotation is supported to the two upper rods using ceramic ball bearings. Insulating materials are favored to avoid eddy currents. But materials such as teflon or ceramics could not be used for the rotation axle

because they are too flexible or brittle, respectively. The rotating discs are mounted on the axle in such a way that they can be moved to set different distances. This part of rotary axle extends to the feedthrough flange, where it is connected to the rotary axle leading to the end of the beamline by couplings to absorb vibrations and changes in length. Thermal length changes of the axle can be neglected, since the thermal expansion coefficient $\alpha_c = 17 \cdot 10^{-6}\,\mathrm{K}^{-1}$ is sufficiently small. Latter rotary axle part is divided into other smaller parts, which are also connected with couplings to dampen the expected stronger vibrations near the servomotor. Two rods attached to the outer flange support this part of rotation axle to ensure that the vibrations are not transmitted to the support of the simulated trap.

This configuration then should be installed in the PILOT-Trap beamline. At first, the magnet should stay ramped down to test the rotating-disc approach in normal environment and to tune the piezo opening voltage and time to obtain the typically used cooling pressure. When this test is successful, the magnet should be ramped up to see the influence of the magnetic field on the rotating discs. The magnetic field will of course distort the measured pressure, but the relative pressure drop should still be measurable in this configuration.

In addition, a vibration measurement should be carried out, by opening the beamline at the side of the detector. Then the outer disc should be dismounted and a quadrant photodiode sensor should be mounted on the Penning trap holder rods. Outside of the beamline a laser should be placed, pointing in the center of this sensor. By turning on the coldhead, vibrations caused by the magnet should be detected. Additionally the servo motor should be run afterwards to investigate vibration transfer of the rotating disc on the Penning trap. Furthermore vibrations transferred from the piezo valve can be examined.

Unfortunately the manufacturing of the construction parts were not finished in the time frame of this thesis and the PILOT-Trap beamline was still used to investigate the PI-ICR technique, so that the rotating disc verification is still pending.

7 Upcoming Improvements

7.1 PI-ICR Realization

With the latest result, the buffer-gas cooling was successfully implemented in PILOT-Trap. Using larger excitation amplitudes at the same phase evolution times for the magnetron motion showed phase differences compared to the spots at lower excitation amplitudes. Therefore, spots for the same phase evolution time at different excitation amplitudes are not on a straight line. Since the magnetron motion is mainly influenced by the electrical field, optimizing the tuning ratio TR to minimize this phase divergence for different excitation amplitudes will reduce the electrical field inhomogeneity. Of course, the excitation radii used to project the pumping barrier on the detector are too high not to expect any inhomogeneities and will not be used in later measurements. Nevertheless, this optimization will harmonize the trap and be even more precise when the phase evolution time will be enhanced during this optimization.

After harmonization of the trap, the magnetic field inhomogeneity can be investigated using the same procedure with enhancing the excitation amplitude of the modified cyclotron amplitude. Increasing the phase evolution time and ensuring no phase divergence on lower excitation radii will resolve the magnetic inhomogeneity on greater radii even more. This data can then be used to design shimming coils, to improve the magnetic field homogeneity especially by reducing the B_2 coefficient to improve the measurement precision. To realize this optimization with the modified cyclotron motion the helium has to be released out of the trap so that the damping caused by the buffer-gas is not present anymore. With the latest implementation, it is now possible to dynamically open and close the used fine dosing valve during a measurement cycle with the implemented TTL logic. This is in the current setup sufficient enough to perform the above mentioned optimization, even so the measurement duty cycle increases a lot due to the slow helium release. But since stable isotopes of rubidium are used and the trapping was demonstrated for times above a second it is feasible. In addition, the Penning trap can be moved on the symmetry axis of the magnet to scan the area of homogeneity, which is possible up to distances of 25 mm in both directions due to the implementation of bellows.

When trying to realize the projection of the pumping barrier on the delay-line detector by lowering the potentials at the drift electrodes in the ejection path of the ions, the circular ring consisting of magnetron excitation spots at different phase evolution times but same excitation amplitudes converted to an ellipse (compare figure 5.8 c) and d)). This effect is even more pronounced for rings at higher excitation radii. Thus, it seems to be due to lens effects between the different drift

electrodes at different potentials in the ejection path of the ion. Simulating the ejection path potentials with SimIon [56] analog to [57] will ensure a radial conserving projection of the ion motion on the detector. This simulation should be addressed at the same time or even before the optimization mentioned above. In addition, a misalignment of the trap axis towards the magnetic field symmetry axis could also be the reason for the observed elliptical ring shape. Since this alignment is time consuming it should be done after the new trap design is built in.

7.2 Vibrations

With implemented and optimized PI-ICR measurement technique as mentioned above, the vibration can be investigated closer by studying the phase stability at different time distances towards the vibration. Additional information about the Penning-trap's magnitude of vibration will be given with the quadrant photodiode sensor measurement when testing the rotating disc approach. The transfer of vibration due to the coldhead and the rotating disc can then be investigated as already described in chapter 6.3.

7.3 Dynamic Buffer-Gas Cooling Technique

The dynamic cooling technique with the developed piezo valve, mini pressure gauge and rotating disc approach should be tested after all priorly mentioned optimizations. A successful test of the piezo valve would enable dynamic buffer-gas cooling, whereas the rotating disc is expected to reduce the helium release time from $\approx 600\,\mathrm{ms}$ to $\approx 200\,\mathrm{ms}$ (see chapter 6.2), enabling mass measurements on short-lived nuclides.

Next to the already in chapter 6.2 mentioned design improvements of the Penning trap to enhance the performance of the rotating disc approach, the new design should combine the properties of a cooling and measurement trap, since currently a cooling trap design is implemented in PILOT-Trap. Since for the fast pressure drop no pumping barrier will be implemented in the trap, the disc facing the detector can be upgraded to function like the pumping barrier for the capture of contaminated ions on greater magnetron radii. This can be achieved by extending the orifice by a smaller aperture arc (quarter circular slit). When designing the new setup of PILOT-Trap, perforated drift electrodes like the already used DT4 or electrodes consisting of thin discs, like the transparent trap design (see chapter B), should be used to enhance the pumping cross-section in the beamline.

7.4 Cryogenic Buffer-Gas Cooling

In the introduction of the buffer-gas cooling technique, it was stated, that the ion spot size depends on the squared temperature, see eq. (3.9). Thus, it is possible to reduce the ion's spot size using colder buffer-gas. Buffer-gas at a temperature of 50 K would reduce the spot size from $\approx 84\mu$m to $\approx 34\mu$m and would directly lead to a gain of factor 2.4 in precision, since the error on frequency is directly proportional to the spot size (see eq. (3.19)), assuming the same excitation radius.

The reduced spot size can also be exploited by using lower excitation radii as long as the different spots can be resolved to adequate precision on the MCP. This would reduce the frequency resolution but would also greatly reduce systematic frequency shifts which mostly scale with the ion's motional amplitudes.

The used coldhead cryo-cooled magnet has the advantage that the penning trap can be directly connected to the radiation shield which is cooled down to 40 K. The connection of a Penning trap to the radiation shield of this magnet was already performed in the Kellerbauer group, where they cooled the electrodes of the trap down to 65 K [39] with four copper rods. Assuming this temperature would be also reached by the buffer-gas the spot size would be reduced by a factor of 2.1.

The piezo valve should be connected to the trap with structures of high thermal resistance to allow for a higher temperature and therefore more reliable working conditions. Using buffer-gas at room temperature would warm up the piezo as well, improving the mobility of the piezo too. With this idea, the helium at a temperature of 300 K would be injected into the cold Penning trap, colliding with the electrodes and cooling the ions further down than before, until everything is equalized at the temperature of the electrodes.

To study this method in more detail, calculations have been carried out to determine the cooling time and number of collisions N_{coll} of one buffer-gas atom with the electrodes needed to reduce the buffer-gas temperature $T_g = 300\,\mathrm{K}$ to the cooled electrodes temperature $T_s = 40\,\mathrm{K}$ or $T_s = 40\,\mathrm{K}$. The Maxwell model is used to describe the interaction between gas and its surrounding surface. Therefore, the energy accommodation coefficient

$$\alpha_E(T_s, T_g) = \frac{E_i - E_r}{E_i - E_s} \tag{7.1}$$

is used, which describes the ratio of the average exchanged energy between the thermal energy of the incident gas E_i and the thermal energy of the reflected gas atom E_r divided by the maximal thermodynamic possible exchange energy between E_i and the thermal energy of the surface E_s. Therewith, α_E can be treated as a loss coefficient of transversal momentum of the gas, when diffuse-reflected on the surface. The value of α_E depends on the surface material as well as on the gas nature, temperature and pressure, where for cryogenic temperatures values about 0.3 to 1 have been stated with the maximal value of 1 representing a perfect accommodation. For cryogenic design estimation purposes $\alpha_E \approx 0.5$ is stated to be reasonable [58].

The study of this cryogenic buffer-gas realization approach is verified by calculations assuming a travel distance of a buffer-gas atom between two collisions with the surface of $d_1 = 216\,\text{mm}$ and $d_2 = 32\,\text{mm}$, which equals the length and the diameter of the used Penning trap, respectively. Equalizing the thermal energy $E_{th} = 3/2 \cdot k_B T$ with the kinetic energy and subtracting the exchanged energy for every collision for different α_E lead to the computation results shown in figure 7.1 for $T_s = 40\,\text{K}$ and figure 7.2 for $T_s = 4\,\text{K}$.

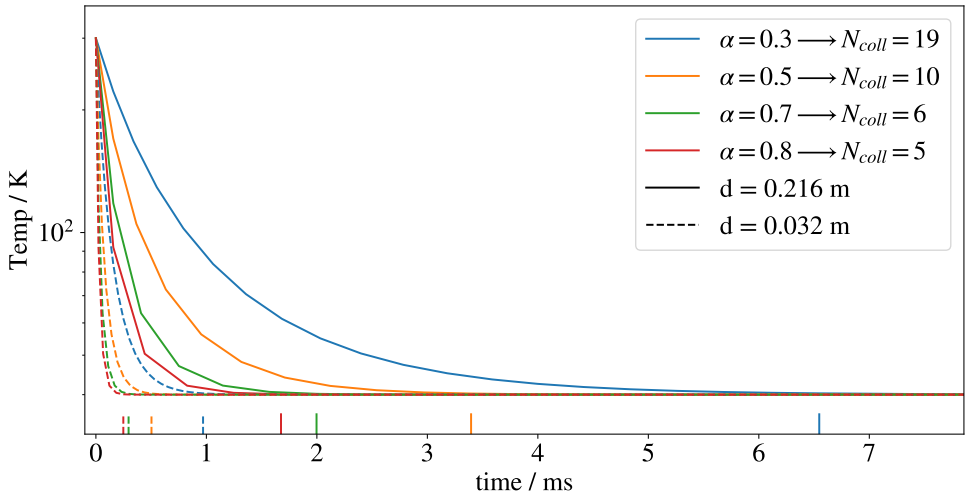

Figure 7.1: *Cooling time of buffer-gas at room temperature in a cryogenic trap at* $T_s = 40\,K$
The dashed and solid lines display the calculated cooling processes of the inlet buffer-gas at room temperature into a cryogenic Penning trap at $T_s = 40\,\text{K}$ by assuming a travel distance of the Penning trap length of 216 mm and diameter of 32 mm, respectively, between collisions of buffer-gas atoms with the electrode walls. The respective vertical lines indicate the times when the reached temperature of the buffer-gas deviates by one percent from T_s.

This results in cooling times of $< 7\,\text{ms}$ for $T_s = 40\,\text{K}$ and $< 25\,\text{ms}$ for $T_s = 4\,\text{K}$. With these estimated cooling times the realization of cryogenic buffer-gas seems to be realizable. One has to further investigate the influence of an open trap or the heating influence of collisions with the disc at room temperature when using the rotating disc approach.

A comparable cryogenic buffer-gas cooling was already performed in California [59]. In this paper, the cooling of a trap-based positron beam in a buffer-gas trap (BGT) and cryogenic beam-tailoring trap (CBT) is stated, which results are summarized in the following. Thereby they cool the positrons with 300 K nitrogen within 0.1 s in the BGT to room temperature and transport the positrons in the CBT. Later consists of eight cylindrical electrodes surrounded by a tube, which are connected to

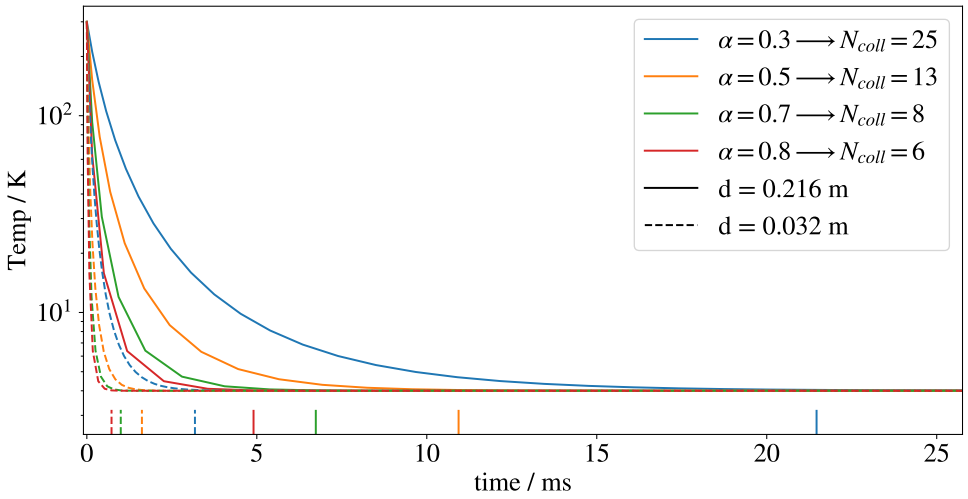

Figure 7.2: *Cooling time of buffer-gas at room temperature in a cryogenic trap at* $T_s = 4\,K$
The dashed and solid lines display the calculated cooling processes of the inlet buffer-gas at room temperature into a cryogenic Penning trap at $T_s = 4\,\mathrm{K}$ by assuming a travel distance of the Penning trap length of 216 mm and diameter of 32 mm, respectively, between collisions of buffer-gas atoms with the electrode walls. The respective vertical lines indicate the times when the reached temperature of the buffer-gas deviates by one percent from T_s.

a cryo-cooler remaining at a temperature of 12 K, yielding an electrode temperature between 46 K and 54 K. Now CO buffer-gas at room temperature is injected between the outer tube and electrodes, where it cools down to $\approx 50\,\mathrm{K}$, before it finds its way into the inner of the electrodes, where a typical pressure of $\approx 1.3 \cdot 10^{-6}\,\mathrm{mbar}$ is prevailing, cooling the positrons for 0.2 s. The cooling times are presented here to give an estimate of the order of magnitude. Of course, these will vary here since ions with higher mass and lighter buffer-gas will be used.

This cooled buffer-gas approach could be further improved, when the trap is connected to the 4 K second stage of the magnet, by connecting it to the coil holder, which is accessible. But it has to be considered that the electrodes temperatures have to be higher than 4.2 K, so that the helium does not liquefy in the Penning trap. This can for example be handled by attaching a resistive heater to the trap. But if in this case the piezo valve fails and lets in a continuous flow of helium in the trap, the heat load may be higher than the cooling power of the stage, warming up the coil and leading to a quench. In contrast to that, the transferred heat-load of the buffer-gas at a typical pressure of $\approx 10^{-5}\,\mathrm{mbar}$ in the Penning trap is negligible. In addition, the radiation heat-up has to be taken more into account, which can also be used to ensure $T_s > 4.2\,\mathrm{K}$.

Nevertheless, the realization of the cryogenic buffer-gas cooling would entail more advantages than the reduction of the spot size. By dismounting the installed warm bore the setup would then be cryo-pumped. Thereby, the base pressure in the beamline would be reduced and molecules like water would freeze out, enabling longer phase evolution times and thus higher precision measurements. In addition to the reduction of the base pressure of the setup, the volume of the beamline gets bigger and an additional pump is connected to the beamline, which all make the dynamic buffer-gas technique, especially the rotating disc approach, more attractive since the helium release time gets shortened. This may enable higher cooling pressures in the Penning trap and therefore faster cooling times to reduce the overall measurement time and enable mass measurements on shorter-lived ions. Since the cryogenic buffer-gas will heat up by collisions with surfaces at room temperature as fast as it cools down, the pumping time in the beamline will not be noticeably affected.

Together with the piezo valve and rotating disc approach, this may conclude in the first dynamic and cryogenic cooled PI-ICR mass spectrometer.

8 Conclusion and Outlook

Within the framework of this master thesis, the novel Penning-trap mass-spectrometer PILOT-Trap based on the *Phase-Imaging Ion-Cyclotron-Resonance* technique was set up at the *Max-Planck-Institute for Nuclear Physics* in Heidelberg.

In the beginning, the 6 T cryogenic coldhead-cooled magnet was successfully commissioned with a temperature readout from the cooling stages. Subsequently, a magnetic field strength measurement on the symmetry axis was carried out. The magnetic field homogeneity of the ISOLTRAP experiment was used to estimate the achievable precision, since comparable excitation radii for the phase-sensitive measurement are used. This comparison predicted a relative mass precision of $\leq 2 \cdot 10^{-7}$, which could be improved by application of shimming coils in future setups. Assuming a shimming effect corresponding to the ISOLTRAP experiment, a precision of $\leq 2 \cdot 10^{-8}$ could be obtained. The latter would fulfill the intended goal written in the introduction. Additionally, the proposed approach to perform cryogenic buffer-gas cooling would improve the relative precision by a factor of 2.4 with a Penning trap at 50 K, whereas a factor of almost 8 can be gained at a temperature of 5 K. The increased resolution of two spots due to the reduction of spot sizes allows the selection of smaller excitation radii. The lower excitation radius of the ions reduces effects caused by magnetic as well as electric inhomogeneity, thus promising an even better improvement. Here, one notices the advantage, besides transportation, of using a coldhead-cooled magnet, as it is rather uncomplicated to connect the trap to a cooling stage compared to a magnet cooled by liquid helium.

The constructed beamline of PILOT-Trap conserves all degrees of freedom for alignment, which was carried out by using a telescope. Installing a perforated drift electrode in front of the delay-line detector and adding an additional pumping path enhanced the pumping cross-section in the ejection path of the ions. With a total length of 3 m and the built-in coldhead-cooled magnet, the PILOT-Trap experiment is suitable for transport. After assembly and alignment of the beamline, the detection of the ions on the MCP detector was possible without ramping the magnet at first. Here, the ions were guided in shooting-through mode by applying the same drift voltage on all electrodes of the beamline. Creating bunched-like ion beams by switching a deflecting electrode near the ion-source realized a first time-of-flight measurement, verifying the detection of rubidium ions. The operation of the ion source exceeded expectations since doubly charged rubidium isotopes could be detected. When ramping up the magnet to 6 T the ion beam still made it through the small pumping barrier of 2 mm radius without any modifications necessary, which indicated a good alignment of the beamline with regard to the magnetic field. Setting up trapping potentials and switching the endcaps of the installed Penning trap

realized the storage of ions, which was verified by trapping the ions with trapping times up to 1 s. With the inlet of helium into the trap, mass-selective buffer-gas cooling was realized by first exciting the magnetron motion of all ions in the trap and then applying the cyclotron coupling to cool the ion of interest. Thus, it was possible to separate the different rubidium isotopes ^{85}Rb and ^{87}Rb with the determined excitation and coupling frequencies. In addition, ionized buffer-gases, here helium, neon and argon were observed due to charge exchange with the doubly charged rubidium isotopes.

To finally realize the PI-ICR technique, the position readout of the delay-line detector was programmed with Python. This readout process was verified with Monte-Carlo simulated coordinate signals. In this process, self-created ion hits were observed, which occur when the times of two ion hits at the detector are within each other's time boundaries. These were prevented by neglecting data of a complete shot when any timing signal is used more than once in the readout to end up in a calculated position. Thus, it was possible to detect the cooling and magnetron excited spots on the delay-line detector. In the beginning, these spots appeared large and were littered with scattered ions. For that reason, the influence of vibration on the spot structure was investigated by triggering the measurement duty cycle on the vibration of the magnet. For this, the vibration of the magnet was recorded with a weighted piezo bender, whose signal was amplified and reshaped to serve as a trigger signal using a constructed Schmitt-trigger circuit. This allowed to place the measurement cycle in the low-vibration period. The comparison to an arbitrary delay and measurements without using the trigger showed a slight improvement in spot structure but no significant reduction of the spot size for cooling and excitation spots.

Reducing the magnification influence of the magnetic field gradient on the ejection path of the ions by lowering the potentials of the drift tubes after the Penning trap lead to reduced spot sizes and enabled the observation of circles made out of magnetron excited spots for different phase accumulation times. This allows phase-sensitive measurements of the magnetron frequency at present, assuming that the magnetron radius blow-up due to the buffer-gas is negligible for the applied phase accumulation times.

Besides the construction of the PILOT-Trap experiment, a piezo valve was constructed and characterized. It enables pressure rises of the buffer-gas of up to the order 10^{-5} mbar, depending on the chosen pressure inside the helium reservoir. The pressure in the reservoir determines the leakage rate, which is on the order of 10^{-7} mbar l/s and low enough to enable measurement pressures on the order of 10^{-8} mbar in the Penning trap of PILOT-Trap. Increasing the voltage which opens the piezo valve even more made it possible to reduce the reservoir pressure to 0.2 mbar by still achieving the typical cooling pressure, such that the leakage rate reduces to the order of 10^{-8} mbar l/s. With these specifications, the piezo valve enables the dynamic buffer-gas cooling with subsequent measurement in the same trap.

To realize measurements of short-lived nuclides, the time during which helium is released had to be examined in more detail. Therefore, the first approach of using a transparent trap consisting of many electrode discs was simulated in MOLFLOW, predicting release times of $\approx$ 600 ms to reduce the pressure from 10^{-5} mbar to 10^{-8} mbar. These predicted release times were experimentally verified with a test setup. To enable measurements of even shorter-lived isotopes, the novel rotating-disc approach was developed. Closing and opening the Penning trap with a rotating disc containing an orifice leads to an instant increase of volume and therefore to an immediate pressure reduction limited by the base pressure. The latter is dependent on the leakage through the distances between the Penning trap and discs. Simulations for different distances of the disc to the Penning trap revealed a reduction in release time by a factor of 3 to $\approx$ 200 ms with a distance of 0.1 mm. To test this approach a test set-up was designed, which will be tested outside the framework of this thesis.

Current status of the PILOT-Trap experiment

During this master thesis, PILOT-Trap has been developed to serve as a completely remotely controllable experiment. Besides safety precautions protecting the setup from power failures and logging the pressures and cooling water temperature, a self-written control system "PILOT-GUI" was programmed to operate all used devices via serial communication. With the latest realization of the dynamic change of the helium inlet into the Penning trap by triggering the fine-dosing valve during a measurement cycle, the modified cyclotron motion can now be excited, without being damped by the buffer-gas. Even though long release times of helium out of the trap will increase the duty cycle length, the realization of converting modified cyclotron in magnetron motion should enable the full realization of the PI-ICR technique. With this, the experimental setup is ready to measure the mass ratio ^{85}Rb / ^{87}Rb as a first physical case. This is well suited for the first commissioning due to comparison to the AME masses.

The achieved precision can be further improved by cryogenic buffer-gas cooling as presented. The developed piezo valve enables the dynamic buffer-gas cooling and subsequent PI-ICR measurement in the same Penning trap. Together with the rotating disc approach, this will allow measurements on short-lived nuclides. In the near future, PILOT-Trap thus could contribute to enable the flight to the island of stability.

9 Bibliography

[1] K. Blaum, "High-accuracy mass spectrometry with stored ions," *Physics Reports*, **425**, no. 1, 1–78, Mar. 1, 2006 (cited on page 1).

[2] D. Lunney, J. M. Pearson, and C. Thibault, "Recent trends in the determination of nuclear masses," *Reviews of Modern Physics*, **75**, no. 3, 1021–1082, Aug. 20, 2003 (cited on page 1).

[3] H. Schatz, A. Aprahamian, J. Görres, *et al.*, "Rp-process nucleosynthesis at extreme temperature and density conditions," *Physics Reports*, **294**, no. 4, 167–263, Feb. 1, 1998 (cited on page 1).

[4] M. G. Mayer, "On Closed Shells in Nuclei," *Physical Review*, **74**, no. 3, 235–239, Aug. 1, 1948 (cited on page 1).

[5] M. Bender, K. Rutz, P.-G. Reinhard, *et al.*, "Shell structure of superheavy nuclei in self-consistent mean-field models," *Physical Review C*, **60**, no. 3, 034304, Aug. 11, 1999 (cited on page 1).

[6] P. Moller and J. R. Nix, "Stability of heavy and superheavy elements," *Journal of Physics G: Nuclear and Particle Physics*, **20**, no. 11, 1681–1747, Nov. 1994 (cited on page 1).

[7] M. Block, D. Ackermann, K. Blaum, *et al.*, "Direct mass measurements above uranium bridge the gap to the island of stability," *Nature*, **463**, no. 7282, 785–788, 7282 Feb. 2010 (cited on page 1).

[8] S. Hofmann and G. Münzenberg, "The discovery of the heaviest elements," *Reviews of Modern Physics*, **72**, no. 3, 733–767, Jul. 1, 2000 (cited on page 1).

[9] K. Morita, K. Morimoto, D. Kaji, *et al.*, "Experiment on the Synthesis of Element 113 in the Reaction ^{209}Bi(^{70}Zn,n)^{278}113," *Journal of the Physical Society of Japan*, **73**, no. 10, 2593–2596, Oct. 15, 2004 (cited on page 1).

[10] Y. Oganessian, "Heaviest nuclei from ^{48}Ca-induced reactions," *Journal of Physics G: Nuclear and Particle Physics*, **34**, no. 4, R165–R242, Mar. 2007 (cited on page 1).

[11] L. S. Brown and G. Gabrielse, "Geonium theory: Physics of a single electron or ion in a Penning trap," *Reviews of Modern Physics*, **58**, no. 1, 233–311, Jan. 1, 1986 (cited on page 1).

[12] J. Karthein, D. Atanasov, K. Blaum, *et al.*, "Direct decay-energy measurement as a route to the neutrino mass," *Hyperfine Interactions*, **240**, no. 1, 61, Jun. 12, 2019 (cited on pages 1, 6, 26).

[13] C. Schweiger, "Direct high-precision measurement of the Q-value of the electron capture in ^{163}Ho for the determination of the neutrino mass", in preparation, 2022 (cited on pages 1, 6).

[14] S. Eliseev, M. Block, M. Dworschak, *et al.*, "A new cryogenic gas-filled stopping chamber for SHIPTRAP," *Nuclear Instruments and Methods in Physics Research Section B: Beam Interactions with Materials and Atoms*, Proceedings of the XVth International Conference on Electromagnetic Isotope Separators and Techniques Related to Their Applications, **266**, no. 19, 4475–4477, Oct. 1, 2008 (cited on page 1).

[15] J. B. Neumayr, L. Beck, D. Habs, *et al.*, "The ion-catcher device for SHIPTRAP," *Nuclear Instruments and Methods in Physics Research Section B: Beam Interactions with Materials and Atoms*, **244**, no. 2, 489–500, Mar. 1, 2006 (cited on page 2).

[16] P. Schury, G. Bollen, M. Block, *et al.*, "Beam purification techniques for low energy rare isotope beams from a gas cell," *Hyperfine Interactions*, **173**, no. 1, 165–170, Nov. 1, 2006 (cited on page 2).

[17] M. Block, D. Ackermann, K. Blaum, *et al.*, "Penning trap mass measurements of transfermium elements with SHIPTRAP," *Hyperfine Interactions*, **196**, 225–231, Feb. 1, 2010 (cited on page 2).

[18] S. Earnshaw, "On the Nature of the Molecular Forces which Regulate the Constitution of the Luminiferous Ether," *Transactions of the Cambridge Philosophical Society*, **7**, 97, Jan. 1, 1848 (cited on page 4).

[19] K. Kromer, "Environmentally-induced systematic effects at the high-precision mass spectrometer PENTATRAP," Ruprecht-Karls-Universität Heidelberg, 2019 (cited on pages 5, 6).

[20] L. S. Brown and G. Gabrielse, "Precision spectroscopy of a charged particle in an imperfect Penning trap," *Physical Review A*, **25**, no. 4, 2423–2425, Apr. 1, 1982 (cited on page 6).

[21] F. Köhler, "Bound-Electron g-Factor Measurements for the Determination of the Electron Mass and Isotope Shifts in Highly Charged Ions," Ruprecht-Karls-Universität Heidelberg, Jul. 22, 2015 (cited on page 8).

[22] M. Mukherjee, D. Beck, K Blaum, *et al.*, "ISOLTRAP: An on-line Penning trap for mass spectrometry on short-lived nuclides," *The European Physical Journal A*, **35**, no. 1, 1–29, Jan. 1, 2008 (cited on page 9).

[23] G. Savard, S. Becker, G. Bollen, *et al.*, "A new cooling technique for heavy ions in a Penning trap," *Physics Letters A*, **158**, no. 5, 247–252, Sep. 2, 1991 (cited on pages 11, 12).

[24] S. Eliseev, K. Blaum, M. Block, *et al.*, "A phase-imaging technique for cyclotron-frequency measurements," *Applied Physics B: Lasers and Optics*, **114**, 396, Sep. 1, 2013 (cited on pages 11, 12, 14–18).

[25] S. Schwarz, "Simulations for Ion Traps Buffer Gas Cooling," *Trapped Charged Particles and Fundamental Interactions*, ser. Lecture Notes in Physics, Berlin, Heidelberg: Springer, 2008, 1–21 (cited on page 12).

[26] H. W. Ellis, R. Y. Pai, E. W. McDaniel, *et al.*, "Transport properties of gaseous ions over a wide energy range," *Atomic Data and Nuclear Data Tables*, **17**, no. 3, 177–210, Mar. 1, 1976 (cited on page 13).

[27] J. Karthein, "Next-Generation Mass Spectrometry of Exotic Isotopes and Isomers," Ph.D. dissertation, Heidelberg, 2020 (cited on pages 14, 17–19).

[28] G. Gräff, H. Kalinowsky, and J. Traut, "A direct determination of the proton electron mass ratio," *Zeitschrift für Physik A Atoms and Nuclei*, **297**, no. 1, 35–39, Mar. 1, 1980 (cited on page 14).

[29] G. Bollen, R. B. Moore, G. Savard, *et al.*, "The accuracy of heavy-ion mass measurements using time of flight-ion cyclotron resonance in a Penning trap," *Journal of Applied Physics*, **68**, no. 9, 4355, Aug. 17, 1998 (cited on page 15).

[30] S. George, S. Baruah, B. Blank, *et al.*, "Ramsey Method of Separated Oscillatory Fields for High-Precision Penning Trap Mass Spectrometry," *Physical Review Letters*, **98**, no. 16, 162501, Apr. 16, 2007 (cited on page 15).

[31] V. Manea, J. Karthein, D. Atanasov, *et al.*, "First Glimpse of the N=82 Shell Closure below Z=50 from Masses of Neutron-Rich Cadmium Isotopes and Isomers," *Physical Review Letters*, **124**, no. 9, 092502, Mar. 5, 2020 (cited on page 18).

[32] "MCP delay line detector manual," version Version 11.0.2201.1, RoentDek Handels GmbH (cited on pages 21, 32, 33).

[33] "Turbomolekularpumpen TURBOVAC MAG W," oerlikon leybold vaccum (cited on page 21).

[34] "TB-118; aluminosilicate ion sources," HeatWave Labs, Inc. (cited on page 23).

[35] "Thermionic effects caused by vapours of alkali metals" (cited on page 23).

[36] "Webpage: RDK-415D2 4K Cryocooler Series," Sumitomo Heavy Industries, Ltd.; Cryogenics Division (cited on page 24).

[37] "Technical instruction; CSW-71D compressor unit," Sumitomo Heavy Industries, Ltd.; Cryogenics Division (cited on page 24).

[38] "Model 27xx integra series, quick start guide," Keithley Instruments, Inc. (cited on page 25).

[39] U. Warring, "Laser Spectroscopy on Os \math{^} : A Prerequisite for the Laser Cooling of Atomic Anions," 2009 (cited on pages 25, 67).

[40] D. Atanasov, "Precision mass measurements for studies of nucleosynthesis via the rapid neutron-capture process," Ruprecht-Karls-Universität Heidelberg, Jul. 6, 2016 (cited on page 26).

[41] J. Ketter, "Theoretical treatment of miscellaneous frequency-shifts in Penning traps with classical perturbation theory", 231, (cited on page 27).

[42] "The DLD delay line detector," version Version 11.0.2201.1, RoentDek Handels GmbH (cited on page 32).

[43] "Model FTA820A octal fast timing amplifier and model FTA420C quad fast timing amplifier, operating manual," ORTEC, 2002 (cited on page 32).

[44] "Model 935, quad constant-fraction 200-mhz discriminator, operating and service manual," ORTEC, 2003 (cited on page 33).

[45] "HPTDC8-PCI time to digital converter with 25ps resolution," version Version 11.0.2201.1, cronologic GmbH & Co. KG (cited on page 33).

[46] J. Karthein, D. Atanasov, K. Blaum, *et al.*, "Analysis methods and code for very high-precision mass measurements of unstable isotopes," *Computer Physics Communications*, **267**, 108070, Oct. 1, 2021 (cited on page 33).

[47] "HV-series multichannel high voltage sources; datasheet and user manual," version Version Rev. 3.51, stahl-electronics.com (cited on pages 34, 85).

[48] "Pulseblaster - programmable pulse and delay generator - owner's manual," SpinCore Technologies, Inc. (cited on page 34).

[49] C. Schweiger, "Fast SiC-MOSFET based high-voltage push-pull switch for charge state separation of highly charged ions with a bradbury-nielsen gate", accepted, 2021 (cited on pages 34, 53).

[50] "Keysight trueform series waveform generator," ORTEC, 2015 (cited on page 34).

[51] "TURBOVAC SL 80," oerlikon leybold vaccum (cited on page 35).

[52] "EVR 116, Gasregelventil, motorisch," PFEIFFER VACUUM (cited on page 35).

[53] "RVC300, Steuergerät, Gasregelventile," PFEIFFER VACUUM (cited on page 35).

[54] R. Kersevan and J.-L. Pons, "Introduction to MOLFLOW+: New graphical processing unit-based Monte Carlo code for simulating molecular flows and for calculating angular coefficients in the compute unified device architecture environment," *Journal of Vacuum Science & Technology A*, **27**, no. 4, 1017–1023, Jul. 2009 (cited on page 50).

[55] D. Neidherr, "Entwicklung einer Pumpsperre für das Penning- Fallen- Massenspektrometer SHIPTRAP," Johannes Gutenberg-Universität Mainz, 2006, 87 pp. (cited on pages 60, 62).

[56] D. Manura and D. Dahl, "SIMION® 8.0 User Manual," *Scientific Instrument Services*, Inc. Ringoes, NJ 08551, 2008 (cited on page 66).

[57] J. Karthein, "Precision mass measurements using the Phase-Imaging Ion-Cyclotron-Resonance detection technique," Ruprecht-Karls-Universität Heidelberg, 2017 (cited on page 66).

[58] J. Ekin, "Experimental Techniques for Low-Temperature Measurements: Cryostat Design, Material Properties and Superconductor Critical-Current Testing." Oxford: Oxford University Press, 2006, 704 pp. (cited on page 67).

[59] M. R. Natisin, J. R. Danielson, and C. M. Surko, "A cryogenically cooled, ultra-high-energy-resolution, trap-based positron beam," *Applied Physics Letters*, **108**, no. 2, 024102, Jan. 11, 2016 (cited on page 68).

10 Acknowledgment

Hier möchte ich mich bei allen bedanken, auch bei jenen die ich im Folgenden nicht genannt habe, die mich bei der Anfertigung dieser Masterarbeit unterstützt haben.

An erster Stelle möchte ich mich bei **Klaus Blaum** für die tolle Betreuung bei dieser Masterarbeit und auch darüber hinaus bedanken. Vielen Dank für die Freiheit am Arbeiten und das entgegengebrachte Vertrauen ein solch spannendes und umfangreiches Projekt umsetzten zu dürfen.

Auch möchte ich mich bei **Yury Litvinov** beanken, für die unkomplizierte Bereitschaft das Zweitgut-achten dieser Arbeit zu übernehmen.

Besonders danken möchte ich **Sergey Eliseev**, der mir stets mit Rat und Tat zur Seite stand. Ich habe unsere Gespräche und Diskussionen über verschiedene Anwendungen und das weitere Vorgehen sehr genossen. Vielen Dank für deine Geduld, die gute Zusammenarbeit, die Unterstützung zur Realisierung eigener Ideen und hilfreichen Kommentare bei der Korrektur dieser Arbeit.

Des weiteren möchte ich mich bei **Christoph Schweiger** bedanken, der mich zur Zeit als HIWI stets unterstützt hat und mir spannende Projekte zuteilte, die mich perfekt auf ein solches Projekt vorbereitet haben.

Auch möchte ich mich bei der gesamten **PENTATRAP-Gruppe**: Pavel, Menno, Kathrin, Nils und Jost für die tolle Arbeitsatmosphäre und eure Unterstützung bedanken. Dabei möchte ich mich speziell bei **Menno Door** für die Diskussionen, Erklärungen und Gedankenexperimente in unseren Pausen bedanken, sowie für deine Unterstützung außerhalb der Arbeit. Besonders möchte ich mich bei meinem Büro-Buddy **Jost Herkenhoff** für ein tolles und spaßiges Jahr bedanken. Ich habe unsere White-Board Sessions mit Musik immer sehr genossen und danke dir für deine Unterstützung in jeglichen Bereichen. Ich bin froh, dass du zum Ende meiner Arbeit doch noch einen Namen für dein Experiment gefunden hast und wünsche dir für dieses viel Erfolg!

Zudem möchte ich auch den Mitgliedern der Gruppen **Alpha-Trap** und **THe** für die gute Zusammenarbeit und tolle Gespräche beim Mittagessen bedanken.

Vielen Dank an **Gabi Weese** für jegliche organisatorische Unterstützung.

Ein großer Dank gilt auch der Werkstatt, Konstruktions- und Elektronik-Abteilung, speziell an Michael Mare, Yannick Steinhauser und Peter Weiß für die tolle Zusammenarbeit und schnelle Umsetzung verschiedener Projekte.

Außerdem möchte ich mich bei meinen Studienfreunden bedanken, für die Unterstützung und tolle Zeit während des Studiums. Zuletzt möchte ich mich bei meiner Familie bedanken, die mich während meines gesamten Studiums stets bedingungslos unterstützt hat.

Erklärung:

Ich versichere, dass ich diese Arbeit selbstständig verfasst habe und keine anderen als die angegebenen Quellen und Hilfsmittel benutzt habe.

Heidelberg, den 05.08.2022 .....

Part I

Appendix

A More Details on used Devices

A.0.1 Delay-Line Detector

Dark Current Measurement

For the calibration of the detector, a dark current measurement was carried out. With this, the levels of the CFD were adjusted,resulting in five noise counts per second for the MCP signal. In addition, the levels of the coordinate timing signals were optimized to achieve a uniform frequency. Furthermore the coordinate signals are optimized so that every MCP signal is followed by the four coordinate timing signals to lead to a clear allocation of positions. With this, the timing distribution of the coordinate timing signals with respect to the MCP timing signal were measured to determine the boundary conditions used by the readout analysis. These measured distributions are displayed in figure A.1.

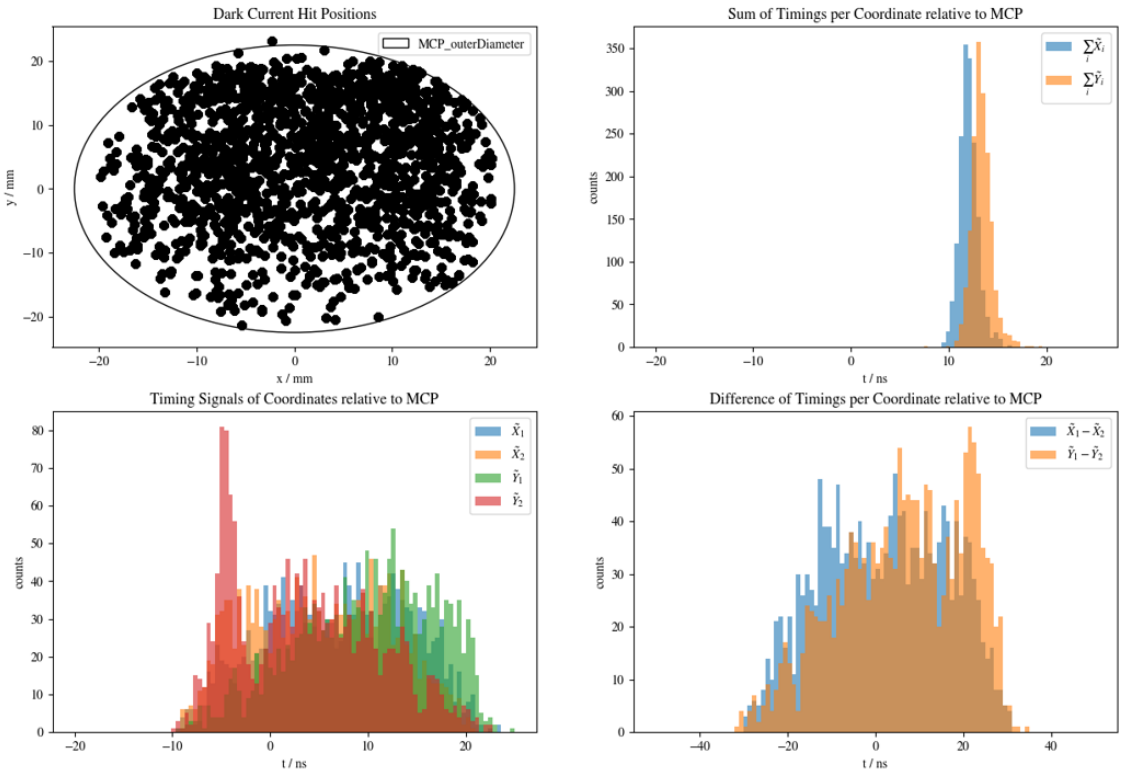

Figure A.1: *Dark Current Measurement to record Coordinate Times Distribution*

Monte-Carlo-Simulation to verify the Readout Process

To cross-check the readout process of different time marks ($\{X_1, X_2, Y_1, Y_2, MCP\}$) towards the determined ion hit positions a Monte-Carlo-Simulation was carried out. Thereby random positions of hits on the detector are generated and calculated to timing differences $\Delta\tilde{T} = \tilde{T}_1 - \tilde{T}_2$ for each coordinate $T \in \{X, Y\}$ with the single pitch velocity of the delay lines. A random timing sum $\sum_{i=1}^{2} \tilde{T}_i$ is generated from the in figure A.1 b) displayed distribution, for each coordinate respectively. With this, the random generated coordinate timings are calculated with

$$\tilde{T_1}, \tilde{T_2} = \frac{\sum_i \tilde{T_i} \pm \Delta\tilde{T}}{2} \quad . \tag{A.1}$$

Last but not least, a random MCP timing signal is generated out of a set ToF-distribution. Thus, the original measured coordinate timings $T_i = \tilde{T_i} + MCP$ in nanoseconds are calculated. With respect to the digitization bin size of 25 ps of the measured timing signals, the calculated timings are multiplied by the factor $25 \cdot 10^{-3}$. The simulated distribution was verified to be the same as shown in figure A.1.
Analyzing these simulated timing signals with the measurement readout scripts results in the projections displayed in figure A.2. In this figure, the positions of the simulated and detected hits are scattered above each other in different order. On the left, the detected positions are plotted on top of the simulated positions and vice versa for the projections on the right. For one simulated ion per shot, a perfect agreement in position and number of detected hits is observed. Below, the projections with two simulated ions per shot are displayed. As expected, timing signals of two ions may be located in each other's boundary conditions, so that self-created hits from the readout analysis are possible. These can be seen on the lower right, where the additionally created hits are displayed in blue.
By neglecting the data of a complete shot, when any timing signal is used twice for a position creation, this effect could be avoided. On the other hand, this leads to fewer detected ions, since the data of a complete shot is discarded. The origin of this effect can be further investigated by measuring it's scaling with the ToF width. Since no such self-created hits was desired, the sorting-out condition of double-used signals will be used and the ions per shot will be optimized to one in the experiment. Currently, the discard of shots is no problem since an offline ion-source is used, but may has to be investigated in more detail when using an online source.

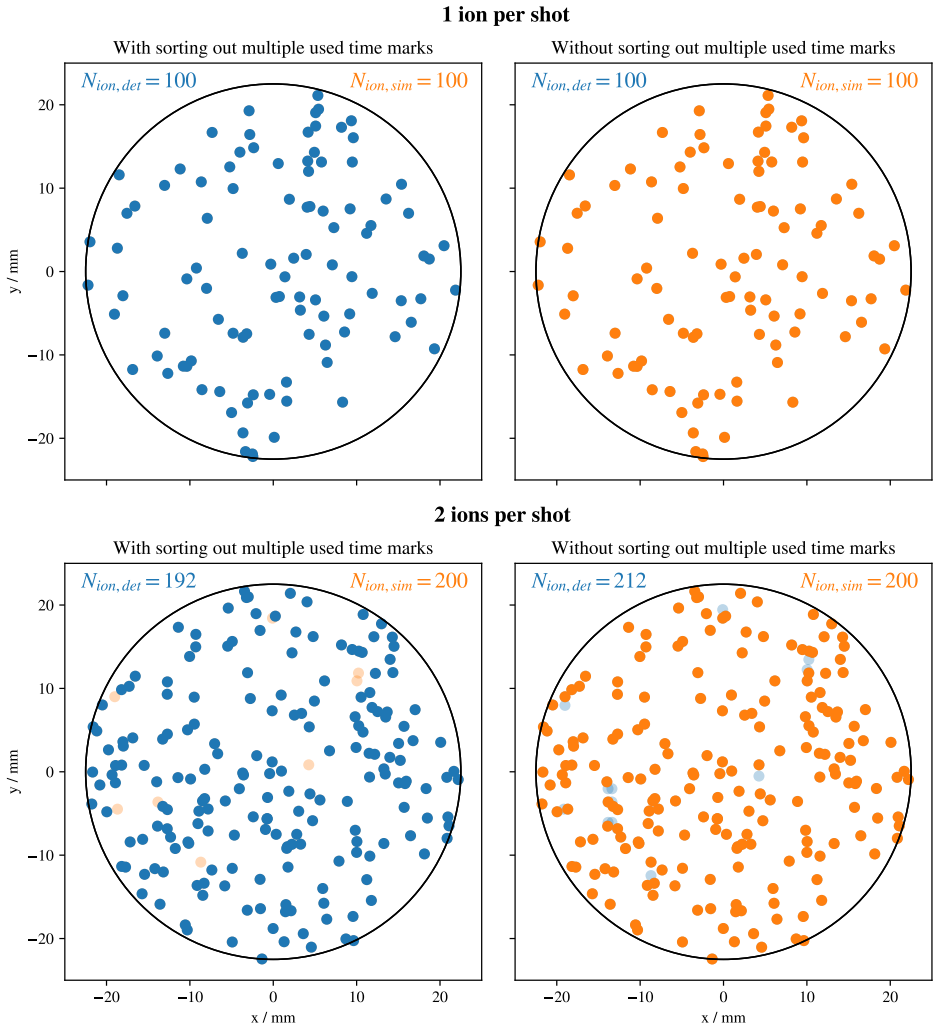

Figure A.2: *Readout verification with Monte-Carlo simulation of ion positions* The simulation projections of one and two ions per shot are displayed. Thereby the simulated (orange) and detected (from readout analysis, blue) positions are scattered above each other. On the left, the detected ones are plotted on top and on the right vice versa. In contrast to one ion per shot, more ions per shot are leading to self-created hits when one time signal fits in the timing boundary conditions of another ion, which can be seen on the right. This effect is avoided by neglecting the complete data of one shot, when a timing signal is used twice for position creation, which is displayed on the left.

Parameter	Typical	Maximal
Scaling error of setting	0.015 %	0.05 %
Offset error	±10 mV	±100 mV
Ripple (50/60 Hz)	2.5 mVpp	5 mVpp
Noise (> 10 Hz)	2 mVrms	-
Low frequency noise (0.1 − 1 Hz)	1.3 mVrms	-
Channel cross-talk	1.2 ppm	2.5 ppm
Temperature coefficient scaling	±10 ppm/K	±18 ppm/K
Temperature coefficient offset	1.5 mV/K	4.5 mV/K

Table A.1: *Noise of high-voltage source HV500-16*

A.0.2 Voltage source

The *HV500-16* from the manufacturer *stahl-electronics.com* [47] is a high-precision, low-noise DC voltage source and offers 16 bipolar, sharing ground channels with a voltage range of ±500 V, delivering a current up to 70 μA over a 2.7 kΩ DC output resistance. It is controlled via an USB2-connector, introducing a scaling error of a voltage setting of 0.015% of full span, resulting in a possible 150 mV systematic offset. In addition, the other errors and noises are in the order of mV and are summarized in table A.0.2, where the manufacturing measurements can be looked up in [47]. Furthermore, a voltage stability measurement has been carried out for all channels, which results are listed in table A.0.2. Summing up, the typical deviation is 1 mV by a set voltage of 100 V . But some channels have a deviation from 30 mV, so that the channel allocation has to be chosen with care (see also in table A.0.2).

Channel	Standard Deviation from 100 V	Connection to
CH 1	1.12 mV	EC1 high
CH 2	1.04 mV	EC2 high
CH 3	1.14 mV	CE1 high
CH 4	0.96 mV	CE2 high
CH 5	38.7 mV	En
CH 6	1.04 mV	DT3 high
CH 7	31.6 mV	D0-2
CH 8	1.09, mV	CE2 low
CH 9	1.17 mV	EC2 low
CH 10	1.13 mV	D0-3,4
CH 11	1.13 mV	DT1
CH 12	1.16 mV	DT2
CH 13	-	Defect
CH 14	1.10 mV	DT3 low
CH 15	1.16 mV	D0-1 (Defl.)
CH 16	1.13 mV	DT4

Table A.2: *Measured voltage stability of the high-voltage source HV500-16*

B Transparent Trap

As described in chapter 6, the time for the release of helium is dependent on the pumping speed. To realize a fast release, a high pumping cross-section should be chosen. This can be achieved by a transparent Penning trap consisting of many thin electrode discs. The construction of a transparent Penning trap is shown in figure B.1.

Figure B.1: *Construction of the transparent Penning trap*
A cylindrical Penning trap consisting of many thin electrode discs is displayed, which offers much transparency and therefore a high pumping cross-section.

To see whether this approach is suitable for PILOT-Trap, the time of the pressure reduction by pumping was simulated for the PILOT-Trap beamline, which results are shown in figure B.1. For comparison, a pumping test setup was used to determine the pumping time constant experimentally. In addition, the pumping time constant is simulated for this test setup as well. This verification is described in the section B.2.

B.1 Molflow Simulation of Helium Pumping Time

To study the transparent-trap approach, the pumping time which is needed to reduce the helium pressure from 10^{-5} mbar to 10^{-9} mbar was simulated. For this, a completely transparent trap was assumed. For this only the piezo-valve was simulated by an orifice in the beamline with an outgasing mass flow of $\approx 10^{-3}$ mbar l/s. In the simulation of the presented best-case scenario, the drift tubes were also assumed to be transparent and no outgasing of the walls was considered. The rest was considered like it is in the PILOT-Trap experiment. The piezo valve was opened for 100 ms to reach a pressure of 10^{-5} mbar in the trap region. Then, the valve is completely closed, without leakage. The pressure evolutions are shown in figure B.2. As can be seen, after the helium inlet stops all the pressure lines converge. The reason for divergence after 600 ms is the low statics that could be collected. This is due to the reduction of the probability of a particle flying through the small areas at lower pressures, so the red line of the mean beamline pressure gives the best estimation. At the mean pressure development of the beamline, the exponential decay function

$$p(t) = p_0 \exp(-\frac{t}{\tau}) \tag{B.1}$$

was fitted after the helium inlet stopped, where p_0 indicates the initial helium pressure, t the time and τ the pumping time constant. There is no pressure offset constant included in eq. (B.1) since the simulation has not included any other outgasing source, which could lead to a pressure equalization point. The fit yields to $\tau = 104 \pm 3 \cdot 10^{-3}$ s.

Based on this simulation, the transparent trap design seems not to be suitable for the PILOT-Trap experiment since the pumping time of $\approx$ 600 ms to reduce the helium pressure from 10^{-5} mbar to 10^{-8} mbar is too long compared to the vibration cycle of the coldhead magnet with frequency of 2 Hz.

The reason for the long pumping time is the high base pressure of the beamline, which raises during the helium injection, since the trap is designed to be transparent. This observation gave rise to the idea of a closed Penning trap, which would not raise the base pressure during cooling. When opening the trap, the pressure reduces immediately due to the increase in volume. This idea is pursued in chapter 6.

To ensure that this simulated pumping time constant is correct, a helium pumping test station was constructed, to measure the pumping time constant experimentally and compare it to a simulation of this test station. This is described in the following section.

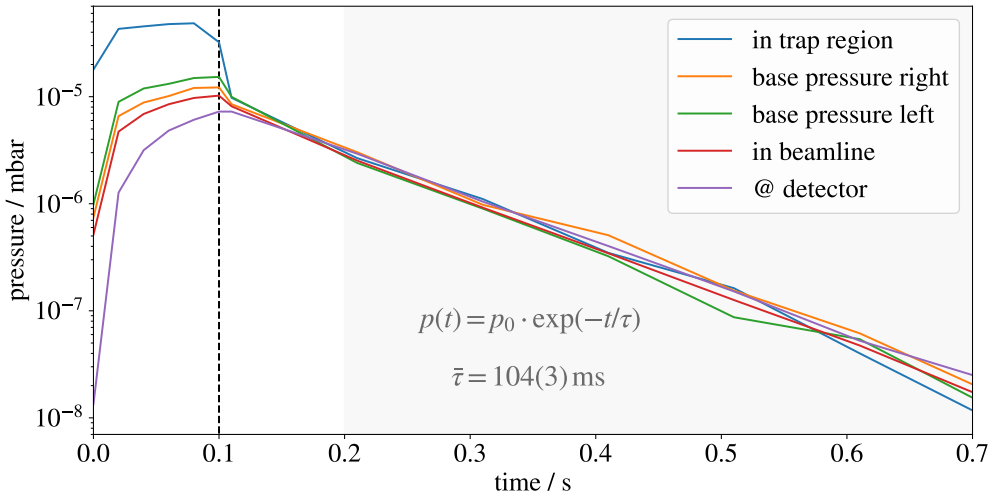

Figure B.2: *Best case simulated pressure evolution in PILOT-Trap beamline with transparent trap*
The dashed line indicates the time the valve closes. As a result, the simulation predicts a pumping time of about 600 ms to reduce the pressure from 10^{-5} mbar to 10^{-8} mbar. The exponential decay fit on the pressure evolutions in the gray shaded time boundary yields to pumping time constants, which average is determined to $\bar{\tau} = (104 \pm 3)$ ms.

B.2 Verification of the pumping time constant

For verification of the simulated pumping time constant (and general check-up of the MOLFLOW simulations) the pumping time constant has to be determined experimentally. Since at this time the beamline of the PILOT-Trap experiment was not set up, a separate setup was used. Therefore, an old beamline construction was reassembled to a pumping test setup. This setup uses only one turbo pump with pumping speed $S = 600\,\mathrm{l/s}$. The enclosed volume $V_{test} = 47\,\mathrm{l}$ of this test beamline corresponds to roughly half of the volume present in the PILOT-Trap beamline. Therewith, the effect of using a smaller volume and only one pump should cancel each other, so that it is a good representation of the PILOT-Trap experiment.
The construction of the test setup is displayed in figure B.3. Full-range pressure gauges *PKR251* are installed at the left and right vacuum crosses. The helium inlet valve is located on the left cross, whereas the pump is installed at the down running tube on the right. Thus, one pressure sensor represents the helium inlet, whereas the other measures the pressure near the pump. The helium flow was controlled by the inlet valve *EVR116*. Between this valve and the beamline, a hand-driven valve is installed. The time of closing the valve manually is smaller than the estimated pumping time of the helium (see section B.1).
The analog voltage signal of the pressure gauges is recorded with an oscilloscope

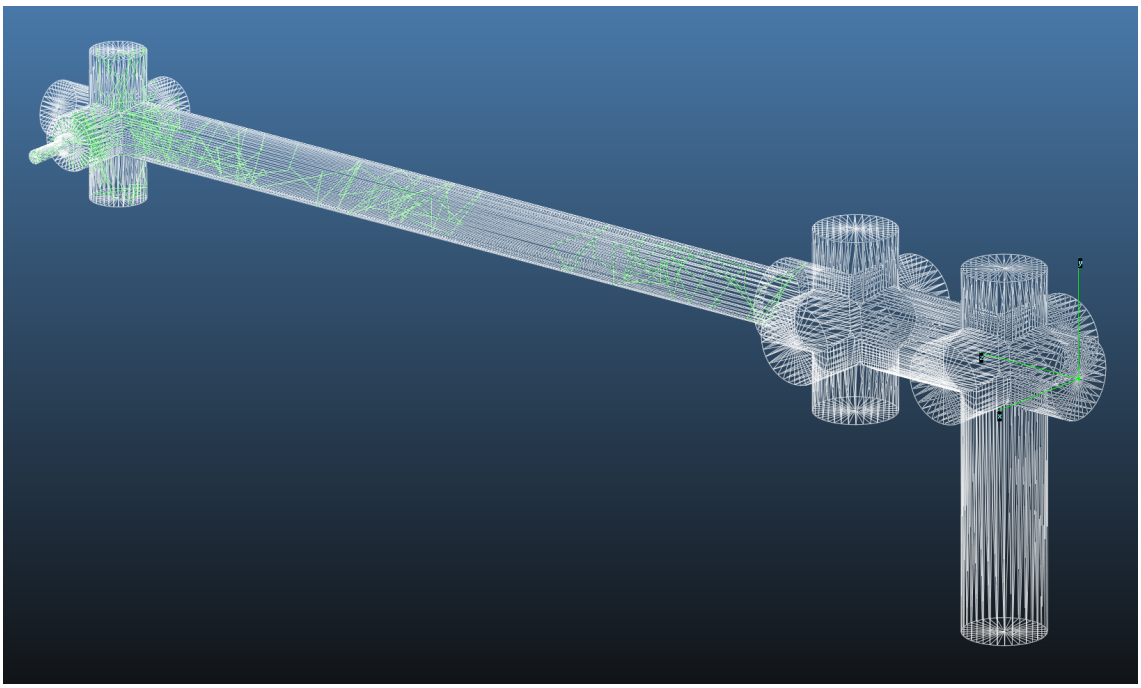

Figure B.3: *Design of the test setup in MOLFLOW*
On the left, the thin tube leads to a manual valve, whose end is the outgasing area for the simulated helium flow with $5 \cdot 10^{-5}$ mbar l/s. The tube running down on the lower right leads to the turbo pump so that the lower area defines the pumping area with pumping speed $S = 600\,\mathrm{l/s}$. The green lines represent the trajectory of helium atoms colliding with a wall in the simulated time step.

which could be calculated back to the pressures. Thereby, the analog measuring rate of $\geq 100\,/\,\mathrm{s}$ is fast enough to measure the expected pressure evolution. As an example, the pressure evolution near the pump is shown in figure B.4.
The evolution of pressure in the gray shaded area is fitted by an exponential decay

$$p(t) = p_0 \exp(-\frac{t}{\tau}) + p_e, \tag{B.2}$$

which distinguishes from eq. (B.1) with the equilibrium pressure offset p_e added.
Finally, the experimental pumping time constant was derived to be $\tau_{pump,exp} = (0.1668 \pm 0.0026)\,\mathrm{s}$ at the pump side and $\tau_{in,exp} = (0.151 \pm 0.003)\,\mathrm{s}$ at the helium inlet side.
This experimental setup was simulated with MOLFLOW by detecting the pressures at the same places as in the experiment. The helium inlet was simulated with an area as big as the tube of the fine dosing valve. The simulated pressure evolution is shown in figure B.5, where the graph labeled as "beamline" represents the mean pressure over the whole beamline.
Analog to section B.1, the evolutions of pressure are fitted by eq. (B.1), which yields to $\tau_{pump,sim} = 0.123\,\mathrm{s}$ and $\tau_{in,sim} = 0.118\,\mathrm{s}$. With this, the simulation leads

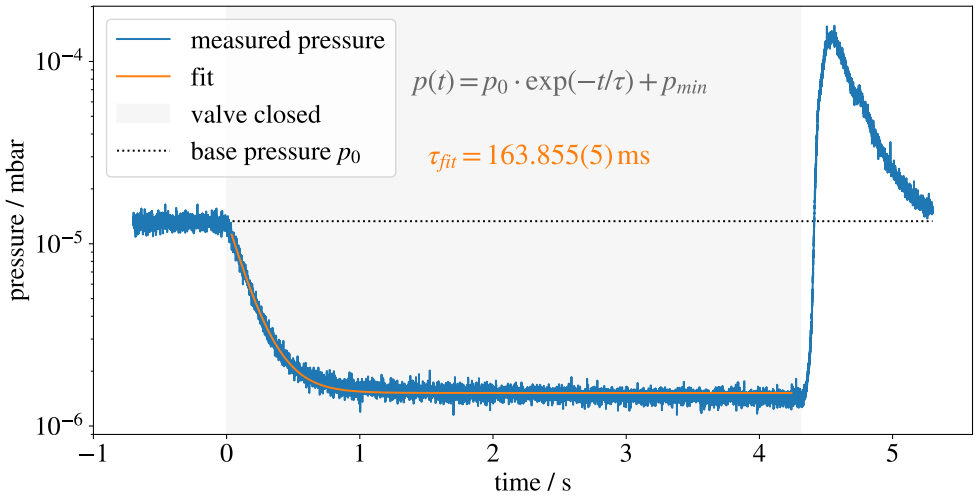

Figure B.4: *Pressure evolution in pumping time test setup on pump side*
At the beginning the pressure is in equilibrium with the helium flow. Then the valve is closed and the pressure decays exponentially towards the equilibrium pressure p_e. After a certain time, the valve is opened again. The valve is closed for the gray shaded time area, which is used to perform an exponential decay fit on the evolution of the pressure.

to an agreement within 26 % and 22 %, respectively. In conclusion, the simulated pumping time constant τ for the PILOT-Trap is correct. Thus, the real pumping time constant for the PILOT-Trap experiment is assumed to be $\tau_{PILOT} \geq 0.1\,\mathrm{s}$. This implies that an assembly as the transparent trap will not be suitable to measure masses on short-lived nuclides with half-lives below a fraction of a second.

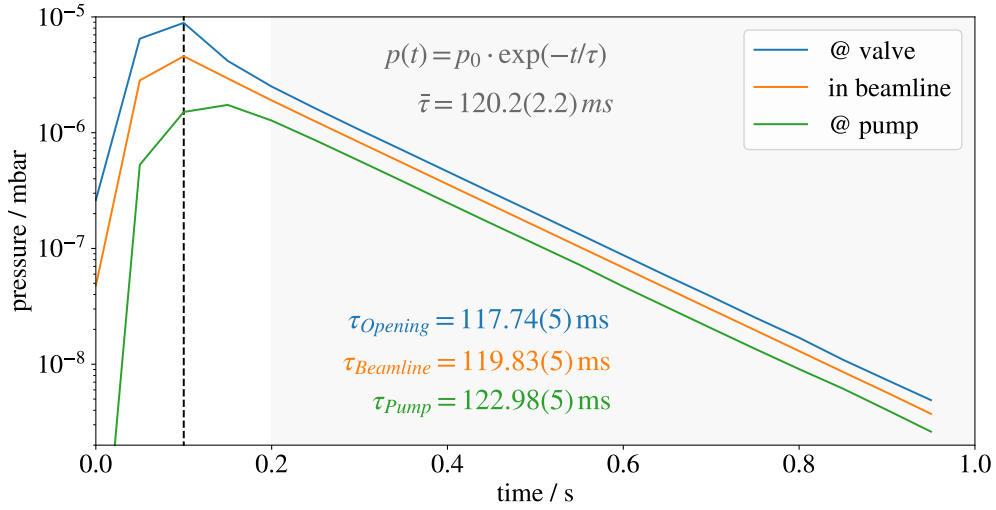

Figure B.5: *Simulated pressure evolutions in the test setup*
The simulated pressure evolutions for the different pressure gauges are shown, as well as the mean pressure in the beamline (orange). The dashed line indicates the time when the valve closes. A pumping time of ≈ 900 ms is required to reduce the helium pressure from 10^{-5} mbar to 10^{-9} mbar.

C Frequency Scan

When performing the mass-selective buffer-gas cooling, the frequency of the magnetron motion and the coupling were first determined manually (see chapter 5.3). During the spot optimization described in chapter 5.4, the tuning ratio was adjusted. Nevertheless, large spot sizes are observed. To ensure that the right frequencies for excitation and coupling are applied a frequency scan was again performed, which is presented in the following.
First, the excitation of the magnetron motion was optimized. For this purpose, the amplitude was first determined with the previously determined frequency at which no more ions are detected at the MCP since the ions are excited to such large radii that they collide with the pump barrier. Then, a frequency scan was performed at this particular amplitude. These two processes were then individually performed again with the newly determined amplitude and frequency. The last optimization is shown in the figure C.1. The plots a) and b) show the scans for the detected rubidium ions, while c) and d) additionally show the behavior of the noble gases. It can be seen, that the number of detected argon ions increases while the number of detected rubidium ions decreases. This could be due to the increased ionization cross-section resulting from larger radii, while the orbital frequency of the doubly charged rubidium ions remains the same. Based on this scan, the optimal magnetron excitation was determined with an amplitude of 0.3 V and a frequency of $\omega_- = 880\,\mathrm{Hz}$.
Next, the coupling with the free cyclotron frequency was optimized, which, starts simultaneously with the magnetron excitation. The amplitude was scanned at the cyclotron frequency already determined. With larger amplitudes, more ions per shot are detected until a plateau occurs. The amplitude at which it changes to a plateau was used for the subsequent frequency scan. The second amplitude scan is displayed in figure C.2 with and without the noble gas behavior. In b), the decrease in number of detected argon ions is shown at higher coupling amplitudes, while the number for the selected rubidium isotope increases. In contrast, the last performed frequency scan considered the spot size for different coupling frequencies. This was determined for each coordinate dimension using a Gaussian fit analog as displayed in figure 5.7. The spot sizes in dependence of the coupling frequency are displayed in figure C.3 a). Based on this measurements, no deviation towards the already determined coupling frequencies could be detected. In figure C.3 b), it is shown that almost all MCP signals originate from detected rubidium. In addition, the percentage of fully detected coordinate signals compared to detected MCP signals for rubidium can be used to estimate the efficiency of the delay line detector to be $\approx 67\,\%$.

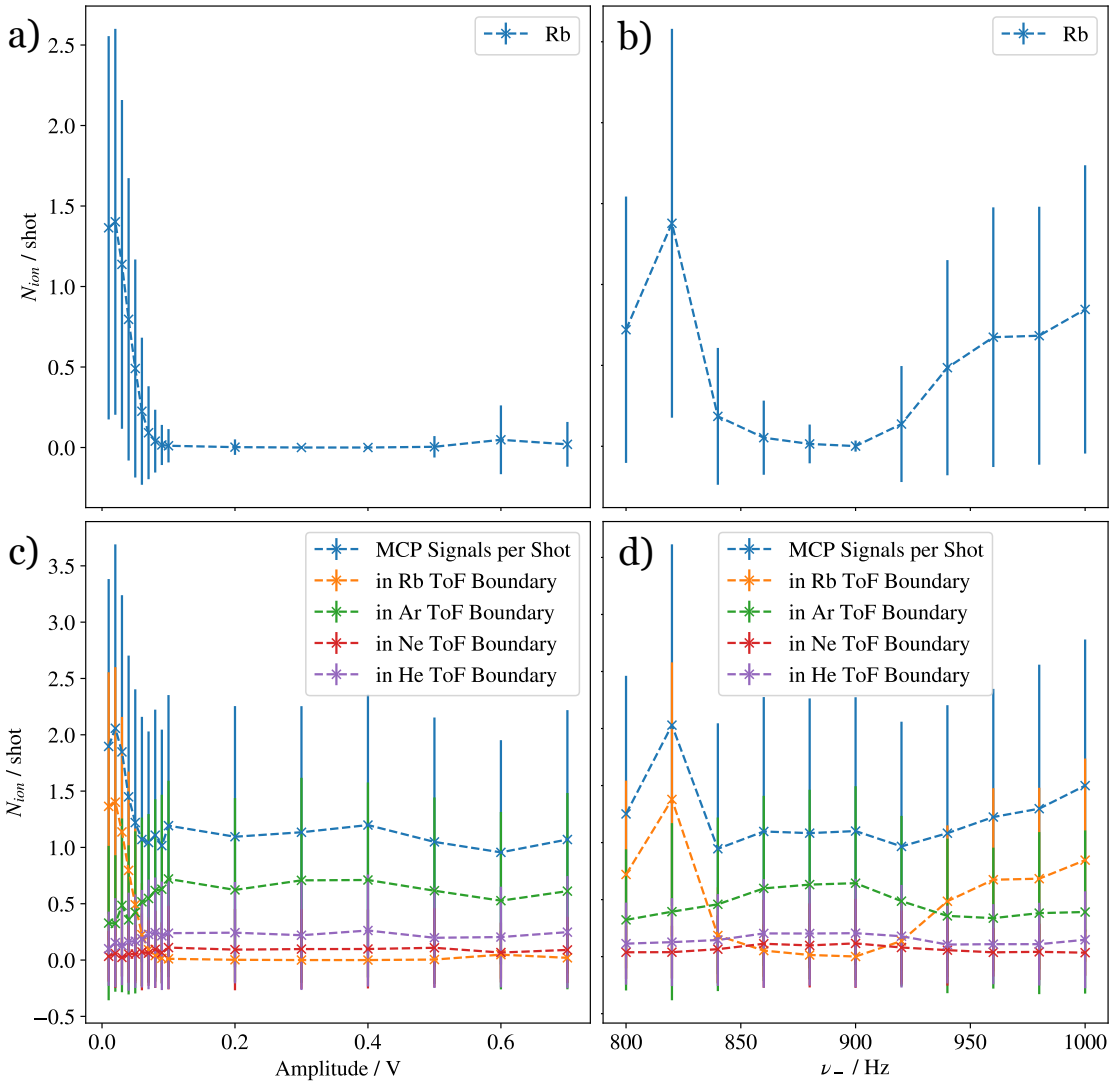

Figure C.1: *Magnetron amplitude and frequency scan*
a) and c) displays the amplitude scan, where c) additionally shows the behavior of the noble gases during the scan.
b) and d) displays the frequency scan, where the minimum for the number of detected rubidium ions indicates the optimal excitation frequency. Additionally, d) displays the number of detected noble gas ions during the scan.

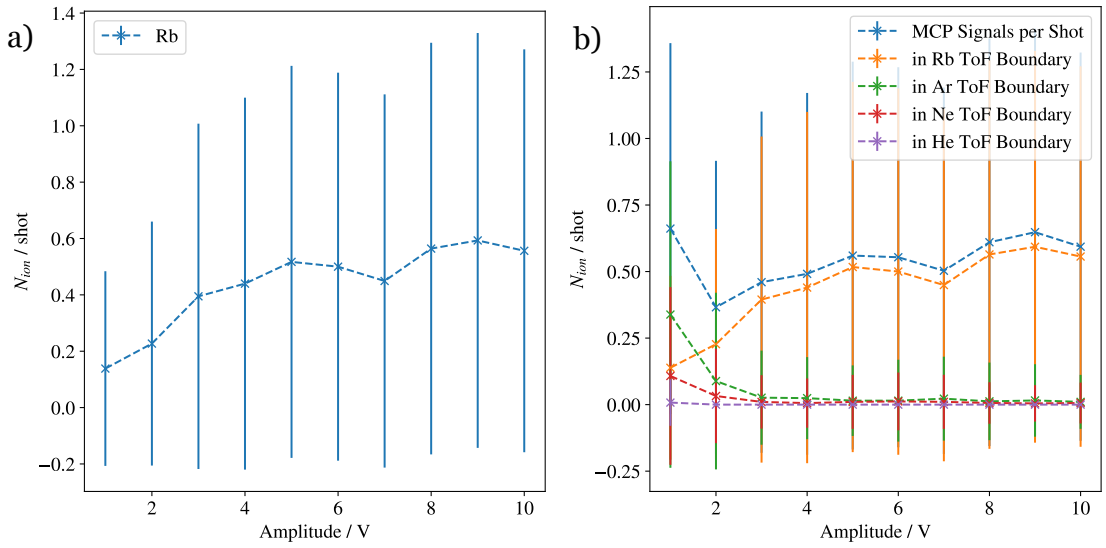

Figure C.2: *Free cyclotron amplitude scan*
a) displays the number of detected rubidium ions during the amplitude scan, whereas in b) additional the number of detected noble gas ions is presented.

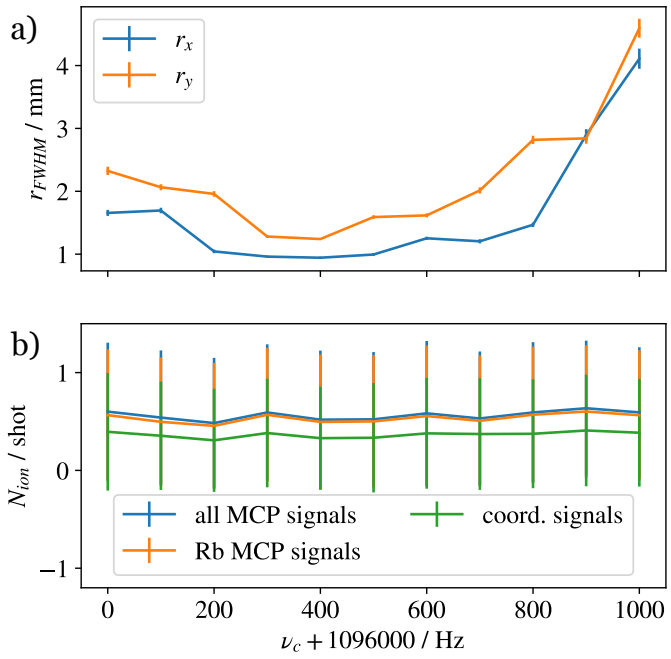

Figure C.3: *Free cyclotron frequency scan*
a) displays the radii of the detected rubidium spots during the frequency scan.
b) presents the average number of all detected MCP signals (blue) per shot together with the proportion of signals in the ToF-boundary of rubidium (orange) and the number of complete coordinate signals for rubidium (green).